



Universiteit Gent
Faculteit Wetenschappen
Vakgroep Fysica en Sterrenkunde

² No title yet

³ No sub-title neither, obviously...

⁴ Alexis Fagot

5



Thesis to obtain the degree of
Doctor of Philosophy in Physics
Academic years 2012-2017



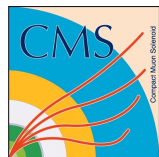


Universiteit Gent
Faculteit Wetenschappen
Vakgroep Fysica en Sterrenkunde

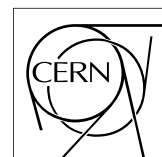
Promotoren: Dr. Michael Tytgat
Prof. Dr. Dirk Ryckbosch

Universiteit Gent
Faculteit Wetenschappen
Vakgroep Fysica en Sterrenkunde
Proeftuinstraat 86, B-9000 Gent, België
Tel.: +32 9 264.65.28
Fax.: +32 9 264.66.97

17



Thesis to obtain the degree of
Doctor of Philosophy in Physics
Academic years 2012-2017



Acknowledgements

¹⁹ Ici on remerciera tous les gens que j'ai pu croiser durant cette aventure et qui m'ont permis de passer
²⁰ un bon moment

²¹ *Gent, ici la super date de la mort qui tue de la fin d'écriture*
²² *Alexis Fagot*

Table of Contents

24	Acknowledgements	i
25	Nederlandse samenvatting	vii
26	English summary	ix
27	1 Introduction	1-1
28	1.1 A story of High Energy Physics	1-1
29	1.2 Organisation of this study	1-1
30	2 Investigating the TeV scale	2-1
31	2.1 The Standard Model of Particle Physics	2-2
32	2.1.1 A history of particle physics	2-2
33	2.1.2 Construction and test of the model [TO SEE IF KEPT - MAYBE TOO COMPLEX]	2-11
34	2.1.3 Investigating the TeV scale	2-11
35	2.2 The Large Hadron Collider & the Compact Muon Solenoid	2-11
36	2.2.1 LHC, the most powerful particle accelerator	2-11
37	2.2.1.1 Particle acceleration	2-13
38	2.2.1.2 LHC discoveries and LHC physics program	2-15
39	2.2.1.3 High Luminosity LHC	2-16
40	2.2.2 CMS, a multipurpose experiment	2-16
41	2.3 Muon Phase-II Upgrade	2-16
42		
43	3 Physics of Resistive plate chambers	3-1
44	3.1 Principle	3-1
45	3.1.1 Electron drift velocity	3-4
46	3.2 Rate capability and time resolution of Resistive Plate Chambers	3-4
47	3.2.1 Operation modes	3-4
48	3.2.2 Detector designs and performance	3-6
49	3.2.2.1 Double-gap RPC	3-7
50	3.2.2.2 Multigap RPC (MRPC)	3-8
51	3.2.2.3 Charge distribution and performance limitations	3-9
52	3.3 Signal formation	3-12
53	3.4 Gas transport parameters	3-12
54	4 Longevity studies and Consolidation of the present CMS RPC subsystem	4-1
55	4.1 Resistive Plate Chambers at CMS	4-1
56	4.1.1 Overview	4-1
57	4.1.2 The present RPC system	4-2
58	4.1.3 Pulse processing of CMS RPCs	4-3

59	4.2	Testing detectors under extreme conditions	4-4
60	4.2.1	The Gamma Irradiation Facilities	4-7
61	4.2.1.1	GIF	4-7
62	4.2.1.2	GIF++	4-9
63	4.3	Preliminary tests at GIF	4-11
64	4.3.1	Resistive Plate Chamber test setup	4-11
65	4.3.2	Data Acquisition	4-13
66	4.3.3	Geometrical acceptance of the setup layout to cosmic muons	4-13
67	4.3.3.1	Description of the simulation layout	4-14
68	4.3.3.2	Simulation procedure	4-16
69	4.3.3.3	Results	4-17
70	4.3.4	Photon flux at GIF	4-17
71	4.3.4.1	Expectations from simulations	4-17
72	4.3.4.2	Dose measurements	4-22
73	4.3.5	Results and discussions	4-23
74	4.4	Longevity tests at GIF++	4-24
75	4.4.1	Description of the Data Acquisition	4-27
76	4.4.2	RPC current, environmental and operation parameter monitoring	4-28
77	4.4.3	Measurement procedure	4-29
78	4.4.4	Longevity studies results	4-29
79	5	Investigation on high rate RPCs	5-1
80	5.1	Rate limitations and ageing of RPCs	5-1
81	5.1.1	Low resistivity electrodes	5-1
82	5.1.2	Low noise front-end electronics	5-1
83	5.2	Construction of prototypes	5-1
84	5.3	Results and discussions	5-1
85	6	Conclusions and outlooks	6-1
86	6.1	Conclusions	6-1
87	6.2	Outlooks	6-1
88	A	A data acquisition software for CAEN VME TDCs	A-1
89	A.1	GIF++ DAQ file tree	A-1
90	A.2	Usage of the DAQ	A-2
91	A.3	Description of the readout setup	A-3
92	A.4	Data read-out	A-3
93	A.4.1	V1190A TDCs	A-4
94	A.4.2	DataReader	A-6
95	A.4.3	Data quality flag	A-10
96	A.5	Communications	A-12
97	A.5.1	V1718 USB Bridge	A-13
98	A.5.2	Configuration file	A-13
99	A.5.3	WebDCS/DAQ intercommunication	A-17
100	A.5.4	Example of inter-process communication cycle	A-18
101	A.6	Software export	A-18

102	B Details on the offline analysis package	B-1
103	B.1 GIF++ Offline Analysis file tree	B-1
104	B.2 Usage of the Offline Analysis	B-2
105	B.2.1 Output of the offline tool	B-3
106	B.2.1.1 ROOT file	B-3
107	B.2.1.2 CSV files	B-5
108	B.3 Analysis inputs and information handling	B-6
109	B.3.1 Dimensions file and IniFile parser	B-6
110	B.3.2 TDC to RPC link file and Mapping	B-7
111	B.4 Description of GIF++ setup within the Offline Analysis tool	B-9
112	B.4.1 RPC objects	B-9
113	B.4.2 Trolley objects	B-10
114	B.4.3 Infrastructure object	B-11
115	B.5 Handeling of data	B-12
116	B.5.1 RPC hits	B-13
117	B.5.2 Clusters of hits	B-14
118	B.6 DAQ data Analysis	B-15
119	B.6.1 Determination of the run type	B-16
120	B.6.2 Beam time window calculation for efficiency runs	B-17
121	B.6.3 Data loop and histogram filling	B-18
122	B.6.4 Results calculation	B-19
123	B.6.4.1 Rate normalisation	B-19
124	B.6.4.2 Rate and activity	B-21
125	B.6.4.3 Strip masking tool	B-23
126	B.6.4.4 Output CSV files filling	B-25
127	B.7 Current data Analysis	B-29

¹²⁸

Nederlandse samenvatting –Summary in Dutch–

¹²⁹

¹³⁰ Le resume en Neerlandais (j'aurais peut-être pu apprendre la langue juste pour ça...).

¹³¹

English summary

¹³² Le meme résume mais en Anglais (on commencera par la hein!).

List of Figures

133

134 2.1	Through the gold foil experiment Rutherford could show that most of the mass of 135 atoms was contained in a positively charged nucleus and could then propose a more 136 accurate atomic model than that of Thomson.	2-3
137 2.2	Figure 2.2a: Meson octet. Figure 2.2b: Baryon octet. Figure 2.2c: Baryon decuplet. .	2-8
138 2.3	CERN accelerator complex.	2-12
139 2.4	Pictures of the different accelerators. From top to bottom: first the LINAC 2 and the 140 <i>Pb</i> source of LINAC 3. Then the Booster and the LEIR. Finally, the PS, the SPS and 141 the LHC.	2-14
142 2.5	Figure 2.5a: schematics of the LHC cryodipoles. 1: Superconducting Coils, 2: Beam 143 pipe, 3: Heat exchanger Pipe, 4: Helium-II Vessel, 5: Superconducting Bus-bar, 6: 144 Iron Yoke, 7: Non-Magnetic Collars, 8: Vacuum Vessel, 9: Radiation Screen, 10: 145 Thermal Shield, 11: Auxiliary Bus-bar Tube, 12: Instrumentation Feed Throughs, 146 13: Protection Diode, 14: Quadrupole Bus-bars, 15: Spool Piece Bus-bars. Fig- 147 ure 2.5b: magnetic field and resulting motion force applied on the beam particles. .	2-15
148 2.6	Figure 2.6a: picture of the LHC quadrupoles. Figure 2.6b: magnetic fields and 149 resulting focussing force applied on the beam by 2 consecutive quadrupoles.	2-15
150 2.7	Absorbed dose in the CMS cavern after an integrated luminosity of 3000 fb. R is the 151 transverse distance from the beamline and Z is the distance along the beamline from 152 the Interaction Point at Z=0.	2-16
153 2.8	A quadrant of the muon system, showing DTs (yellow), RPCs (light blue), and CSCs 154 (green). The locations of new forward muon detectors for Phase-II are contained 155 within the dashed box and indicated in red for GEM stations (ME0, GE1/1, and 156 GE2/1) and dark blue for improved RPC (iRPC) stations (RE3/1 and RE4/1).	2-17
157 2.9	RMS of the multiple scattering displacement as a function of muon p_T for the pro- 158 posed forward muon stations. All of the electromagnetic processes such as bremsstrahlung 159 and magnetic field effect are included in the simulation.	2-18
160 3.1	Different phases of the avalanche development in the RPC gas volume subjected to 161 a constant electric field E_0 . a) An avalanche is initiated by the primary ionisation 162 caused by the passage of a charged particle through the gas volume. b) Due to 163 its growing size, the avalanche starts to locally influence the electric field. c) The 164 electrons, lighter than the cations reach the anode first. d) The ions reach the cathode. 165 While the charges have not recombined, the electric field in the small region around 166 the avalanche stays affected and locally blind the detector.	3-2
167 3.2	Effeciency (circles and stars with 30 mV and 100 mV thresholds respectively) and 168 streamer probability (opened circles) as function of the operating voltatge of a 2 mm 169 single gap HPL RPC flushed with a gas mixture containing (a) 5%, (b) 2%, (c) 1% 170 and (d) no SF_6 [33].	3-3

171	3.3	Movement of the charge carriers in an RPC. Figure 3.3a: Voltage across an RPC whose electrode have a relative permittivity of 5 at the moment the tension s applied. Figure 3.3b: After the charge carriers moved, the electrodes are charged and there is no voltage drop over the electrodes anymore. The full potential is applied on the gas gap only. Figure 3.3c: The streamer discharge initiated by a charged particle transports electrons and cations towards the anode and cathode respectively.	3-5
177	3.4	Typical oscilloscope pulses in streamer mode (Figure 3.4a) and avalanche mode(Figure 3.4b). In the case of streamer mode, the very small avalanche signal is visible.	3-5
179	3.5	Rate capability comparison for the streamer and avalanche mode of operation. An order of magnitude in rate capability for a maximal efficiency drop of 10% is gained by using the avalanche mode over the streamer mode.	3-6
182	3.6	Possible double-gap RPC layouts: a) "standard" 1D double-gap RPC, as used in CMS experiment, where the anodes are facing each other and a 1D read-out plane is sandwiched in between them, b) double read-out double-gap RPC as used in AT-LAS experiment, where the cathodes are facing each other and 2 read-out planes are used on the outer surfaces. This last layout can offer the possibility to use a 2D reconstruction by using orthogonal read-out planes.	3-7
188	3.7	Comparison of performance of CMS double and single gap RPCs using cosmic muons [44]. Figure 3.7a: Comparison of efficiency sigmoids. Figure 3.7b: Voltage distribution at 95% of maximum efficiency. Figure 3.7c: $\Delta_{10\%}^{90\%}$ distribution. . . .	3-7
191	3.8	Presentation of ALICE MRPC using 250 μm gas gaps, 620 μm outer glass electrodes and 550 μm inner floating electrodes. More details on the labels are given in [45]. . . .	3-8
193	3.9	Particle identification applied to electrons in the STAR experiment. The identification is performed combining ToF and dE/dx measurements [50].	3-9
195	3.10	Comparison of the detector performance of ALICE ToF MRPC [51] at fixed applied voltage (in blue) and at fixed effective voltage (in red). The effective voltage is kept fixed by increasing the applied voltage accordingly to the current drawn by the detector.	3-9
198	3.11	Ratio between total induced and drifting charge have been simulated for single gap, double-gap and multigap layouts [52]. The total induced charge for a double-gap RPC is a factor 2 higher than for a multigap.	3-10
201	3.12	Charge spectra have been simulated for single gap, double-gap and multigap layouts [52]. It appears that when single gap shows a decreasing spectrum, double and multigap layouts exhibit a spectrum whose peak is detached from the origin. The detachment gets stronger as the number of gaps increases.	3-11
205	3.13	The maximal theoretical efficiency is simulated for single gap, double-gap and multi-gap layouts [52] at a constant gap thickness of 2 mm and using an effective Townsend coefficient of 9 mm^{-1}	3-11
208	4.1	Signals from the RPC strips are shaped by the FEE described on Figure 4.1a. Output LVDS signals are then read-out by a TDC module connected to a computer or converted into NIM and sent to scalers. Figure 4.1b describes how these converted signals are put in coincidence with the trigger.	4-3

212	4.2	Description of the principle of a CFD. A comparison of threshold triggering (left) 213 and constant fraction triggering (right) is shown in Figure 4.2a. Constant fraction 214 triggering is obtained thanks to zero-crossing technique as explained in Figure 4.2b. 215 The signal arriving at the input of the CFD is split into three components. A first 216 one is delayed and connected to the inverting input of a first comparator. A sec- 217 ond component is connected to the noninverting input of this first comparator. A 218 third component is connected to the noninverting input of another comparator along 219 with a threshold value connected to the inverting input. Finally, the output of both 220 comparators is fed through an AND gate.	4-4
221	4.3	(4.3a) Extrapolation from 2016 data of single hit rate per unit area in the barrel 222 region. (4.3b) Extrapolation from 2016 data of single hit rate per unit area in the 223 endcap region.	4-6
224	4.4	Background Fluka simulation compared to 2016 Data at $L = 10^{34} \text{ cm}^{-2} \cdot \text{s}^{-1}$ in 225 the fourth endcap disk region. A mismatch in between simulation and data can be 226 observed. [To be understood.]	4-7
227	4.5	Layout of the test beam zone called X5c GIF at CERN. Photons from the radioactive 228 source produce a sustained high rate of random hits over the whole area. The zone is 229 surrounded by 8 m high and 80 cm thick concrete walls. Access is possible through 230 three entry points. Two access doors for personnel and one large gate for material. 231 A crane allows installation of heavy equipment in the area.	4-8
232	4.6	^{137}Cs decays by β^- emission to the ground state of ^{137}Ba (BR = 5.64%) and via the 233 662 keV isomeric level of ^{137}Ba (BR = 94.36%) whose half-life is 2.55 min.	4-9
234	4.7	Floor plan of the GIF++ facility. When the facility downstream of the GIF++ takes 235 electron beam, a beam pipe is installed along the beam line (z-axis). The irradiator 236 can be displaced laterally (its center moves from $x = 0.65$ m to 2.15 m), to increase 237 the distance to the beam pipe.	4-9
238	4.8	Simulated unattenuated current of photons in the xz plane (Figure 4.8a) and yz plane 239 (Figure 4.8b) through the source at $x = 0.65$ m and $y = 0$ m. With angular correction 240 filters, the current of 662 keV photons is made uniform in xy planes.	4-10
241	4.9	Description of the RPC setup. Dimensions are given in mm. A tent containing RPCs 242 is placed at 1720 mm from the source container. The source is situated in the center 243 of the container. RE-4-2-BARC-161 chamber is 160 mm inside the tent. This way, 244 the distance between the source and the chambers plan is 2060 mm. Figure 4.9a 245 provides a side view of the setup in the xz plane while Figure 4.9b shows a top view 246 in the yz plane.	4-11
247	4.10	RE-4-2-BARC-161 chamber is inside the tent as described in Figure 4.9. In the top 248 right, the two scintillators used as trigger can be seen. This trigger system has an 249 inclination of 10° relative to horizontal and is placed above half-partition B2 of the 250 RPCs. PMT electronics are shielded thanks to lead blocks placed in order to protect 251 them without stopping photons from going through the scintillators and the chamber.	4-12
252	4.11	Hit distributions over all 3 partitions of RE-4-2-BARC-161 chamber is showed on 253 these plots. Top, middle and bottom figures respectively correspond to partitions A, 254 B, and C. These plots show that some events still occur in other half-partitions than 255 B2, which corresponds to strips 49 to 64, in front of which the trigger is placed, con- 256 tributing to the inefficiency of detection of cosmic muons. In the case of partitions 257 A and C, the very low amount of data can be interpreted as noise. On the other hand, 258 it is clear that a little portion of muons reach the half-partition B1, corresponding to 259 strips 33 to 48.	4-13

260	4.12 Results are derived from data taken on half-partition B2 only. On the 18 th of June 261 data has been taken on chamber RE-2-BARC-161 at building 904 (Prevessin 262 Site) with cosmic muons providing us a reference efficiency plateau of $(97.54 \pm$ 263 $0.15)\%$ represented by a black curve. A similar measurement has been done at GIF 264 on the 21 st of July with the same chamber giving a plateau of $(78.52 \pm 0.94)\%$ 265 represented by a red curve.	4-14
266	4.13 Representation of the layout used for the simulations of the test setup. The RPC is 267 represented as a yellow trapezoid while the two scintillators as blue cuboids looking 268 at the sky. A green plane corresponds to the muon generation plane within the sim- 269 ulation. Figure 4.9a shows a global view of the simulated setup. Figure 4.9b shows 270 a zommed view that allows to see the 2 scintillators as well as the full RPC plane.	4-15
271	4.14 γ flux $F(D)$ is plot using values from table 4.1. As expected, the plot shows similar 272 attenuation behaviours with increasing distance for each absorption factors.	4-18
273	4.15 Figure 4.15a shows the linear approximation fit done via formulae 4.7 on data from 274 table 4.2. Figure 4.15b shows a comparison of this model with the simulated flux 275 using a and b given in figure 4.15a in formulae 4.4 and the reference value $D_0 =$ 276 50cm and the associated flux for each absorption factor F_0^{ABS} from table 4.1	4-20
277	4.16 Dose measurements has been done in a plane corresponding to the tents front side. 278 This plan is 1900 mm away from the source. As explained in the first chapter, a 279 lens-shaped lead filter provides a uniform photon flux in the vertical plan orthogonal 280 to the beam direction. If the second line of measured fluxes is not taken into account 281 because of lower values due to experimental equipments in the way between the 282 source and the tent, the uniformity of the flux is well showed by the results.	4-22
283	4.17	4-23
284	4.18 Evolution of the maximum efficiency for RE2 (4.18a) and RE4 (4.18b) chambers 285 with increasing extrapolated γ rate per unit area at working point. Both irradiated 286 (blue) and non irradiated (red) chambers are shown.	4-25
287	4.19 Evolution of the working point for RE2 (4.19a) and RE4 (4.19b) with increasing 288 extrapolated γ rate per unit area at working point. Both irradiated (blue) and non 289 irradiated (red) chambers are shown.	4-25
290	4.20 Evolution of the maximum efficiency at HL-LHC conditions, i.e. a background hit 291 rate per unit area of 300Hz/cm^2 , with increasing integrated charge for RE2 (4.20a) 292 and RE4 (4.20b) detectors. Both irradiated (blue) and non irradiated (red) chambers 293 are shown. The integrated charge for non irradiated detectors is recorded during test 294 beam periods and stays small with respect to the charge accumulated in irradiated 295 chambers.	4-26
296	4.21 Comparison of the efficiency sigmoid before (triangles) and after (circles) irradiation 297 for RE2 (4.21a) and RE4 (4.21b) detectors. Both irradiated (blue) and non irradiated 298 (red) chambers are shown.	4-26
299	4.22 Evolution of the Bakelite resistivity for RE2 (4.22a) and RE4 (4.22b) detectors. Both 300 irradiated (blue) and non irradiated (red) chambers are shown.	4-27
301	4.23 Evolution of the noise rate per unit area for the irradiated chamber RE2-2-BARC-9 302 only.	4-27
303	A.1 (A.1a) View of the front panel of a V1190A TDC module [58]. (A.1b) View of the 304 front panel of a V1718 Bridge module [59]. (A.1c) View of the front panel of a 6U 305 6021 VME crate [60].	A-3
306	A.2 Module V1190A <i>Trigger Matching Mode</i> timing diagram [58].	A-4

307	A.3 Structure of the ROOT output file generated by the DAQ. The 5 branches (<code>EventNumber</code> ,	
308	<code>number_of_hits</code> , <code>Quality_flag</code> , <code>TDC_channel</code> and <code>TDC_TimeStamp</code>) are visible on	
309	the left panel of the ROOT browser. On the right panel is visible the histogram cor-	
310	responding to the variable <code>nHits</code> . In this specific example, there were approximately	
311	50k events recorded to measure the gamma irradiation rate on the detectors. Each	
312	event is stored as a single entry in the <code>TTree</code>	A-10
313	A.4 The effect of the quality flag is explained by presenting the content of <code>TBranch</code>	
314	<code>number_of_hits</code> of a data file without <code>Quality_flag</code> in Figure A.4a and the con-	
315	tent of the same <code>TBranch</code> for data corresponding to a <code>Quality_flag</code> where all TDCs	
316	were labelled as <code>GOOD</code> in Figure A.4b taken with similar conditions. It can be noted	
317	that the number of entries in Figure A.4b is slightly lower than in Figure A.4a due	
318	to the excluded events.	A-12
319	A.5 Using the same data as previously showed in Figure A.4, the effect of the quality	
320	flag is explained by presenting the reconstructed hit multiplicity of a data file with-	
321	out <code>Quality_flag</code> in Figure A.5a and the reconstructed content of the same RPC	
322	partition for data corresponding to a <code>Quality_flag</code> where all TDCs were labelled as	
323	<code>GOOD</code> in Figure A.5b taken with similar conditions. The artificial high content of bin	
324	0 is completely suppressed.	A-12
325	A.6 WebDCS DAQ scan page. On this page, shifters need to choose the type of scan	
326	(Rate, Efficiency or Noise Reference scan), the gamma source configuration at the	
327	moment of data taking, the beam configuration, and the trigger mode. These in-	
328	formation will be stored in the DAQ ROOT output. Are also given the minimal	
329	measurement time and waiting time after ramping up of the detectors is over before	
330	starting the data acquisition. Then, the list of HV points to scan and the number of	
331	triggers for each run of the scan are given in the table underneath.	A-14
332	B.1 Example of expected hit time distributions in the cases of efficiency (Figure B.1a)	
333	and noise/gamma rate per unit area (Figure B.1b) measurements as extracted from	
334	the raw ROOT files. The unit along the x-axis corresponds to ns. The fact that	
335	"the" muon peak is not well defined in Figure B.1a is due to the contribution of all	
336	the RPCs being tested at the same time that don't necessarily have the same signal	
337	arrival time. Each individual peak can have an offset with the ones of other detectors.	
338	The inconsistency in the first 100 ns of both time distributions is an artefact of the	
339	TDCs and are systematically rejected during the analysis.	B-16
340	B.2 The effect of the quality flag is explained by presenting the reconstructed hit multi-	
341	plicity of a data file without <code>Quality_flag</code> . The artificial high content of bin 0 is the	
342	effect of corrupted data.	B-19
343	B.3 Display of the masking tool page on the webDCS. The window on the left allows the	
344	shifter to edit <code>ChannelsMapping.csv</code> . To mask a channel, it only is needed to set the	
345	3rd field corresponding to the strip to mask to 0. It is not necessary for older mapping	
346	file formats to add a 1 for each strip that is not masked as the code is versatile and	
347	the default behaviour is to consider missing mask fields as active strips. The effect	
348	of the mask is directly visible for noisy channels as the corresponding bin turns red.	
349	The global effect of masking strips will be an update of the rate value showed on the	
350	histogram that will take into consideration the rejected channels.	B-24

List of Tables

351

352	3.1 Properties of the most used electrode materials for RPCs.	3-4
353	4.1 Total photon flux ($E\gamma \leq 662$ keV) with statistical error predicted considering a	
354	^{137}Cs activity of 740 GBq at different values of the distance D to the source along	
355	the x-axis of irradiation field [55].	4-17
356	4.2 Correction factor c is computed thanks to formulae 4.5 taking as reference $D_0 =$	
357	50 cm and the associated flux F_0^{ABS} for each absorption factor available in table 4.1. .	4-19
358	4.3 The data at D_0 in 1997 is taken from [55]. In a second step, using Equations 4.8	
359	and 4.9, the flux at D can be estimated in 1997. Then, taking into account the	
360	attenuation of the source activity, the flux at D can be estimated at the time of the	
361	tests in GIF in 2014. Finally, assuming a sensitivity of the RPC to γ $s = 2 \cdot 10^{-3}$,	
362	an estimation of the hit rate per unit area is obtained.	4-21
363	A.1 Inter-process communication cycles in between the webDCS and the DAQ through	
364	file string signals.	A-19

List of Acronyms

365

366

List of Acronyms

367

368

A

369

370

371 AFL

Almost Full Level

372

373

B

374

375

376 BARC

Bhabha Atomic Research Centre

377 BLT

Block Transfer

378 BNL

Brookhaven National Laboratory

379 BR

Branching Ratio

380

381

C

382

383

384 CAEN

Costruzioni Apparecchiature Elettroniche Nucleari S.p.A.

385 CERN

European Organization for Nuclear Research

386 CFD

Constant Fraction Discriminator

387 CMS

Compact Muon Solenoid

388 CSC

Cathode Strip Chamber

389

390

D

391

392

393 DAQ

Data Acquisition

394 DCS

Detector Control Software

395 DQM

Data Quality Monitoring

396 DT

Drift Tube

397

398

F

399

400

401	FEE	Front-End Electronics
402	FEB	Front-End Board
403		
404		
405	G	
406		
407	GE-/-	Find a good description
408	GE1/1	Find a good description
409	GE2/1	Find a good description
410	GEANT	GEometry ANd Tracking - a series of software toolkit platforms developed by CERN
411		
412	GEM	Gas Electron Multiplier
413	GIF	Gamma Irradiation Facility
414	GIF++	new Gamma Irradiation Facility
415		
416		
417	H	
418		
419	HL-LHC	High Luminosity LHC
420	HPL	High-pressure laminate
421	HV	High Voltage
422		
423		
424	I	
425		
426	iRPC	improved RPC
427	IRQ	Interrupt Request
428	ISR	Intersecting Storage Rings
429		
430		
431	L	
432		
433	LEIR	Low Energy Ion Ring
434	LEP	Large Electron-Positron
435	LHC	Large Hadron Collider
436	LS1	First Long Shutdown
437	LS3	Third Long Shutdown
438	LV	Low Voltage
439	LVDS	Low-Voltage Differential Signaling
440		
441		
442	M	
443		
444	MC	Monte Carlo

445	MCNP	Monte Carlo N-Particle
446	ME-/	Find good description
447	ME0	Find good description
448	MRPC	Multigap RPC
449		
450		
451	N	
452		
453	NIM	Nuclear Instrumentation Module logic signals
454		
455		
456	P	
457		
458	PS	Proton Synchrotron
459	PMT	PhotoMultiplier Tube
460		
461		
462	Q	
463		
464	QCD	Quantum Chromodynamics
465	QED	Quantum Electrodynamics
466		
467		
468	R	
469		
470	RE-/	Find a good description
471	RE2/2	Find a good description
472	RE3/1	Find a good description
473	RE3/2	Find a good description
474	RE4/1	Find a good description
475	RE4/2	Find a good description
476	RE4/3	Find a good description
477	RMS	Root Mean Square
478	ROOT	a framework for data processing born at CERN
479	RPC	Resistive Plate Chamber
480		
481		
482	S	
483		
484	SC	Synchrocyclotron
485	SLAC	Stanford Linear Accelerator Center
486	SM	Standard Model
487	SPS	Super Proton Synchrotron

488		
489		
490	T	
491		
492	TDC	Time-to-Digital Converter
493	ToF	Time-of-flight
494		
495		
496	W	
497		
498	webDCS	Web Detector Control System

1

Introduction

499

500

⁵⁰¹ **1.1 A story of High Energy Physics**

⁵⁰² **1.2 Organisation of this study**

2

503

504

Investigating the TeV scale

505 „We may regard the present state of the universe as the effect of the
506 past and the cause of the future. An intellect which at any given mo-
507 ment knew all of the forces that animate nature and the mutual posi-
508 tions of the beings that compose it, if this intellect were vast enough
509 to submit the data to analysis, could condense into a single formula
510 the movement of the greatest bodies of the universe and that of the
511 lightest atom; for such an intellect nothing could be uncertain and
512 the future just like the past would be present before its eyes.”

513

514 - Pierre Simon de Laplace, *A Philosophical Essay on Probabilities*, 1814

515 Throughout history, physics experiment became more and more powerful in order to investigate
516 finer details of nature and helped understanding the elementary blocks of matter and the fundamental
517 interactions that bond them in the microscopic world. Nowadays, the Standard Model (SM) of
518 particle physics is the most accurate theory designed to explain the behaviour of particles and was
519 able to make very precise predictions that are constantly verified, although some hints of new physics
520 are visible as bricks are still missing to have a global comprehension of the Universe.

521 To highlight the limits of the SM and test the different alternative theories, ever more powerful
522 machines are needed. This is in this context that the Large Hadron Collider (LHC) has been thought
523 and built to accelerate and collide particles at energies exceeding anything that had been done before.
524 Higher collision energies and high pile-up imply the use of enormous detectors to measure the
525 properties of the interaction products. The Compact Muon Solenoid (CMS) is a multipurpose ex-
526 periment that have been designed to study the proton-proton collisions of the LHC and give answers
527 on various high energy physics scenari. Nevertheless, the luminosity delivered by the collider will
528 in the future be increased to levels beyond the original plans to improve its discovery potential giv-
529 ing no choice to experiments such as CMS to upgrade their technologies to cope with the increased
530 radiation levels and detection rates.

531 **2.1 The Standard Model of Particle Physics**

532 In this early 21st century it is now widely accepted that matter is made of elementary blocks referred
533 to as *elementary particles*. The physics theory that classifies and describes the best the behaviour
534 and interaction of such elementary particles is the so called Standard Model that formalizes 3 of
535 the 4 fundamental interactions (electromagnetic, weak and strong interactions). It's development
536 took place during the 20th century thanks to a strong collaboration in between the theoretical and
537 experimental physicists.

538 **2.1.1 A history of particle physics**

539 The idea that nature is composed of elementary bricks, called *atomism*, is not contemporary as it
540 was already discussed by Indian or Greek philosophers during antiquity. In Greece, atomism has
541 been rejected by Aristotelianism as the existance of *atoms* would imply the existance of a void that
542 would violate the physical principles of Aristotle philosophy. Aristotelianism has been considered
543 as a reference in the european area until the 15th century and the italian *Rinascimento* where antic
544 text and history started to be more deeply studied. The re-discovery of Platon's philosophy would
545 allow to open the door to alternative theories and give a new approach to natural sciences where
546 experimentation would become central. A new era of knowledge was starting. By the begining of
547 the 17th century, atomism was re-discovered by philosophers and the very first attempt to estimate
548 an *atom* size would be provided by Magnetus in 1646. Although his *atoms* correspond to what would
549 nowadays be called *molecules*, Magnetus achieved feats by calculating that the number of molecules
550 in a grain of incense would be of the order of 10^{18} simply by considering the time necessary to smell
551 it everywhere in a large church after the stick was lit on. It is now known that this number only falls
552 short by 1 order of magnitude.

553 An alternative philosophy to atomism popularized by Descartes was corpuscularianism. Built on
554 ever divisible corpuscles, contrary to atoms, it's principles would be mainly used by alchemists like
555 Newton who would later develop a corpuscular theory of light. Boyle would combine together ideas
556 of both atomism or corpuscularianism leading to mechanical philosophy. The 18th century have

seen the development of engineering providing philosophical thought experiments with repeatable demonstration and a new point of view to explain the composition of matter and Lavoisier would greatly contribute to chemistry and atomism by publishing in 1789 a list of 33 chemical elements corresponding to what is now called *atoms*. In the early 19th century Dalton would summarize the knowledge on composition of matter and Fraunhofer would invent the spectrometer and discover the spectral lines. The rise of atomic physics, chemistry and mathematical formalism would unravel the different atomic elements and ultimately, the 20th century would see the very first sub-atomic particles.

Discovery of the inner structure of the atom

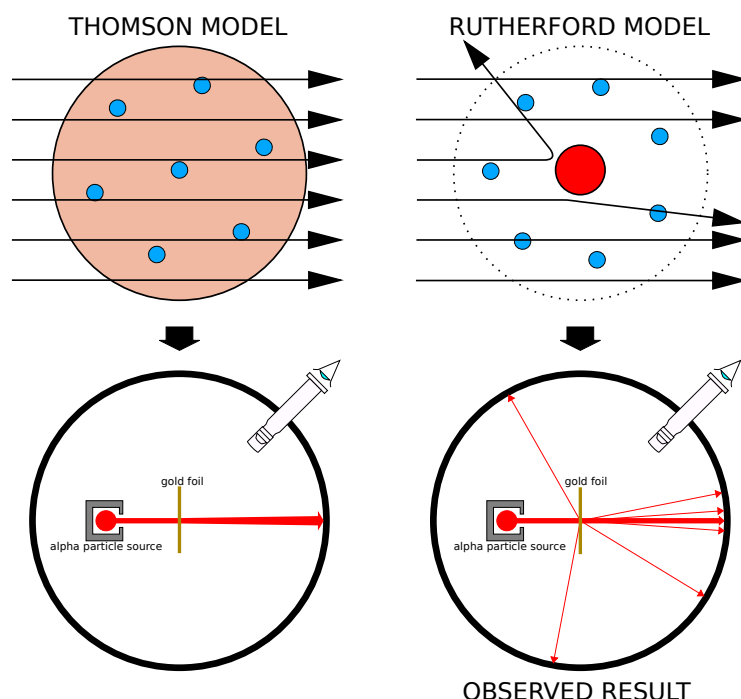


Figure 2.1: Through the gold foil experiment Rutherford could show that most of the mass of atoms was contained in a positively charged nucleus and could then propose a more accurate atomic model than that of Thomson.

The negative *electron* would be the first to be discovered in 1897 by Thomson after 3 decades of research on cathode rays by proving that the electrification observed in an electroscope, as reported by Perrin, was due to the rays themselves and that they had to be composed of electrically charged particles. In 1900, Becquerel would show the *beta rays* emitted by radium had the same charge over mass ratio than what measured by Thomson for cathode rays, pointing to electrons as a constituent of atoms. In 1907, Rutherford and Royds showed that *alpha* particles, once captured in a tube and subjected to an electric spark causing an electron avalanche, where helium ions as they could combine with 2 electrons to form a ${}^4\text{He}$. This discovery was directly followed by the constraint of the atom structure in 1909 through the gold foil experiment in which the deflection angle of alpha particles fired at a very thin gold foil was measured and highlighted atoms where mainly empty with

576 nearly all its mass contained into a tiny positively charged *nucleus*. With these two observations,
 577 he could formulate the Rutherford model of the atom in 1911, shown together with the Thomson
 578 plum pudding model in Figure 2.1. The link in between atomic number and number of positive and
 579 negative charges contained into the atoms would fast be understood and the different kind of element
 580 transmutation appeared to be purely nuclear processes making clear that the electromagnetic nature
 581 of chemical transformation could not possibly change nuclei. Thus a new branch in physics appeared
 582 to study nuclei exclusively: the nuclear physics.

583 Moreover, in 1913 quantum physics would be introduced into the atomic model by Bohr based
 584 on the assumptions of Plank to explain spectral lines, and other observed quantum effects. The same
 585 year, Moseley would confirm Borh's model and Debye would extend it by introducing elliptical
 586 orbits.

587 By studying alpha emission and the product of their interaction with nitrogen gas, Rutherford
 588 reported in 1919 the very first nuclear reaction leading to the discovery that the hydrogen nucleus was
 589 composed of a single positively charged particle that was later baptised *proton*. This idea came from
 590 1815 Prout's hypothesis proposing that all atoms are composed of "*protyles*" (i.e. hydrogen atoms).
 591 By using scintillation detectors, Rutherford could highlight typical hydrogen nuclei signature and
 592 understand that the impact of alpha particles with nitrogen would knock out an hydrogen nucleus
 593 and produce an oxygen 17, as explicated in Formula 2.1 and would then postulate that protons are
 594 building bricks of all elements.



595 With this assumption and the discovery of isotopes together with Aston, elements with identical
 596 atomic number but different masses, Rutherford would propose that all elements' nuclei but hydrogen's are composed of both charged particles, protons, and of chargeless particles, which he called
 597 *neutrons*, and that these neutral particles would help maintaining nuclei as one, as charged protons
 598 were likely to electrostatically repulse each other, and introduced the idea of a new force, a *nuclear*
 599 force. Though the first idea concerning neutrons was a bond state of protons and electrons as it was
 600 known that the beta decay, emitting electrons, was taking place in the nucleus, it was then showed
 601 that such a model would hardly be possible due to Heisenberg's uncertainty principle and by the
 602 recently measured *spin* of both protons and electrons. The spin, discovered through the study of
 603 the emission spectrum of alkali metals, would be understood as a "two-valued quantum degree of
 604 freedom" and formalized by Pauli and extended by Dirac, to take the relativist case into account.
 605 Measured to be $\frac{1}{2}\hbar$ for both, it was impossible to arrange an odd number of half integer spins and
 606 obtain a global nucleus spin that would be integer. Finally, in 1932, following the discovery of a new
 607 neutral radiation, Chadwick could discover the neutron as an uncharged particle with a mass similar
 608 to that of the proton whose half integer spin would reveal to be the solution to explain the nuclear
 609 spin.
 610

611 Development of the Quantum Electrodynamics

612 Historically, the development of the quantum theory revolved around the question of emission and
 613 absorption of discrete amount of energy through light. Einstein used the initial intuition of Plank
 614 about the black-body radiation to develop in 1905 a model to explain the photoelectric effect in
 615 which light was described by discrete quanta now called *photons*. For this model, Einstein introduced
 616 the concept of wave-particle duality as classical theory was not able to describe the phenomenon.
 617 With the new understanding of atoms and of their structure, classical theories also proved unable

618 to explain atoms stability. Indeed, using classical mechanics, electrons orbiting around a nucleus
 619 should radiate an energy proportional to their angular momentum and thus lose energy through
 620 time and the spectrum of energy emission should then be continuous, but it was known since the
 621 19th century and the discovery of spectral lines that the emission spectrum of material was discrete.

622 This was Bohr who first suggested that a quantum description of the atom was necessary in 1913.
 623 Using the correspondence principle stating that at large enough numbers the quantum calculations
 624 should give the same results than the classical theory, he proposed the very first quantum model
 625 of the hydrogen atom explaining the line spectrum by introducing the principal quantum number
 626 n describing the electron shell. This model would then be improved by Sommerfeld that would
 627 quantize the z-component of the angular momentum, leading to the second and third quantum
 628 numbers, or azimuthal and magnetic quantum number, l and m defining for the second the orbital
 629 angular momentum of the electrons on their shells and thus, the shape of the orbital, and for the third
 630 the available orbital on the subshell for each electron. Nevertheless, although the model was not only
 631 limited to spherical orbitals anymore, making the atom more realistic, the Zeeman effect couldn't be
 632 completely explained by just using n , l and m . A solution would be brought after the discovery of
 633 Pauli in 1924, as Uhlenbeck, Goudsmit, and Kramers proposed in 1925 the idea of intrinsic rotation
 634 of the electron, introducing a new angular momentum vector associated to the particle itself, and
 635 not to the orbital, and associated to a new quantic number s , the *spin* projection quantum number
 636 explaining the lift of degeneracy to an even number of energy levels.

637 The introduction of the *spin* happened 1 year after another attempt of improvement of the theory
 638 was made by De Broglie in his PhD thesis. The original formulation of the quantum theory only
 639 considered photons as energy quanta behaving as both waves and particles. De Broglie proposed
 640 that all matter are described by waves and that their momentum is proportional to the oscillation of
 641 quantized electromagnetic field oscillators. This interpretation was able to reproduce the previous
 642 version of the quantum energy levels by showing that the quantum condition involves an integer
 643 multiple of 2π , as shown by Formula 2.2.

$$p = \hbar k \Leftrightarrow \int pdx = \hbar \int kdx = 2\pi\hbar n \quad (2.2)$$

644 Although the intuition of De Broglie about the wave-particle duality of all matter, his interpretation
 645 was semiclassical and it's in 1926 that the first fully quantum mechanical wave-equation would
 646 be introduced by Schrödinger to describe electron-like particles, reproducing the previous semiclassical
 647 formulation without inconsistencies. This complexe equation describes the evolution of the
 648 wave function Ψ of the quantum system, defined by its position vector \mathbf{r} and time t as an energy
 649 conservation law, in which the hamiltonian of the system \hat{H} is explicit, by solving the Equation 2.3.

$$i\hbar \frac{\partial}{\partial t} |\Psi(\mathbf{r}, t)\rangle = \hat{H} |\Psi(\mathbf{r}, t)\rangle \quad (2.3)$$

650 In 1927, Dirac would go further in his paper about emission and absorption of radiation by
 651 proposing a second quantization not only of the physical process at play but also of the electromagnetic
 652 field, providing the ingredients to the first formulation of *Quantum Electrodynamics (QED)*
 653 and the description of photon emission by electrons dropping into a lower energy state in which the
 654 final number of particles is different than the initial one. To complete this model to the many-body
 655 wave functions of identical particles, Jordan included creation and annihilation operators for fields
 656 obeying Fermi-Dirac statistics leading to a model describing particles that would be referred to as
 657 *fermions*. Nevertheless, in order to properly treat electromagnetism, the incorporation of the relativ-

ity theory developed by Einstein. Including gravity into quantum physics still is a challenge nowadays, but in 1928 Pauli and Jordan would show that special relativity's coordinate transformations could be applied to quantum fields as the field commutators were Lorentz invariant. Finally derived the same year, the Dirac equation, shown as Equation 2.4, similarly to Schrödinger's equation, is a single-particle equation but it incorporates special relativity in addition to quantum mechanics rules. It features the 4×4 gamma matrices γ^μ built using 2×2 Pauli matrices and unitary matrix, the 4-gradient ∂_μ , the rest mass m of any half integer spin massive particle described by the wave function $\psi(x, t)$, also called a Dirac spinor, and the speed of light c . In addition to perfectly reproduce the results obtained with quantum mechanics so far, it also provided with *negative-energy solutions* that would later be interpreted as a new form of matter, *antimatter* and give a theoretical justification to the Pauli equation that was phenomenologically constructed to account for the spin as in the non-relativistic limit, the Dirac equation is similar.

$$i\hbar\gamma^\mu\partial_\mu\psi - mc\psi = 0 \quad (2.4)$$

The successes of the QED was soon followed with theoretical problems as computations of any physical process involving photons and charged particles were showed to be only reliable at the first order of perturbation theory. At higher order of the theory, divergent contributions were appearing giving nonsensical results. Only two effects were contributing to these infinities.

- The self-energy of the electron (or positron), the energy that the particle has due its own interaction with its environment.
- The vacuum polarization, virtual electron–positron pairs produced by a background electromagnetic field in the vacuum which is not an "empty" space. These virtual pairs affect the charge and current distributions generated by the original electromagnetic field.

Solving this apparent problem was done by carefully defining the concepts of each observables, for example mass or charge, as these quantities are understood within the context of a non-interacting field equation, and that from the experiment point of view, they are abstractions as what is measured are "renormalized observables" shifted from there "bare" value by the interaction taking place in the measuring process. The infinities needed to be connected to corrections of mass and charge as those are fixed to finite values by experiment. This was the intuition of Bethe in 1947 who successfully computed the effect of such *renormalization* in the non-relativist case. Fully covariant formulations of QED including renormalization was achieved by 1949 by Tomonaga, Schwinger, Feynman and Dyson and Feynman is now famous for his association of diagrams to the term of the scattering matrix, greatly simplifying the representation and computation of interactions as the diagrams directly corresponded the measurable physical processes and would then be used in every quantum field theories. With the resolution of infinities, QED had mostly reached its final form, being still today the most accurate physical theory and would serve as a model to build all other quantum field theories.

Development of the quark model and Quantum Chromodynamics

To explain the nuclear force that holds *nucleons* (protons and neutrons) together, Yukawa theoretically proposed in 1934 the existence of a force carrier called *meson* due to it's predicted mass in the range in between the electron and nucleon masses. Discovered in 1936 by Anderson and Neddermeyer, and confirmed using bubble chambers in 1937 by Street and Stevenson, a first meson

698 candidate was observed in the decay products of cosmic rays. Assuming it had the same electric
 699 charge than electrons and protons, this particle was observed to have a curvature due to magnetic
 700 field that was sharper than protons but smoother than electrons resulting in a mass in between that
 701 of electrons and protons. But its properties were not compatible with Yukawa's theory, which was
 702 emphasized by the discovery of a new candidate in 1947, again in cosmic ray products using photo-
 703 graphic emulsions.

704 This new candidate, although it had a similar mass than the already believed *meson*, would rather
 705 decay into it. For distinction, the first candidate would then be renamed "*mu meson*" when the second
 706 would be the "*pi meson*". The *mu meson* was behaving like a heavy electron and didn't participate
 707 in the strong interaction whereas the pion was believed to be the carrier of the nuclear interaction.
 708 This lead to classify the *mu* in a new category of particles called *leptons* together with the electron
 709 that shared similar properties and *the neutrino*, and be renamed *muon*. The *pi meson* was finally
 710 found to be a triplet of particles: a positively charged, a negatively charged, and a neutral particle.
 711 The neutral *pi meson* has been more difficult to identify as it wouldn't leave tracks on emulsions nor
 712 on bubble chambers and needed to be studied via it's decay products. It was ultimately identified in
 713 University of California's cyclotron in 1950 through the observation of its decay into 2 photons.

714 Also discovered in 1947 but in cloud chamber photographs, the *K meson* as also been an im-
 715 portant step towards the establishment of the Standard Model. A triplet of particle, 2 charged and a
 716 neutral, with a mass roughly half that of a proton, were reported. These particles were baptised *K*
 717 *meson* in contrast to the "light" *pi* and *mu* "L-mesons". The particularity of the *K* were there very
 718 slow decays with a typical lifetime of the order of 10^{-10} s much greater than the 10^{-23} s of *pi*-proton
 719 reactions. The concept of *strangeness*, a new quantum number was then introduced by Pais as an
 720 attempt to explain this phenomenon as *strange* particles appeared as a pair production of a strange
 721 and anti-strange particle.

722 With the development of synchrotrons, the particle *zoo* would grow to several dozens during the
 723 1950s as higher energies were reachable through acceleration. In 1961, a first classification system,
 724 called Eightfold Way, was proposed by Gell-Mann and finding its roots in the Gell-Mann–Nishijima
 725 formula, which relates the electric charge Q , the third component of the isospin I_3 , the *baryon*
 726 number B and the strangeness S , as explicitated in Formula 2.5. The isospin was a quantum number
 727 introduced in 1932 to explain symmetries of the newly discovered neutron using representation
 728 theory of SU(2). The baryon number, was introduced by Nishijima as a quantum number for baryons,
 729 i.e. particles of the same family as nucleons. The mesons were classified in an octet and baryons of
 730 spin $\pm \frac{1}{2}$ and $\pm \frac{3}{2}$ were respectively classified into an octet and a decuplet, as shown in Figure 2.2. To
 731 complete the baryon decuplet, Gell-Mann predicted the existance of baryon Ω^- which would later
 732 be discovered in 1964.

$$Q = I_3 + \frac{1}{2}(B + S) \quad (2.5)$$

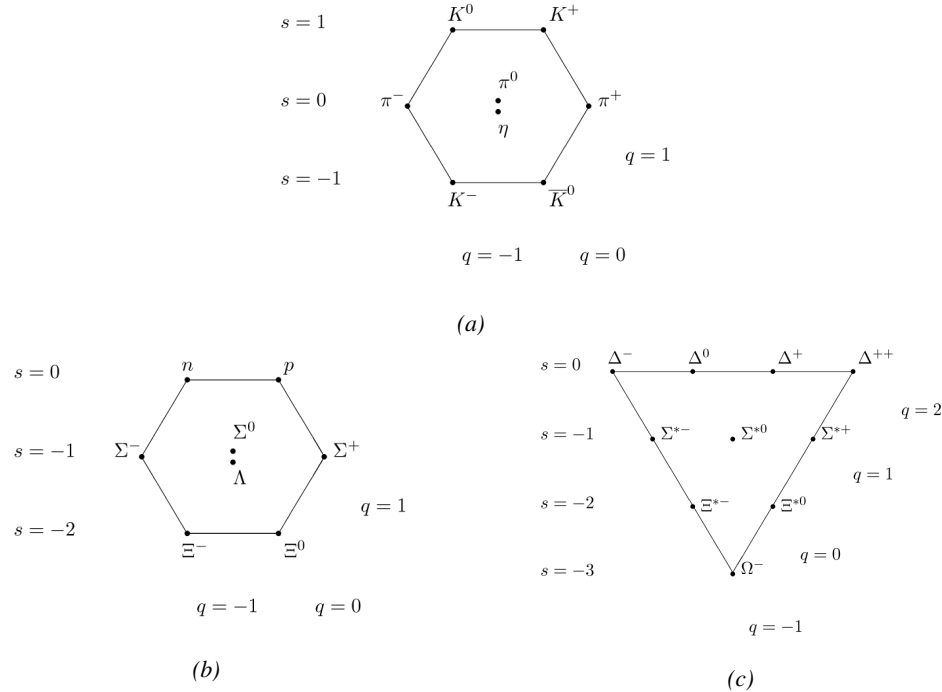


Figure 2.2: Figure 2.2a: Meson octet. Figure 2.2b: Baryon octet. Figure 2.2c: Baryon decuplet.

Strong of this classification using an SU(3) flavor symmetry, Gell-Mann, and independently Zweig, would propose a full theoretical model in which *hadrons* (strongly interacting particles, i.e. mesons and baryons) were not elementary particles anymore. They would rather be composed with 3 flavors of particles called *quarks* and there anti-particles. The 3 flavors were called *up*, *down* and *strange*. *Up* and *down* would be used to explain the nucleons and non-strange mesons, while *strange* would come into the composition of hadrons showing strangeness. *Up* and *down* flavors would be discovered in 1968 thanks to the deep inelastic scattering experiments conducted at the Stanford Linear Accelerator Center (SLAC), and *strange* could only be indirectly validated even though it provided a robust explanation to *kaon* (K) and *pion* (π). However, in the decade following the Gell-Mann-Zweig quark model proposition, several improvement to the model were brought, first by Glashow and Bjorken the same year that predicted the existence of a fourth quark flavor, the *charm*, that would equalize the then known number of quarks and leptons and finally in 1973 by Kobayashi and Maskawa that would increase the number of quarks to 6 to explain the experimental observation of CP violation. These two quarks would be referred to as *top* and *bottom* for the first time in 1975. It's only after these additions to the quark model that finally the *charm* would be discovered in 1974 at both SLAC and Brookhaven National Laboratory (BNL). A meson where the *charm* was bound with an *anti-charm*, called J/ψ , would help convince the physics community of the validity of the model. The *top* would be discovered soon after in 1977 in Fermilab and indicate the existence of the *bottom* that would resist to discovery until Fermilab's experiments CDF and D \emptyset in 1995 due to its very large mass and the energy needed to produce it.

As remarked by Struminsky, the original quark model proposal composed of 3 quarks should possess an additional quantum number due to mesons such as Ω^- or Δ^{++} . Indeed, these mesons are composed of 3 identical quarks, respectively 3 *strange* and *up* quark, with parallel spins, which

should be forbidden by the exclusion principle. Independentle, Greenberg and Han-Nambu proposed an additional SU(3) degree of freedom possessed by the quarks, that would later be refered to as *color charge gauge*, that could interact through *gluons*, the gauge boson octet corresponding to this degree of freedom. Nevertheless, as observing free quarks proved to be impossible, two visions of the quarks were argued mainly due to the failures to observe these particles free to prove their existence. On one side, Gell-Mann proposed to see quarks as mathematical construct instead of real particles, as they are always confined, implying that quantum field theory would not describe entirely the strong interaction. Opposed to this vision, Feynman on the contrary argued that quarks were real particles, that he would call *partons*, that should be described as all other particles by a distribution of position and momentum. The implications of quarks as point-like particles would be verified at SLAC and the concept of *color* would be added to the quark model in 1973 by Fritzsch and Leutwyler together with Gell-Mann to propose a description of the strong interaction through the theory of Quantum Chromodynamics (QCD). The discovery the same year of asymptotic freedom within the QCD by Groos, Politzer and Wilczek, allowed for very precise predictions thanks to the perturbation theory. Nowadays, the confinement of quarks is studied in experiments such as ALICE, through exploration of the quark-gluon plasma.

772 The Weak interaction, spontaneous symmetry breaking, the Higgs mechanism and the Elec- 773 troweak unification

The weak interaction is the process that causes radioactive decays. Thanks to the neutron discovery, Fermi could explain in 1934 the beta radiations through the beta decay process in which the neutron decays into a proton by emitting an electron. Though the missing energy observed during this process triggered a huge debate about the apparent non conservation of energy, momentum and spin of the process, Fermi, as Pauli before him, proposed that the missing energy was due to a neutral not yet discovered particle that would then be baptised *neutrino*. The impossibility to detect such a particle would leave some members of the scientific community sceptical, but hints of energy conservation and of the existence of the neutrino were provided by measuring the energy spectrum of electrons emitted through beta decay, as there was a strict limit on their energy. It's only 30 years later in 1953 that it would be discovered by the team of Cowan and Reines using the principle of inverse beta decay described through Formula 2.6. The experiment consisted in placing water tanks sandwiched in between liquid scintillators near a nuclear reactor with an estimated neutrino flux of $5 \times 10^{13} \text{ s}^{-1} \text{ cm}^{-2}$. However, in order to explain the absence of some reactions in the experiment of Cowan and Reines, and constraint the beta decay theory of Fermi and extend it to the case of the muon, Konopinski and Mahmoud proposed in 1953 that the muon decay would eject a particle similar to the neutrino and thus predicted the existence of a muon neutrino that would be different than the one involved in the beta decay, related to the electron. With this, the idea of lepton number would arise. The muon neutrino would successfully be detected in 1962 by Lederman, Schwartz and Steinberger.

$$\bar{\nu} + p \rightarrow n + e^+ \quad (2.6)$$

The theory could not be valid though as the probability of interaction, called cross-section, would have been increasing without bond with the square of the energy. Fermi assumed in a two vector current coupling but Lee and Yang noted that an axial current could appear and would violate parity. The experiment of Wu in 1956 would confirm the parity violation and Gamow and Teller would try to account for it by describing Fermi's interaction through allowed (parity-violating) and superallowed

798 (parity-conserving) decays. But the success of QED as a quantum field theory would spark the
799 development of such a theory to describe the weak interaction.

800 As previously discussed, the great success of QED was built on an underlying symmetry, interpreted
801 as a gauge invariance so that the effect of the force is the same in all space-time coordinates,
802 and of the possibility to renormalize it in order to absorb the infinities. Independently in 1958,
803 Glashow, and Salam and Ward used 1957 Schwinger ideas about vector intermediary for the decay
804 processes, could find a way to unite both the electromagnetic and weak interaction into a gauge
805 theory involving 4 gauge bosons, 3 of which were massive and carried out the weak interaction and
806 a massless boson carrying the electromagnetic interaction. Among the 3 massive bosons, 2 were
807 charged and 1 was neutral, similarly to the previously theorized *pi meson* vector of the Yukawa
808 model and all have a mass much greater than nucleons and thus a very short life time implying a
809 finite very short range contrary to the contact interaction originally proposed by Fermi.

810 Breakthrough in other fields of physics contributed in giving theoretical support and interpretation
811 to the unified electroweak theory. The stepping stone would be the use of spontaneous symmetry
812 breaking that was inspired to Nambu at the end of the 1950s following the development of the BCS
813 superconductivity mechanism in 1957. Cooper had shown that BCS pairs, pairs of electrons bound
814 together at low temperature, could have lower energy than the Fermi energy and where responsible
815 for superconductivity. This lead to the discovery of Goldstone-Nambu bosons as a result of the
816 spontaneous breaking of the chiral symmetry in a theory describing nucleons and mesons developed
817 by Nambu and Jona-Lasinio in 1961, and now understood as a low-energy approximation of
818 QCD. Similarly to mechanism of energy gap appearance in superconductivity, the nucleon mass
819 is suggested to the result of a self-energy of a fermion field and is studied through a four-fermion
820 interaction in which, as a consequence of the symmetry, bound states of nucleon-antinucleon pairs
821 appear and can be regarded as virtual pions. Though the symmetry is maintained in the equations,
822 the ground state is not preserved. Goldstone would later the same year show that the bound states
823 corresponds to spinless bosons with zero mass.

824 Although the model in itself didn't revolutionize particle physics, spontaneous symmetry breaking
825 would be generalized to quantum field theories. As all fundamental interactions are described
826 using gauge theories based on underlying symmetries, processes such as the chiral symmetry breaking
827 would be introduced soon after the publication of Nambu and Jona-Lasinio. In 1962, Anderson,
828 following an idea of Schwinger who suggested that zero-mass vector bosons were not necessarily
829 required to describe the conservation of baryons contrary to the bosons emerging from chiral symmetry
830 breaking, discussed the implications of spontaneous symmetry breaking in particles physics.
831 A model was finally independently built in 1964 by Brout and Englert, Higgs, and Guralnik, Hagen,
832 and Kibble, who discovered that combining an additional field into a gauge theory in order to break
833 the symmetry, the resulting gauge bosons acquire a nonzero mass. Moreover, Higgs stated that this
834 implied the existence of at least one new massive, i.e. self-interacting, scalar boson, that are now
835 known as *Higgs bosons* corresponding to this additional field. The Higgs mechanism today specifically
836 refers to the process through which the gauge bosons of the weak interaction acquire mass. In
837 1968, Weinberg could point to the Higgs mechanism to integrate a Higgs field into a new version
838 of the electroweak theory in which the spontaneous symmetry breaking mechanism of the Higgs
839 field would explicitly explain the masses of the weak interaction gauge bosons and the zero-mass
840 of photons.

841 **2.1.2 Construction and test of the model**

842 **2.1.3 Investigating the TeV scale**

843 **2.2 The Large Hadron Collider & the Compact Muon Solenoid**

844 Throughout its history, CERN has played a leading role in high energy particle physics. Large re-
845 gional facilities such as CERN were thought after the second world war in an attempt to increase
846 international scientific collaboration and allows scientists to share the forever increasing costs of
847 experiment facilities required due to the need for increasing the energy in the center of mass to
848 deeper probe matter. The construction of the first accelerators at the end of the 50s, the Synchro-
849 cyclotron (SC) and the Proton Synchrotron (PS), was directly followed by the first observation of
850 antinuclei in 1965 [1]. Strong from the experience of the Intersecting Storage Rings (ISR), the very
851 first proton-proton collider that showed hints that protons are not elementary particles, the Super
852 Proton Synchrotron (SPS) was built in the 70s to investigate the structure of protons, the preference
853 for matter over antimatter, the state of matter in the early universe or exotic particles, and lead to
854 the discovery in 1983 of the W and Z bosons [2–5]. These newly discovered particles and the elec-
855 troweak interaction would then be studied in details by the Large Electron-Positron (LEP) collider
856 that will help to prove in 1989 that there only are three generations of elementary particles [6]. The
857 LEP would then be dismantled in 2000 to allow for the LHC to be constructed in the existing tunnel.

858 **2.2.1 LHC, the most powerful particle accelerator**

859 The LHC has always been considered as an option to the future of CERN. At the moment of the
860 construction of the LEP beneath the border between France and Switzerland, the tunnel was built in
861 order to accomodate what would be a Large Hadron Collider with a dipole field of 10 T and a beam
862 energy in between 8 and 9 TeV [7] directly followed in 1985 with the creation of a 'Working Group
863 on the Scientific and Technological Future of CERN' to investigate such a collider [8]. The decision
864 was finally taken almost 10 years later, in 1994, to construct the LHC in the LEP tunnel [9] and the
865 approval of the 4 main experiments that would take place at the 4 interaction points would come in
866 1997 [10] and 1998 [11]:

- 867 • ALICE [12] has been designed in the purpose of studying quark-gluon plasma that is believed
868 to have been a state of matter that existed in the very first moment of the universe.
- 869 • ATLAS [13] and CMS [14] are general purpose experiments that have been designed with
870 the goal of continuing the exploration of the Standard Model and investigate new physics.
- 871 • LHCb [15] has been designed to investigate the preference of matter over antimatter in the
872 universe through the CP violation.

873 These large scale experiments, as well as the full CERN accelerator complex, are displayed on
874 Figure 2.3.

CERN's Accelerator Complex

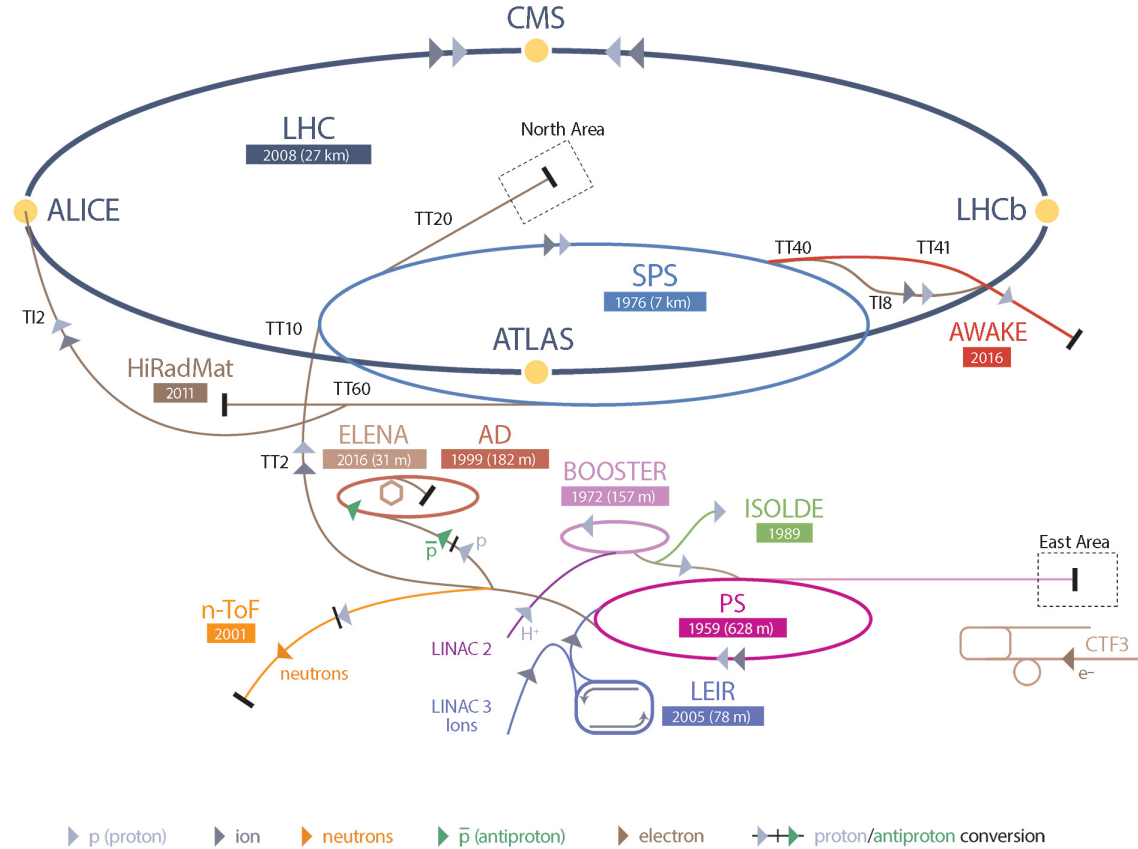


Figure 2.3: CERN accelerator complex.

875 The LHC is a 27 km long hadron collider and the most powerful accelerator used for particle
 876 physics since 2008 [16]. The LHC was originally designed to collide protons at a center-of-mass
 877 energy of 14 TeV and luminosity of $10^{34} \text{ cm}^{-2}\text{s}^{-1}$, as well as Pb ions at a center-of-mass energy
 878 of 2.8 TeV/A with a peak luminosity of $10^{27} \text{ cm}^{-2}\text{s}^{-1}$. Run 1 of LHC, when the center-of-mass
 879 energy only was half of the nominal LHC energy, was enough for both CMS and ATLAS to dis-
 880 cover the Higgs boson [17] and for LHCb to discover pentaquarks [18] and confirm the existance of
 881 tetraquarks [19]. Nevertheless, after the Third Long Shutdown (LS3) (2024-2026), the accelerator
 882 will be in the so called High Luminosity LHC (HL-LHC) configuration [20], increasing its instan-
 883 taneous luminosity to $10^{35} \text{ cm}^{-2}\text{s}^{-1}$ for pp collisions and to $4.5 \times 10^{27} \text{ cm}^{-2}\text{s}^{-1}$, boosting the
 884 discovery potential of the LHC.

885 2.2.1.1 Particle acceleration

886 The LHC is the last of a long series of accelerating devices. Before being accelerated by the LHC,
 887 the particles need to pass through different acceleration stages. All these acceleration stages are

888 visible on Figure 2.3 and pictures of the accelerators are showed in Figure 2.4.

889

890 The story of accelerated protons at CERN starts with a bottle of hydrogen gas injected into the
891 source chamber of the linear particle accelerator *LINAC 2* in which a strong electric field strips the
892 electron off the hygrogen molecules only to keep their nuclei, the protons. The cylindrical conductors,
893 alternatively positively or negatively charged by radiofrequency cavities, accelerate protons by
894 pushing them from behing and pulling them from the front and ultimately give them an energy of
895 50 MeV, increasing their mass by 5% in the process.

896

897 When exiting the LINAC 2, the protons are divided into 4 bunches and injected into the 4 su-
898 perimposed synchrotron rings of the *Booster* where they are then accelerated to reach an energy of
899 1.4 GeV before being injected into the *PS*. Before the Booster was operational in 1972, the protons
900 were directly injected into the PS from the LINAC 2 but the low injection energy limited the amount
901 of protons that could be accelerated at once by the PS. With the Booster, the PS accepts approxi-
902 mately 100 times more particles.

903

904 The 4 proton bunches are thus sent as one to the PS where their energy eventually reaches
905 26 GeV. Since the 70s, the main goal of this 628 m circumference synchrotron has been to sup-
906 ply other machines with accelerated particles. Nowadays, not only the PS accelerates protons, it also
907 accelerates heavy ions from the *Low Energy Ion Ring (LEIR)*. Indeed, the LHC experiments are not
908 only designed to study pp -collisions but also Pb -collisions. Lead is first injected into the dedicated
909 linear collider *LINAC 3*, that accelerate the ions using the same principle than LINAC 2. Electrons
910 are striped off the lead ions all along the acceleration process and eventually, only bare nuclei are
911 injected in the LEIR whose goal is to transform the long ion pulses received into short dense bunches
912 for LHC. Ions injected and stored in the PS were aceelerated by the LEIR from 4.2 MeV to 72 MeV.

913

914 Directly following the PS, is finally the last acceleration stage before the LHC, the 7 km long
915 *SPS*. The SPS accelerates the protons to 450 GeV and inject proton in both LHC accelerator rings
916 that will increase their energy up to 7 TeV. When the LHC runs with heavy lead ions for ALICE
917 and LHCb, ions are injected and accelerated to reach the energy of 2.8 TeV/A.

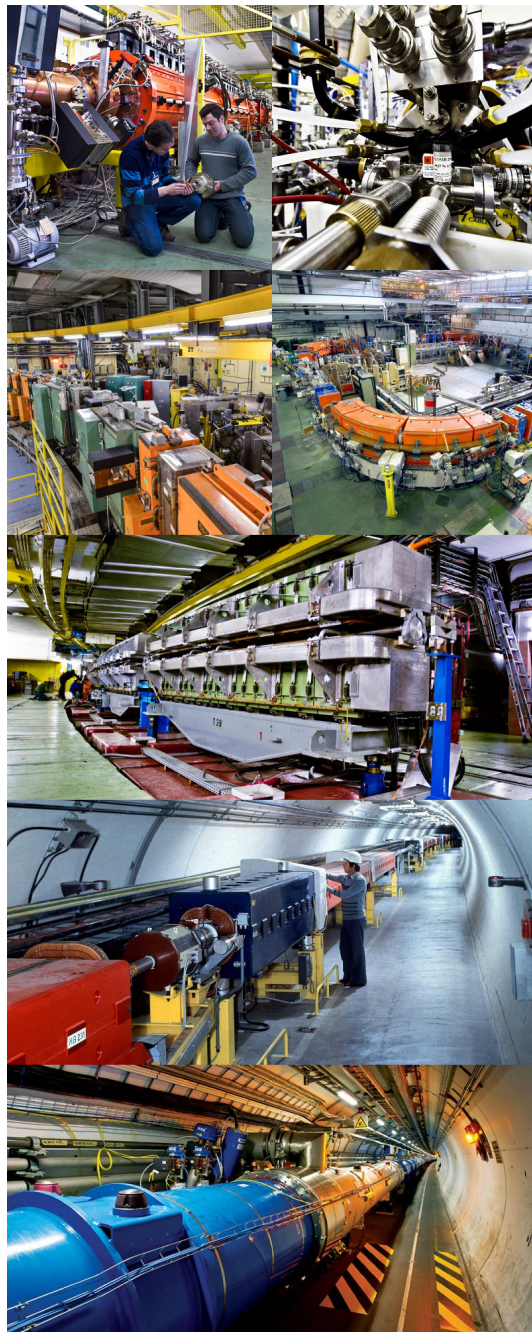


Figure 2.4: Pictures of the different accelerators. From top to bottom: first the LINAC 2 and the Pb source of LINAC 3. Then the Booster and the LEIR. Finally, the PS, the SPS and the LHC.

918 The LHC beams are not continuous and are rather organised in bunches of particles. When in pp -
 919 collision mode, the beams are composed of 2808 bunches of 1.15×10^{11} protons separated by 25 ns.
 920 When in Pb collision mode, the 592 Pb bunches are on the contrary composed of 2.2×10^8 ions
 921 separated by 100 ns. The two parallel proton beams of the LHC are contained in a single twin-

bore magnet due to the space restriction in the LEP tunnel. Indeed, building 2 completely separate accelerator rings next to each other was impossible. The dipoles of the 1232 twin-bore magnets are showed in Figure 2.5 alongside the magnetic field generated along the dipole section to accelerate the particles. The dipoles generate a nominal field of 8.33 T, needed to give protons and lead nucleons their nominal energy. Some 392 quadrupoles, presented in Figure 2.6, are also used to focus the beams, as well as other multipoles to correct smaller imperfections.

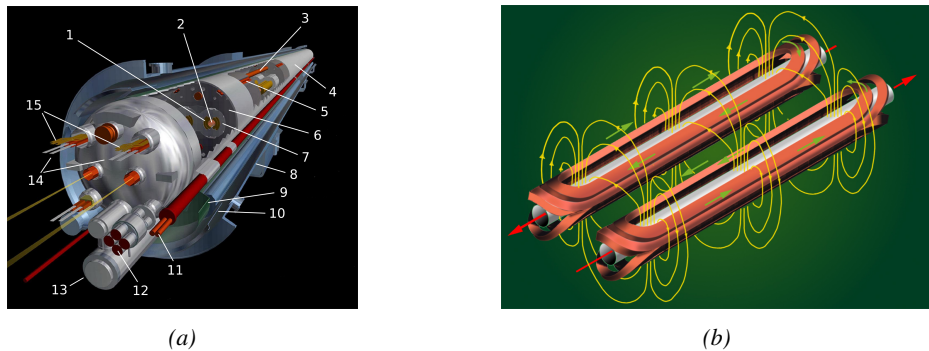


Figure 2.5: Figure 2.5a: schematics of the LHC cryodipoles. 1: Superconducting Coils, 2: Beam pipe, 3: Heat exchanger Pipe, 4: Helium-II Vessel, 5: Superconducting Bus-bar, 6: Iron Yoke, 7: Non-Magnetic Collars, 8: Vacuum Vessel, 9: Radiation Screen, 10: Thermal Shield, 11: Auxiliary Bus-bar Tube, 12: Instrumentation Feed Throughs, 13: Protection Diode, 14: Quadrupole Bus-bars, 15: Spool Piece Bus-bars. Figure 2.5b: magnetic field and resulting motion force applied on the beam particles.

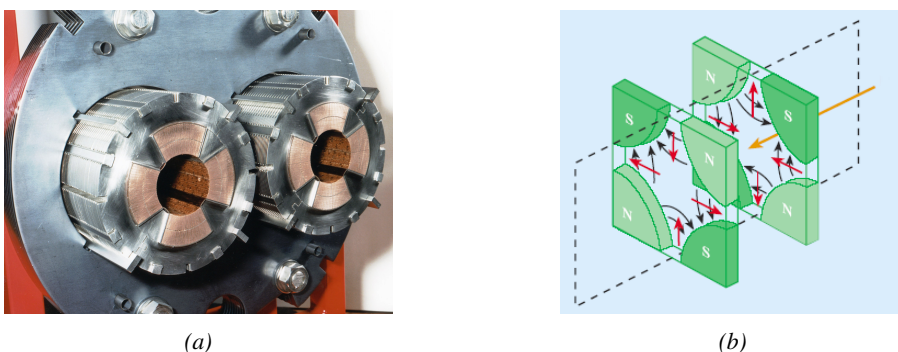


Figure 2.6: Figure 2.6a: picture of the LHC quadrupoles. Figure 2.6b: magnetic fields and resulting focussing force applied on the beam by 2 consecutive quadrupoles.

928 2.2.1.2 LHC discoveries and LHC physics program

929 The very first proton beam successfully circulated in the LHC in September 2008 directly followed
930 by an incident leading to mechanical damage that would delay the LHC program for a year until
931 November 2009.

932 **2.2.1.3 High Luminosity LHC**

933 **2.2.2 CMS, a multipurpose experiment**

934 **2.3 Muon Phase-II Upgrade**

935 After the more than two years lasting First Long Shutdown (LS1), the Large Hadron Collider (LHC)
 936 delivered its very first Run-II proton-proton collisions early 2015. LS1 gave the opportunity to the
 937 LHC and to the its experiments to undergo upgrades. The accelerator is now providing collisions
 938 at center-of-mass energy of 13 TeV and bunch crossing rate of 40 MHz, with a peak luminosity
 939 exceeding its design value. During the first and upcoming second LHC Long Shutdown, the Compact
 940 Muon Solenoid (CMS) detector is also undergoing a number of upgrades to maintain a high system
 941 performance [21].

942 From the LHC Phase-2 or High Luminosity LHC (HL-LHC) period onwards, i.e. past the Third
 943 Long Shutdown (LS3), the performance degradation due to integrated radiation as well as the average
 944 number of inelastic collisions per bunch crossing, or pileup, will rise substantially and become a
 945 major challenge for the LHC experiments, like CMS that are forced to address an upgrade program
 946 for Phase-II [22]. Simulations of the expected distribution of absorbed dose in the CMS detector
 947 under HL-LHC conditions, show in figure 4.16 that detectors placed close to the beamline will have
 948 to withstand high irradiation, the radiation dose being of the order of a few tens of Gy.

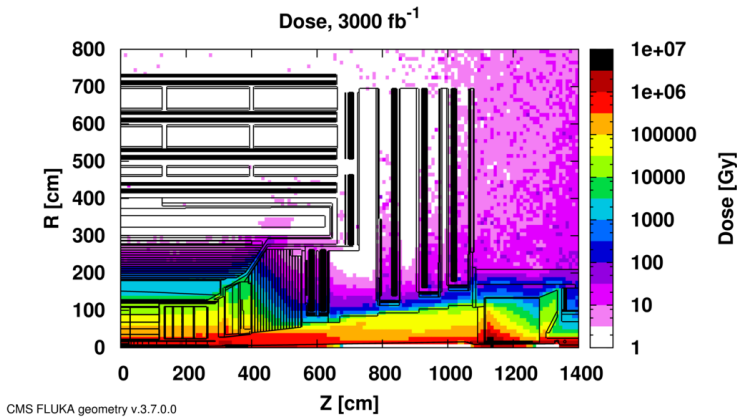


Figure 2.7: Absorbed dose in the CMS cavern after an integrated luminosity of 3000 fb. R is the transverse distance from the beamline and Z is the distance along the beamline from the Interaction Point at Z=0.

949 The measurement of small production cross-section and/or decay branching ratio processes, such
 950 as the Higgs boson coupling to charge leptons or the $B_s \rightarrow \mu^+\mu^-$ decay, is of major interest and
 951 specific upgrades in the forward regions of the detector will be required to maximize the physics
 952 acceptance on the largest possible solid angle. To ensure proper trigger performance within the
 953 present coverage, the muon system will be completed with new chambers. In figure 2.8 one can
 954 see that the existing Cathode Strip Chambers (CSCs) will be completed by Gas Electron Multipliers
 955 (GEMs) and Resistive Plate Chambers (RPCs) in the pseudo-rapidity region $1.6 < |\eta| < 2.4$ to
 956 complete its redundancy as originally scheduled in the CMS Technical Proposal [23].

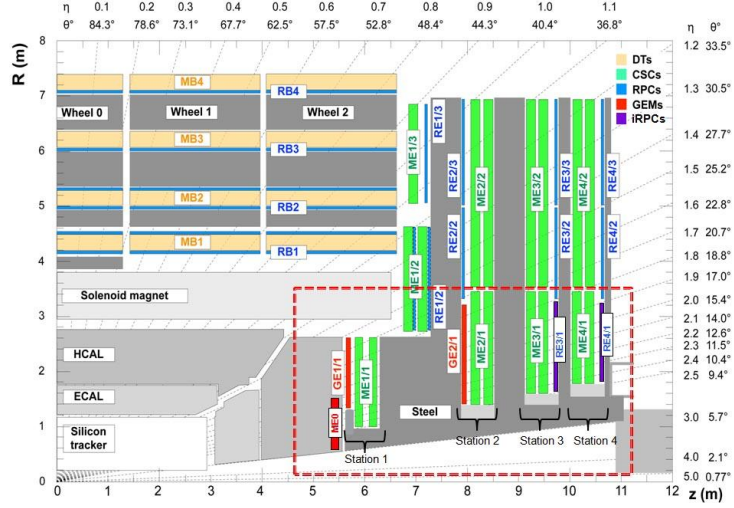


Figure 2.8: A quadrant of the muon system, showing DTs (yellow), RPCs (light blue), and CSCs (green). The locations of new forward muon detectors for Phase-II are contained within the dashed box and indicated in red for GEM stations (ME0, GE1/1, and GE2/1) and dark blue for improved RPC (iRPC) stations (RE3/1 and RE4/1).

957 RPCs are used by the CMS first level trigger for their good timing performances. Indeed, a very
 958 good bunch crossing identification can be obtained with the present CMS RPC system, given their
 959 fast response of the order of 1 ns. In order to contribute to the precision of muon momentum mea-
 960 surements, muon chambers should have a spatial resolution less or comparable to the contribution
 961 of multiple scattering [21]. Most of the plausible physics is covered only considering muons with
 962 $p_T < 100$ GeV thus, in order to match CMS requirements, a spatial resolution of $\mathcal{O}(\text{few mm})$ the
 963 proposed new RPC stations, as shown by the simulation in figure 2.9. According to preliminary
 964 designs, RE3/1 and RE4/1 readout pitch will be comprised between 3 and 6 mm and 5 η -partitions
 965 could be considered.

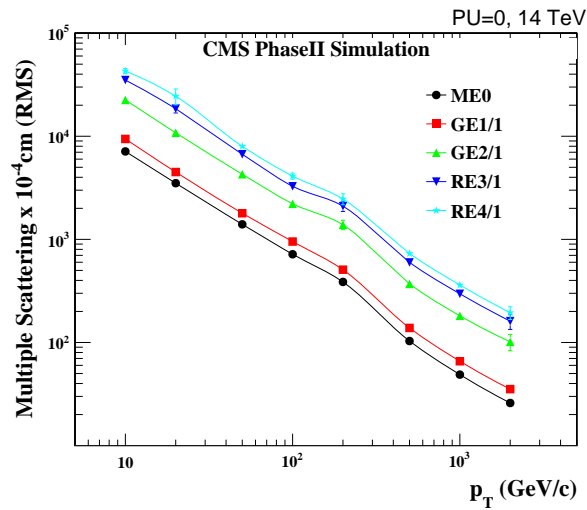


Figure 2.9: RMS of the multiple scattering displacement as a function of muon p_T for the proposed forward muon stations. All of the electromagnetic processes such as bremsstrahlung and magnetic field effect are included in the simulation.

3

966

967

Physics of Resistive plate chambers

968 A Resistive Plate Chamber (RPC) is a gaseous detector using the same physical processes described
969 in Chapter 3. It has been developed in 1981 by Santonico and Cardarelli [24], under the name of
970 *Resistive Plate Counter*, as an alternative to the local-discharge spark counters proposed in 1978
971 by Pestov and Fedotovich [25, 26]. Working with spark chambers implied using high-pressure gas
972 and high mechanical precision which the RPC simplified by formerly using a gas mixture of argon
973 and butane flowed at atmospheric pressure and a constant and uniform electric field propagated
974 in between two parallel electrode plates. Moreover, a significant increase in rate capability was
975 introduced by the use of electrode plate material with high bulk resistivity, preventing the discharge
976 from growing throughout the whole gas gap. Indeed, the effect of using resistive electrodes is that
977 the constant electric field is locally canceled out by the development of the discharge, limiting its
978 growth.

979 Through its development history, different operating modes [27–29] and new detector designs [30–
980 32] have been discovered, leading to further improvement of the rate capability of such a detector.
981 Moreover, the addition of SF_6 into the gas mix improved the stability of operation of the RPC [33,
982 34].

983 The low developing costs and easily achievable large detection areas offered by RPCs, as well as
984 the wide range of possible designs, made them a natural choice to as muon chambers and/or trigger
985 detectors in multipurpose experiments such as CMS [21] or ATLAS [35], time-of-flight detectors in
986 ALICE [36], calorimeter with CALICE [37] or even detectors for volcanic muography with ToMu-
987 Vol [38].

988 3.1 Principle

989 RPCs are ionisation detectors composed of two parallel resistive plate electrodes in between which
990 a constant electric field is set. The space in between the electrodes, referred as *gap*, is filled with a
991 dense gas that is used to generate primary ionization into the gas volume. The free charge carriers
992 (electrons and cations) created by the ionization of the gas molecules are then accelerated towards

993 the electrodes by the electric field, as shown in Figure 3.1 [39].

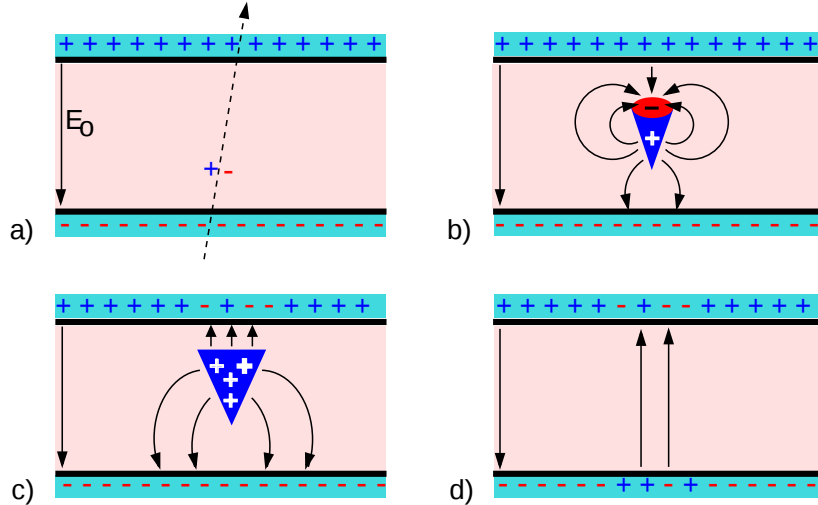


Figure 3.1: Different phases of the avalanche development in the RPC gas volume subjected to a constant electric field E_0 . a) An avalanche is initiated by the primary ionisation caused by the passage of a charged particle through the gas volume. b) Due to its growing size, the avalanche starts to locally influence the electric field. c) The electrons, lighter than the cations reach the anode first. d) The ions reach the cathode. While the charges have not recombined, the electric field in the small region around the avalanche stays affected and locally blind the detector.

994 RPCs being passive detectors, a current on pick-up copper read-out placed outside of the gas
 995 volume is induced by the charge accumulation during the growth of the avalanche. As a result,
 996 the time resolution of the detector is substantially increased as the output signal is generated while
 997 the electrons are still in movement. The advantage of a constant electric field, over multi-wire
 998 proportional chambers, is that the electrons are being fully accelerated from the moment charge
 999 carriers are freed and feel the full strength of the electric field that doesn't depend on the distance to
 1000 the readout and that the output signal doesn't need for the electrons to be physically collected.

1001 The typical gas mixture RPCs are operated with is generally composed of 3 gas compounds.

- 1002 • Tetrafluoroethane ($C_2F_4H_2$), also referred to as *Freon*, is the principal compound of the RPC
 1003 gas mixtures, with a typical fraction above 90%. It is used for it's high effective Townsend
 1004 coefficient and the great average fast charge that allows to operate the detector with a high
 1005 threshold with respect to argon, for example, that has similar effective Townsend coefficient
 1006 but suffers from a lower fast charge. To operate with similar conditions, argon would require a
 1007 higher electric field leading to a higher fraction of streamers, thus limiting the rate capability
 1008 of the detector [40].
- 1009 • Isobutane (i- C_4H_{10}), only present in a few percent in the gas mixtures, is used for its UV
 1010 quenching properties [41] helping to prevent streamers due to UV photon emission during the
 1011 avalanche growth.
- 1012 • Sulfur hexafluoride, (SF_6), referred to simply as *SF6*, is used in very little quantities for its
 1013 high electronegativity. Excess of electrons are being absorbed by the compound and streamers

are suppressed [34]. Nevertheless, a fraction of SF_6 higher than 1% will not bring any extra benefit in terms of streamer cancelation power but will lead to higher operating voltage [33], as can be understood through Figure 3.2.

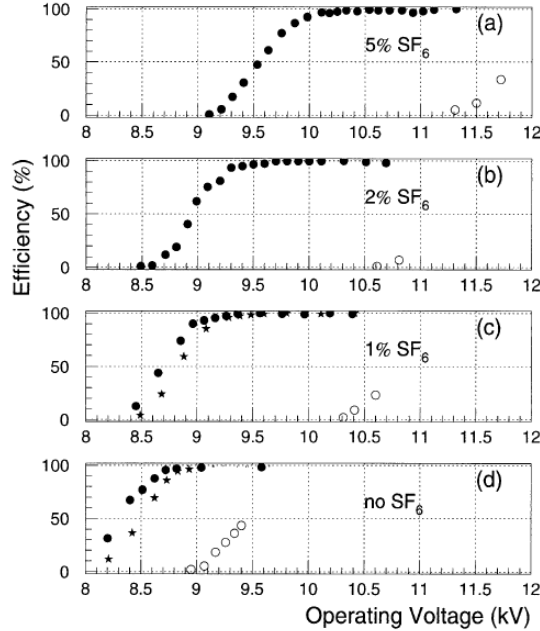


Figure 3.2: Effeciency (circles and stars with 30 mV and 100 mV thresholds respectively) and streamer probability (opened circles) as function of the operating voltatge of a 2 mm single gap HPL RPC flushed with a gas mixture containing (a) 5%, (b) 2%, (c) 1% and (d) no SF_6 [33].

After an avalanche developed in the gas, a time long compared to the development of a discharge is needed to recombine the charge carriers in the electrode material due to their resistivity. This property has the advantage of affecting the local electric field and avoiding sparks in the detector but, on the other hand, the rate capability is intrinsically limited by the time constant τ_{RPC} of the detector. Using a quasi-static approximation of Maxwell's equations for weakly conducting media, it can be shown that the time constant τ_{RPC} necessary to the charge recombination at the interface in between the electrode and the gas volume is given by the Formula 3.1 [42].

$$\tau_{RPC} = \frac{\epsilon_{electrode} + \epsilon_{gas}}{\sigma_{electrode} + \sigma_{gas}} \quad (3.1)$$

A gas can be assimilated to vacuum, leading to $\epsilon_{gas} = \epsilon_0$ and $\sigma_{gas} = 0$, and the electrodes permittivity and conductivity can be written as $\epsilon_{electrode} = \epsilon_r \epsilon_0$ and $\sigma_{electrode} = 1/\rho_{electrode}$, showing the strong dependence of the time constant to the electrodes resistivity in Formula 3.2.

$$\tau_{RPC} = (\epsilon_r + 1)\epsilon_0 \times \rho_{electrode} \quad (3.2)$$

Very few materials with a low enough resistivity exist in nature. The resistivity targeted to build RPCs ranges from 10^9 to $10^{12} \Omega \cdot \text{cm}$. The most common RPC electrode materials are displayed in Table 3.1. When the doped glass and ceramics can offer short time constants of the order of 1 ms,

1030 the developing cost of such materials is quite high due to the very low demand. Thus, High-pressure
 1031 laminate (HPL) is often the choice for high rate experiments using very large RPC detection areas.
 1032 Other experiments working at cosmic muon fluxes can safely operate with ordinary float glass.

Material	$\rho_{electrode}$ ($\Omega \cdot \text{cm}$)	ϵ_r	τ_{RPC} (ms)
Float glass	10^{12}	~ 7	~ 700
High-pressure laminate	10^{10} to 10^{12}	~ 6	~ 6 to 600
Doped glass (LR S)	10^9 to 10^{11}	~ 10	~ 1 to 100
Doped ceramics (SiN/SiC)	10^9	~ 8.5	~ 1
Doped ceramics (Ferrite)	10^8 to 10^{12}	~ 20	~ 0.2 to 2000

Table 3.1: Properties of the most used electrode materials for RPCs.

1033 3.1.1 Electron drift velocity

1034 Talk about the electron drift velocity and mention the time resolution of RPCs.

1035 3.2 Rate capability and time resolution of Resistive Plate Chambers

1037 As already previously discussed, the electrode material plays a key role in the max intrinsic rate
 1038 capability of RPCs. R&D is being done to develop at always cheaper costs material with lower
 1039 resistivity. Nevertheless, the amount of charge released, i.e. the size of the discharge, if reduced
 1040 leads to a smaller blind area in the detector, increasing the rate capability of the detector.

1041 3.2.1 Operation modes

1042 RPCs where developed early 1980s. At that time it was using an operating mode now referred to
 1043 as *streamer mode*. Streamers are large discharges that develop in between the 2 electrodes enough
 1044 to locally discharge the electrodes. If the electric field inside of the gas volume is strong enough,
 1045 with electrons being fast compared to ions, a large and dense cloud of positive ions will develop
 1046 nearby the anode and extend toward the cathode while the electrons are being collected, eventually
 1047 leading to a streamer discharge due to the increase of field seen at the cathode. the field is then strong
 1048 enough so that electrons are pulled out of the cathode. Electrodes, though they are a unique volume
 1049 of resistive material, can be assimilated to capacitors. At the moment an electric field is applied in
 1050 between their outer surfaces, the charge carriers inside of the volume will start moving leading to
 1051 a situation where there is no voltage across the electrodes and a higher density of negative charges,
 1052 i.e. electrons, on the inner surface of the cathode. Finally, when a streamer discharge occurs, these
 1053 electrons are partially released in the gas volume contributing to increase the discharge strength until
 1054 the formation of a conductive plasma, the streamer. This can be understood through Figure 3.3 [27].
 1055 Streamer signals are very convenient in terms of read-out as no amplification is required with output
 1056 pulses amplitudes of the order of a few tens to few hundreds of mV as can be seen on Figure 3.4.

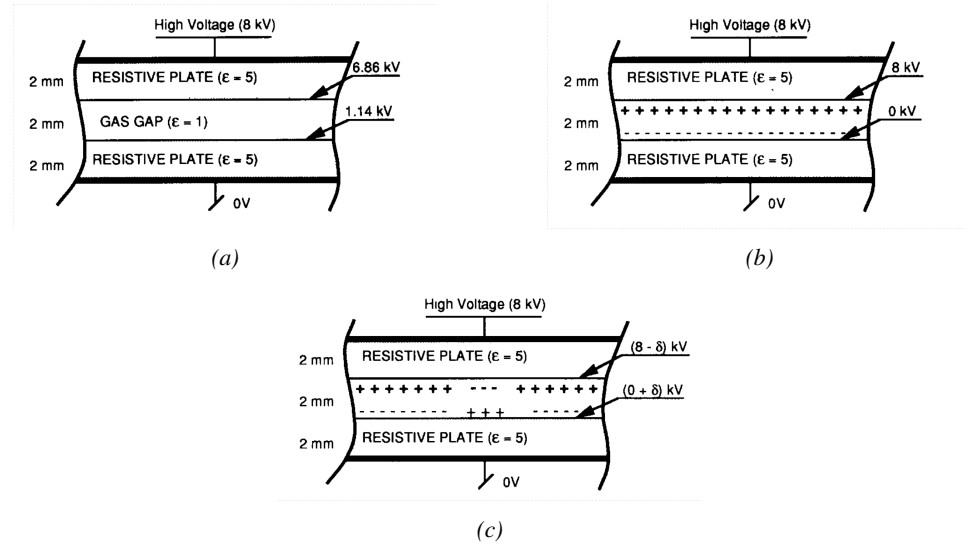


Figure 3.3: Movement of the charge carriers in an RPC. Figure 3.3a: Voltage across an RPC whose electrode have a relative permittivity of 5 at the moment the tension is applied. Figure 3.3b: After the charge carriers moved, the electrodes are charged and there is no voltage drop over the electrodes anymore. The full potential is applied on the gas gap only. Figure 3.3c: The streamer discharge initiated by a charged particle transports electrons and cations towards the anode and cathode respectively.

When the electric field is reduced though, the electronic gain is small until the electrons get close enough to the anode and the positive ion cloud is much smaller. The electric field cannot rise to the point a field emission of electrons on the cathode is possible. The resulting signal is weak, of the order of a few mv as shown on Figure 3.4, and requires amplification. This is the *avalanche mode* of RPC operation.

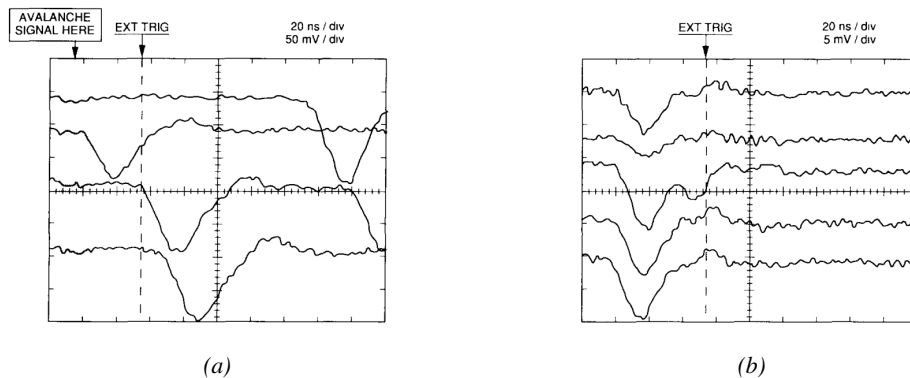


Figure 3.4: Typical oscilloscope pulses in streamer mode (Figure 3.4a) and avalanche mode (Figure 3.4b). In the case of streamer mode, the very small avalanche signal is visible.

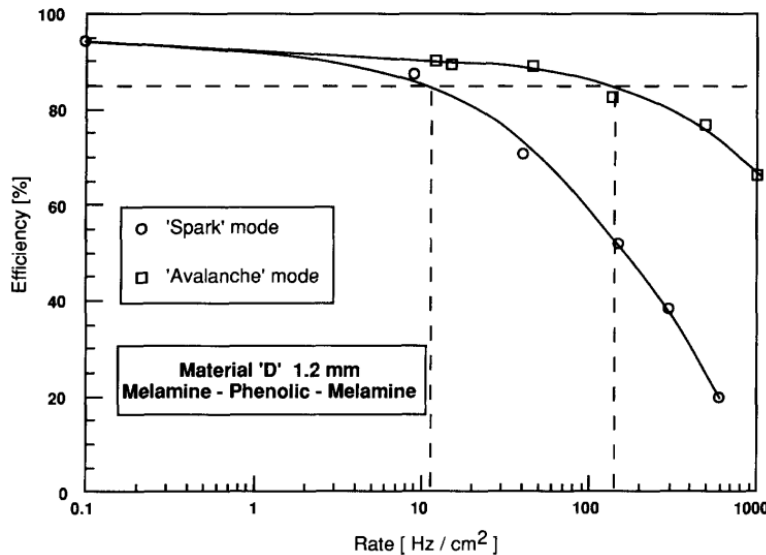


Figure 3.5: Rate capability comparison for the streamer and avalanche mode of operation. An order of magnitude in rate capability for a maximal efficiency drop of 10% is gained by using the avalanche mode over the streamer mode.

This mode offers a higher rate capability by providing smaller discharges that don't affect the electrodes charge and are more locally contained in the gas volume as was demonstrated by Crotty with Figure 3.5 [27]. The detector only stays locally blind the time the charge carriers are recombined and there is no need for electrode recharge which is a long process affecting a large portion of the detector. Another advantage of avalanche signals over streamer is the great time consistency. Figure 3.4 shows very clearly that avalanche signals have a very small time jitter. This is a natural choice for high rate experiments.

3.2.2 Detector designs and performance

Different RPC design have been used and each of them present its own advantages. Historically, the first type of RPC to have been developed is what is referred now to *narrow gap* RPC [24, 43]. After the avalanche mode has been discovered [27], it has been proven that increasing the width of the gas gap lead to higher rate capability, due to lower charge deposition per avalanche, and lower power dissipation [43]. Nevertheless, by increasing the gas gap width, the time resolution of the detector decreases. This is a natural result if the increase of active gas volume in the detector is taken into account. Indeed, for a given threshold, only the small fraction of gas closest to the cathode will provide enough gain to have a detectable signal. In the case of a wider gas volume, the active region is then larger and a larger time jitter is introduced with the variation of starting position of the avalanche, as discussed in [30]. To solve improve both the time resolution and the rate capability, different methods were used trying to get advantages of both narrow and wide gap RPCs.

3.2.2.1 Double-gap RPC

Double-gap RPCs are made out of 2 narrow RPC detectors. The 2 RPC gaps are stacked on top of each other as shown in Figure 3.6. This detector layout, popularized by the two multipurpose experiments CMS [21] and ATLAS [35] at LHC, can be used as an OR system in which each individual chamber participates in the output signal. The gain of such a detector is greatly reduced with respect to single-gap RPCs with an efficiency plateau reached at lower voltage, as visible on Figure 3.7.

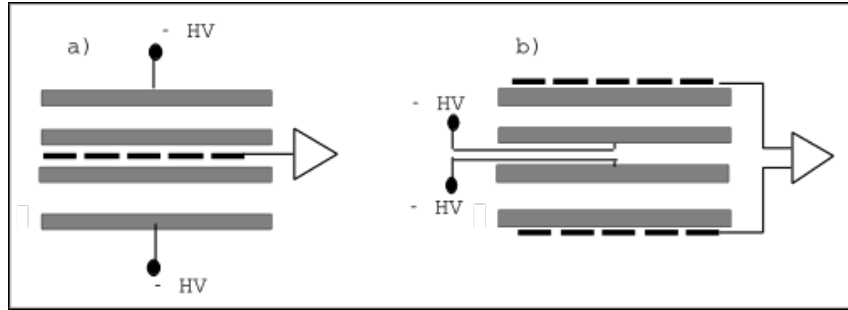


Figure 3.6: Possible double-gap RPC layouts: a) "standard" 1D double-gap RPC, as used in CMS experiment, where the anodes are facing each other and a 1D read-out plane is sandwiched in between them, b) double read-out double-gap RPC as used in ATLAS experiment, where the cathodes are facing each other and 2 read-out planes are used on the outer surfaces. This last layout can offer the possibility to use a 2D reconstruction by using orthogonal read-out planes.

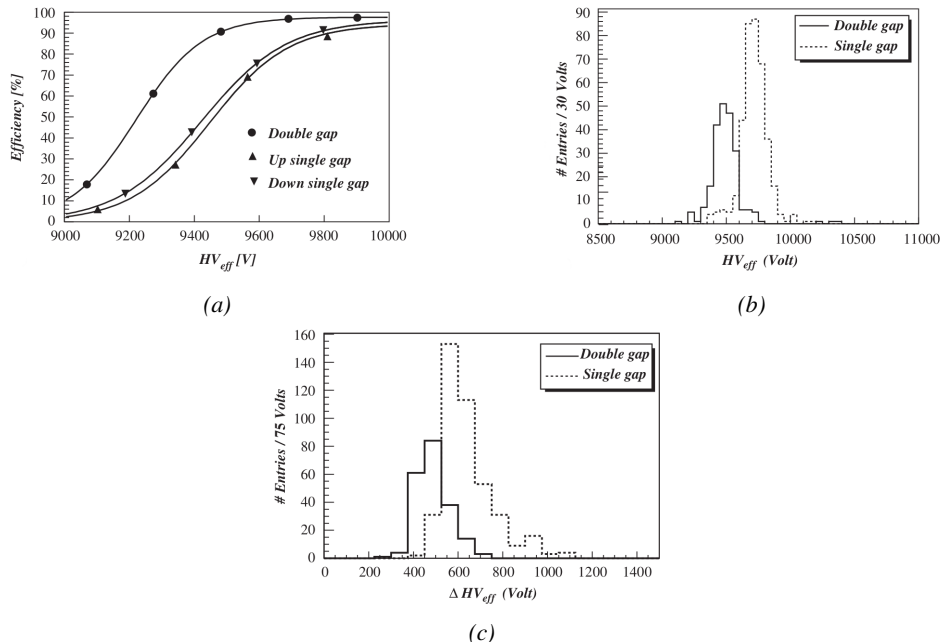


Figure 3.7: Comparison of performance of CMS double and single gap RPCs using cosmic muons [44]. Figure 3.7a: Comparison of efficiency sigmoids. Figure 3.7b: Voltage distribution at 95% of maximum efficiency. Figure 3.7c: $\Delta_{10\%}^{90\%}$ distribution.

3.2.2.2 Multigap RPC (MRPC)

MRPCs are layouts in which floating sub electrode plates are placed into a wide gap RPC to divide the gas volume and create a sum of narrow gaps [30, 31]. The time resolution of such a detector can reach of few tens of ps, with gas gaps of the order of a few hundred μm as shown in Figure 3.8 representing ALICE Time-of-flight (ToF) MRPCs.

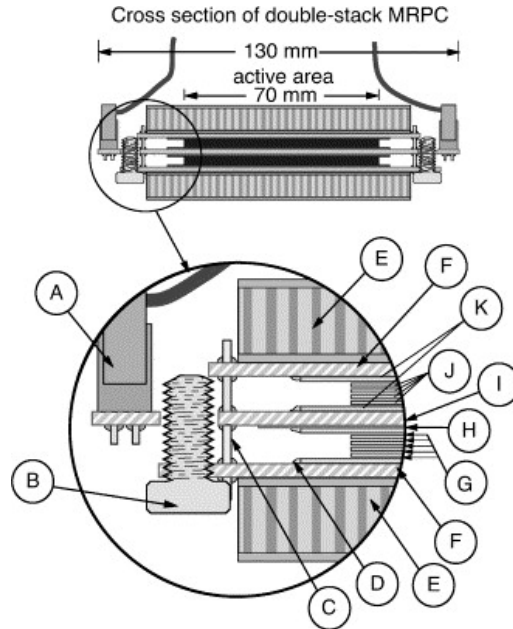


Figure 3.8: Presentation of ALICE MRPC using 250 μm gas gaps, 620 μm outer glass electrodes and 550 μm inner floating electrodes. More details on the labels are given in [45].

Sometimes used as a double multigap RPC, taking advantage of the OR of double gap RPCs, the MRPC is mainly used as ToF detector [45–49] due to its excellent timing properties that allow to perform particle identification as explained by Williams in [50]. The principle of particle identification using ToF is simply the measurement of the velocity of a particle. Indeed, particles are defined by their mass (for the parameter of interest here, their electric charge being measured using the bending angle of the particles traveling through a magnetic field) and this mass can be calculated by measuring the velocity β and momentum of the particle:

$$\beta = \frac{p}{\sqrt{p^2 + m^2}} \quad (3.3)$$

Intuitively, it is trivial to understand that 2 different particles having the same momentum will have a different velocity due to the mass difference and thus a different flight time T_1 and T_2 through the detector and this is used to separate and identify particles. The better the time resolution of the ToF system used, the stronger will the separation be:

$$T = \frac{L}{v} = \frac{L}{c \cdot \beta}, \quad \Delta T = T_1 - T_2 = \frac{L}{c} \left(\sqrt{1 + m_1^2/p^2} - \sqrt{1 + m_2^2/p^2} \right) \cong (m_1^2 - m_2^2) \frac{L}{2cp^2} \quad (3.4)$$

1103 An example of particle identification is given for the case of STAR experiment in Figure 3.9.

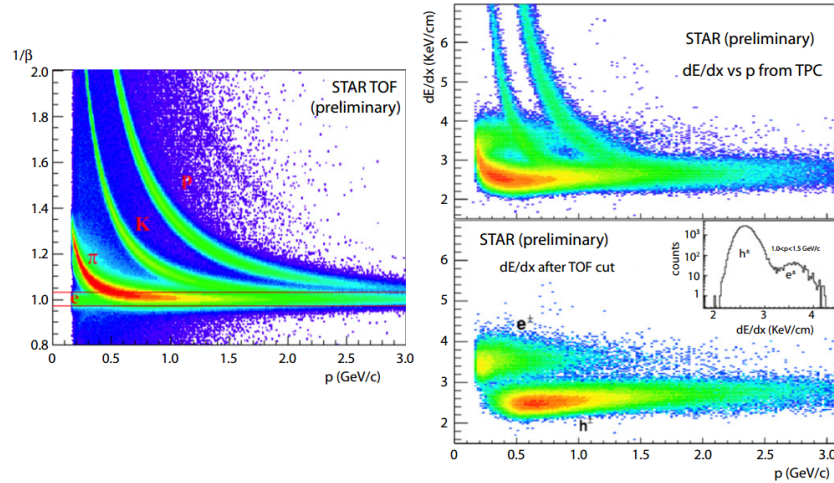


Figure 3.9: Particle identification applied to electrons in the STAR experiment. The identification is performed combining ToF and dE/dx measurements [50].

1104 Another benefice of using such small gas gaps is the strong reduction of the average avalanche
1105 volume and thus of the blind spot on MRPCs leading to an improved rate capability. Multigaps can
1106 sustain backgrounds of several kHz/cm² as demonstrated in Figure 3.10.

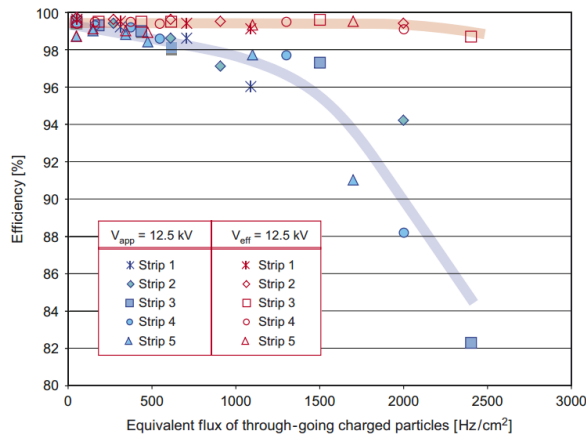


Figure 3.10: Comparison of the detector performance of ALICE ToF MRPC [51] at fixed applied voltage (in blue) and at fixed effective voltage (in red). The effective voltage is kept fixed by increasing the applied voltage accordingly to the current drawn by the detector.

1107 3.2.2.3 Charge distribution and performance limitations

1108 The direct consequence of the different RPC layouts is a variation of intrinsic time resolution of the
1109 RPC as the gap size decreases. An advantage is given to multigaps whose design use sub-millimeter
1110 gas volumes providing very consistent signals.

1111 On the charge spectrum point of view, each layout has its own advantages. When the double-gap
 1112 has the highest induced over drifting charge ratio, as seen in Figure 3.11, the multigap has a charge
 1113 spectrum strongly detached from the origin, as visible in Figure 3.12. A high induced over drifting
 1114 charge ratio means that the double gap can be safely operated at high threshold or that at similar
 1115 threshold it can be operated with a twice smaller drifting charge, meaning a higher rate capability.
 1116 On the other hand, the strong detachment of the charge spectrum from the origin in the MRPC case
 1117 allows to reach a higher efficiency with increasing threshold as most of the induced charge is not low
 1118 due to the convolution of several single gap spectra. The range of stable efficiency increases with
 1119 the number of gap, as presented in Figure 3.13.

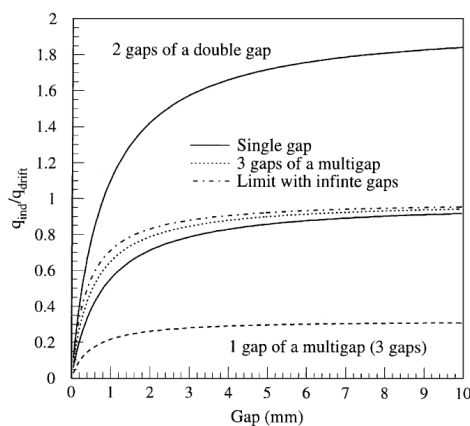


Figure 3.11: Ratio between total induced and drifting charge have been simulated for single gap, double-gap and multigap layouts [52]. The total induced charge for a double-gap RPC is a factor 2 higher than for a multigap.

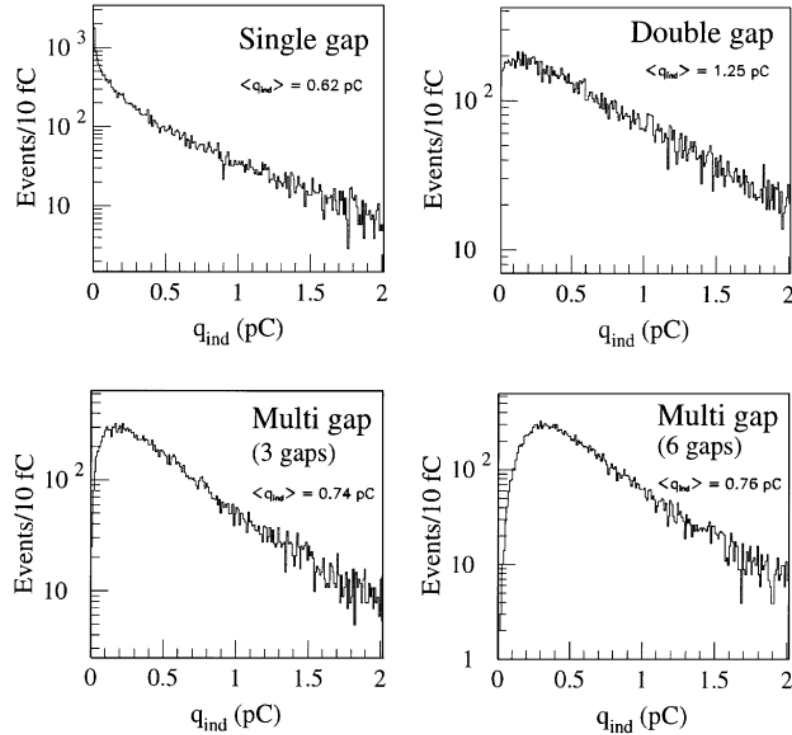


Figure 3.12: Charge spectra have been simulated for single gap, double-gap and multigap layouts [52]. It appears that when single gap shows a decreasing spectrum, double and multigap layouts exhibit a spectrum whose peak is detached from the origin. The detachment gets stronger as the number of gaps increases.

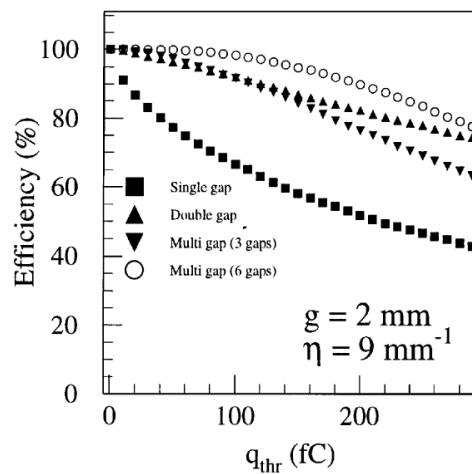


Figure 3.13: The maximal theoretical efficiency is simulated for single gap, double-gap and multigap layouts [52] at a constant gap thickness of 2 mm and using an effective Townsend coefficient of 9 mm^{-1} .

¹¹²⁰ **3.3 Signal formation**

¹¹²¹ **3.4 Gas transport parameters**

4

1122

1123

1124

Longevity studies and Consolidation of the present CMS RPC subsystem

1125

4.1 Resistive Plate Chambers at CMS

1126

4.1.1 Overview

1127

The Resistive Plate Chambers (RPC) system, located in both barrel and endcap regions, provides a fast, independent muon trigger with a looser p_T threshold over a large portion of the pseudorapidity range ($|\eta| < 1.6$) [add reconstruction].

1130

During High-Luminosity LHC (HL-LHC) operations the expected conditions in terms of background and pile-up will make the identification and correct P_T assignment a challenge for the Muon system. The goal of RPC upgrade is to provide additional hits to the Muon system with precise timing. All these informations will be elaborated by the trigger system in a global way enhancing the performance of the trigger in terms of efficiency and rate control. The RPC Upgrade is based on two projects: an improved Link Board System and the extension of the RPC coverage up to $|\eta| = 2.4$. [FIXME 2.4 or 2.5?]

1138

The Link Board system, that will be described in section xxx, is responsible to process, synchronize and zero-suppress the signals coming from the RPC front end boards. The Link Board components have been produced between 2006 and 2007 and will be subjected to aging and failure in the long term. The upgraded Link Board system will overcome the aging problems described in section xxx and will allow for a more precise timing information to the RPC hits from 25 to 1 ns [ref section xxx].

1144

The extension of the RPC system up to $|\eta| = 2.1$ was already planned in the CMS TDR [ref cmstdr] and staged because of budget limitations and expected background rates higher than the rate capability of the present CMS RPCs in that region. An extensive R&D program has been done in order to develop an improved RPC that fulfills the CMS requirements. Two new RPC layers in the innermost ring of stations 3 and 4 will be added with benefits to the neutron-induced background

1145

1146

1147

1148

1149 reduction and efficiency improvement for both trigger and offline reconstruction.

1150 4.1.2 The present RPC system

1151 The RPC system is organized in 4 stations called RB1 to RB4 in the barrel region, and RE1 to RE4
 1152 in the endcap region. The innermost barrel stations, RB1 and RB2, are instrumented with 2 layers
 1153 of RPCs facing the innermost (RB1in and RB2in) and outermost (RB1out and RB2out) sides of the
 1154 DT chambers. Every chamber is then divided from the read-out point of view into 2 or 3 η partitions
 1155 called “rolls”. The RPC system consist of 480 barrel chambers and 576 endcap chambers. Details
 1156 on the geometry are discussed in the paper [ref to geo paper].

1157 The CMS RPC chamber is a double-gap, operated in avalanche mode to ensure reliable operation
 1158 at high rates. Each RPC gap consists of two 2-mm-thick resistive High-Pressure Laminate (HPL)
 1159 plates separated by a 2-mm-thick gas gap. The outer surface of the HPL plates is coated with a thin
 1160 conductive graphite layer, and a voltage is applied. The RPCs are operated with a 3-component,
 1161 non-flammable gas mixture consisting of 95.2% freon ($C_2H_2F_4$, known as R134a), 4.5% isobutane
 1162 ($i-C_4H_{10}$), and 0.3% sulphur hexafluoride (SF_6) with a relative humidity of 40% - 50%. Readout
 1163 strips are aligned in η between the 2 gas gaps. [\[Add a sentence on FEBs.\]](#)

1164 The discriminated signals coming from the Front End boards feed via twisted cables (10 to 20 m
 1165 long) the Link Board System located in UXC on the balconies around the detector. The Link System
 1166 consist of the 1376 Link Boards (LBs) and the 216 Control Boards (CBs), placed in 108 Link Boxes.
 1167 The Link Box is a custom crate (6U high) with 20 slots (for two CBs and eighteen LBs). The Link
 1168 Box contains custom backplane to which the cables from the chambers are connected, as well as the
 1169 cables providing the LBs and CBs power supply and the cables for the RPC FEBs control with use
 1170 of the I2C protocol (trough the CB). The backplane itself contains only connectors (and no any other
 1171 electronic devices).

1172 The Link Board has 96 input channels (one channel corresponds to one RPC strip). The input
 1173 signals are the ~ 100 ns binary pulses which are synchronous to the RPC hits, but not to the LHC
 1174 clock (which drives the entire CMS electronics). Thus the first step of the FEB signals processing
 1175 is synchronization, i.e. assignment of the signals to the BXes (25 ns periods). Then the data are
 1176 compressed with a simple zero-suppressing algorithm (the input channels are grouped into 8 bit
 1177 partitions, only the partitions with at least one nonzero bit are selected for each BX). Next, the non-
 1178 empty partitions are time-multiplexed i.e. if there are more than one such partition in a given BX,
 1179 they are sent one-by-one in consecutive BXes. The data from 3 neighbouring LBs are concentrated
 1180 by the middle LB which contains the optical transmitter for sending them to the USC over a fiber at
 1181 1.6 Gbps.

1182 The Control Boards provide the communication of the control software with the LBs via the
 1183 FEC/CCU system. The CBs are connected into token rings, each ring consists of 12 CBs of one
 1184 detector tower and a FEC mezzanine board placed on the CCS board located in the VME crate in
 1185 the USC. In total, there are 18 rings in the entire Link System. The CBs also perform automatic
 1186 reloading of the LB's firmware which is needed in order to avoid accumulation of the radiation
 1187 induced SEUs in the LBs firmware.

1188 Both LBs and CB are based on the Xilinx Spartan III FPGAs, the CB additionally contains
 1189 radiation-tolerant (FLASH based) FPGA Actel ProAsicPlus.

1190 The High Voltage power system is located in USC, not exposed to radiation and easily accessible
 1191 for any reparation. A single HV channel powers 2 RPC chambers both in the barrel and endcap
 1192 regions. The Low Voltage boards are located in UXC on the balconies and provide the voltage to the

¹¹⁹³ front end electronics.

¹¹⁹⁴ 4.1.3 Pulse processing of CMS RPCs

¹¹⁹⁵ Signals induced by cosmic particle in the RPC strips are shaped by standard CMS RPC Front-End
¹¹⁹⁶ Electronics (FEE) following the scheme of Figure 4.1. On a first stage, analogic signals are amplified
¹¹⁹⁷ and then sent to the Constant Fraction Discriminator (CFD) described in Figure 4.2. At the end of
¹¹⁹⁸ the chain, 100 ns long pulses are sent in the LVDS output. These output signal are sent on one side to
¹¹⁹⁹ a V1190A Time-to-Digital Converter (TDC) module from CAEN and on the other to an OR module
¹²⁰⁰ to count the number of detected signals. Trigger and hit coïncidences are monitored using scalers.
¹²⁰¹ The TDC is used to store the data into ROOT files. These files are thus analysed to understand the
¹²⁰² detectors performance.

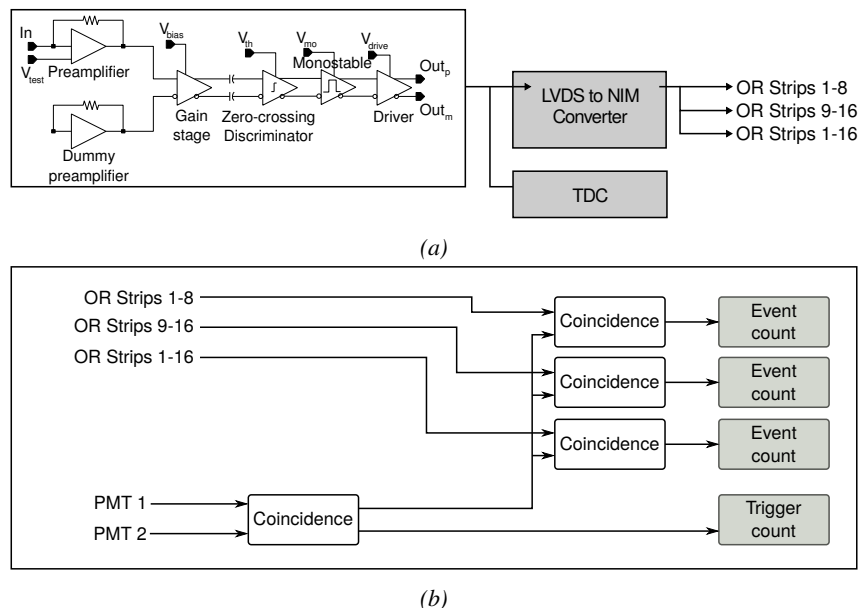


Figure 4.1: Signals from the RPC strips are shaped by the FEE described on Figure 4.1a. Output LVDS signals are then read-out by a TDC module connected to a computer or converted into NIM and sent to scalers. Figure 4.1b describes how these converted signals are put in coincidence with the trigger.

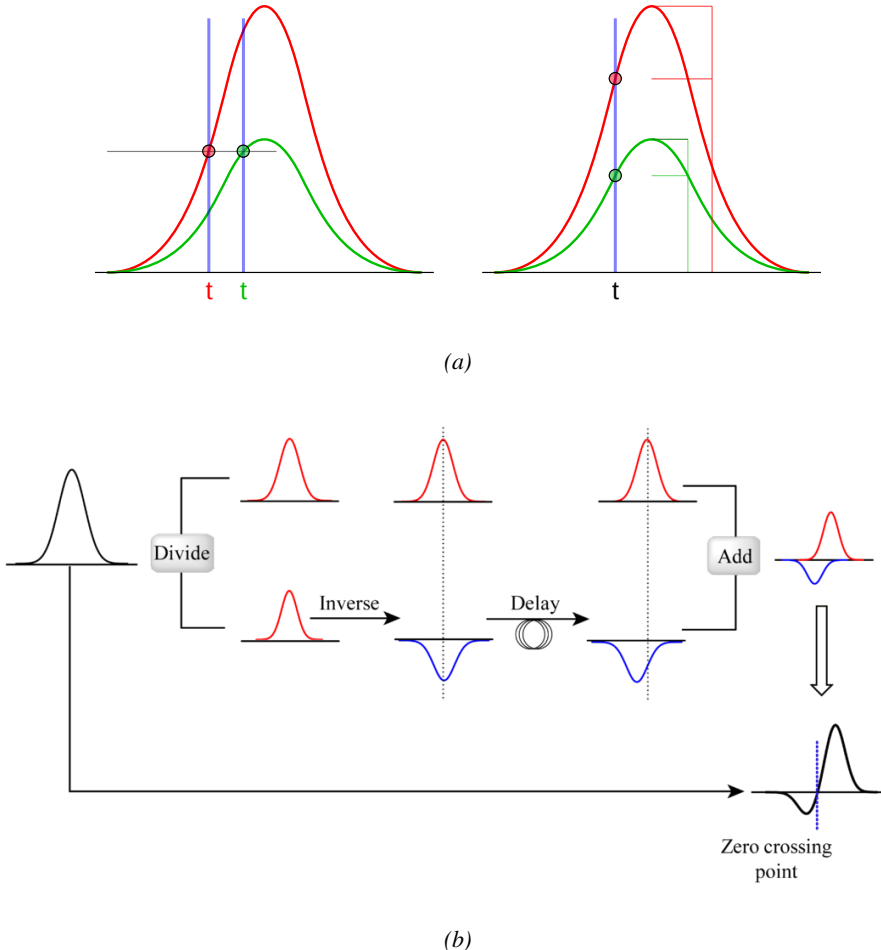


Figure 4.2: Description of the principle of a CFD. A comparison of threshold triggering (left) and constant fraction triggering (right) is shown in Figure 4.2a. Constant fraction triggering is obtained thanks to zero-crossing technique as explained in Figure 4.2b. The signal arriving at the input of the CFD is split into three components. A first one is delayed and connected to the inverting input of a first comparator. A second component is connected to the noninverting input of this first comparator. A third component is connected to the noninverting input of another comparator along with a threshold value connected to the inverting input. Finally, the output of both comparators is fed through an AND gate.

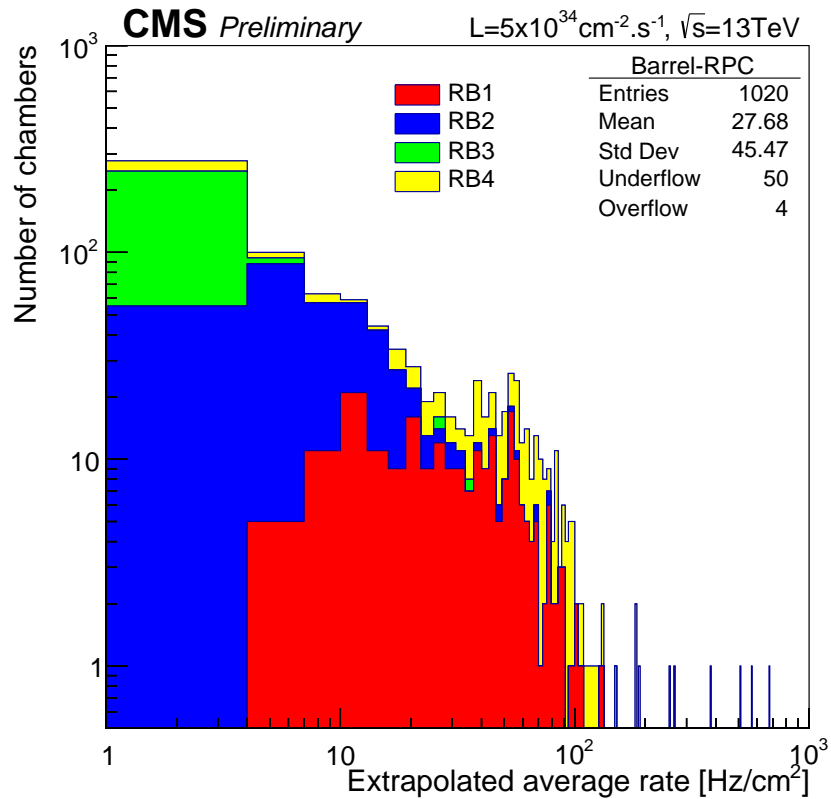
1203 4.2 Testing detectors under extreme conditions

1204 The upgrade from LHC to HL-LHC will increase the peak luminosity from $10^{34} \text{ cm}^{-2} \text{ s}^{-1}$ to reach
 1205 $5 \times 10^{34} \text{ cm}^{-2} \text{ s}^{-1}$, increasing in the same way the total expected background to which the RPC
 1206 system will be subjected to. Composed of low energy gammas and neutrons from $p\text{-}p$ collisions, low
 1207 momentum primary and secondary muons, puch-through hadrons from calorimeters, and particles
 1208 produced in the interaction of the beams with collimators, the background will mostly affect the
 1209 regions of CMS that are the closest to the beam line, i.e. the RPC detectors located in the endcaps.
 1210 [To update.]

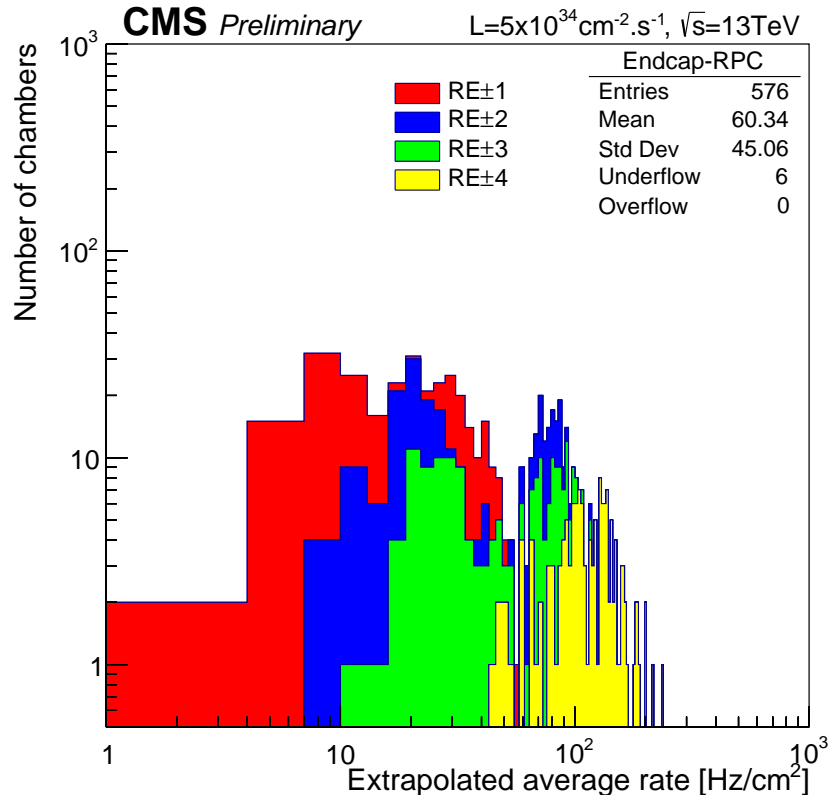
1211

1212 The 2016 data allowed to study the values of the background rate in all RPC system. In Fig-
1213 ure 4.3, the distribution of the chamber background hit rate per unit area is shown at a luminosity
1214 of $5 \times 10^{34} cm^{-2}.s^{-1}$ linearly extrapolating from data collected in 2016 [ref mentioning the linear
1215 dependency of rate vs lumi]. The maximum rate per unit area at HL-LHC conditions is expected to
1216 be of the order of $600 Hz/cm^2$ (including a safety factor 3). Nevertheless, Fluka simulations have
1217 conducted in order to understand the background at HL-LHC conditions. The comparison to the
1218 data has shown, in Figure 4.4, a discrepancy of a factor 2 even though the order of magnitude is
1219 consistent. [Understand mismatch.]

1220



(a)



(b)

Figure 4.3: (4.3a) Extrapolation from 2016 data of single hit rate per unit area in the barrel region. (4.3b) Extrapolation from 2016 data of single hit rate per unit area in the endcap region.

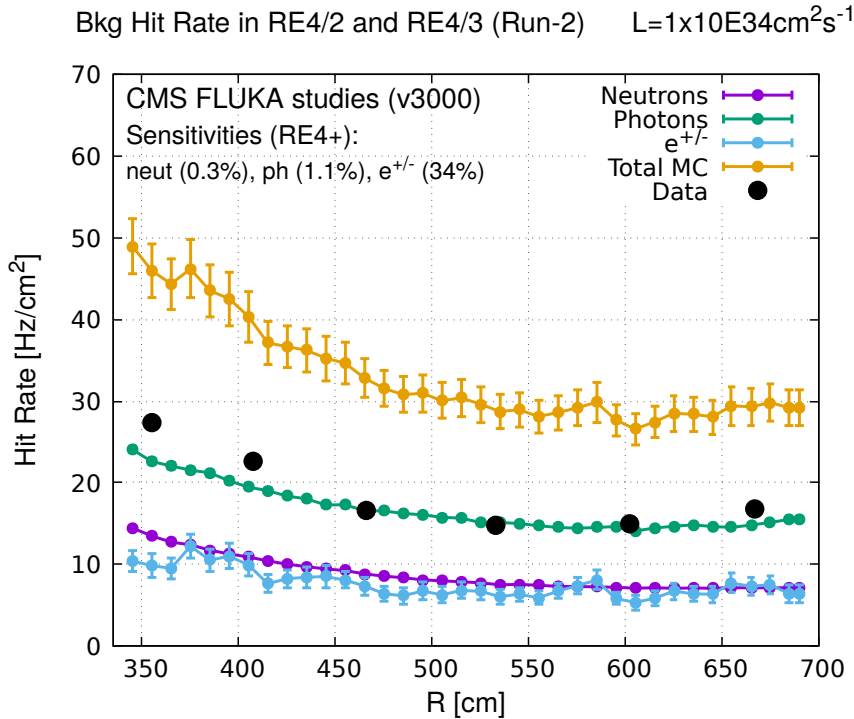


Figure 4.4: Background Fluka simulation compared to 2016 Data at $L = 10^{34} \text{ cm}^{-2} \cdot \text{s}^{-1}$ in the fourth endcap disk region. A mismatch in between simulation and data can be observed. [\[To be understood.\]](#)

In the past, extensive long-term tests were carried out at several gamma and neutron facilities certifying the detector performance. Both full size and small prototype RPCs have been irradiated with photons up to an integrated charge of $\sim 0.05 \text{ C}/\text{cm}^2$ and $\sim 0.4 \text{ C}/\text{cm}^2$, respectively [53, 54]. During Run-I, the RPC system provided stable operation and excellent performance and did not show any aging effects for integrated charge of the order of $0.01 \text{ C}/\text{cm}^2$. Projections on currents from 2016 Data, has allowed to determine that the total integrated charge, by the end of HL-LHC, would be of the order of $1 \text{ C}/\text{cm}^2$ (including a safety factor 3). [\[Corresponding figure needed.\]](#)

1228

1229 4.2.1 The Gamma Irradiation Facilities

1230 4.2.1.1 GIF

1231 Located in the SPS West Area at the downstream end of the X5 test beam, the Gamma Irradiation
 1232 Facility (GIF) was a test area in which particle detectors were exposed to a particle beam in presence
 1233 of an adjustable gamma background [55]. Its goal was to reproduce background conditions these
 1234 detectors would suffer in their operating environment at LHC. GIF layout is shown in Figure 4.5.
 1235 Gamma photons are produced by a strong ^{137}Cs source installed in the upstream part of the zone
 1236 inside a lead container. The source container includes a collimator, designed to irradiate a $6 \times 6 \text{ m}^2$
 1237 area at 5 m maximum to the source. A thin lens-shaped lead filter helps providing with a uniform
 1238 outgoing flux in a vertical plane, orthogonal to the beam direction. The principal collimator hole
 1239 provides a pyramidal aperture of $74^\circ \times 74^\circ$ solid angle and provides a photon flux in a pyramidal vol-

ume along the beam axis. The photon rate is controled by further lead filters allowing the maximum rate to be limited and to vary within a range of four orders of magnitude. Particle detectors under test are then placed within the pyramidal volume in front of the source, perpendicularly to the beam line in order to profit from the homogeneous photon flux. Adjusting the background flux of photons can then be done by using the filters and choosing the position of the detectors with respect to the source.

1245

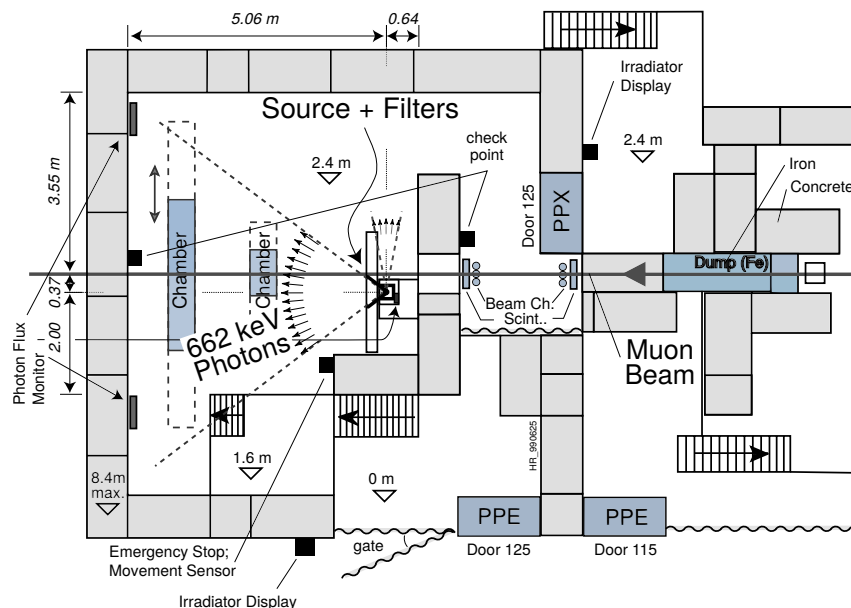


Figure 4.5: Layout of the test beam zone called X5c GIF at CERN. Photons from the radioactive source produce a sustained high rate of random hits over the whole area. The zone is surrounded by 8 m high and 80 cm thick concrete walls. Access is possible through three entry points. Two access doors for personnel and one large gate for material. A crane allows installation of heavy equipment in the area.

As described on Figure 4.6, the ^{137}Cs source emits a 662 keV photon in 85% of the decays. An activity of 740 GBq was measured on the 5th March 1997. To estimate the strength of the flux in 2014, it is necessary to consider the nuclear decay through time assiciated to the Cesium source whose half-life is well known ($t_{1/2} = (30.05 \pm 0.08)$ y). The GIF tests were done in between the 20th and the 31st of August 2014, i.e. at a time $t = (17.47 \pm 0.02)$ y resulting in an attenuation of the activity from 740 GBq in 1997 to 494 GBq in 2014.

1252

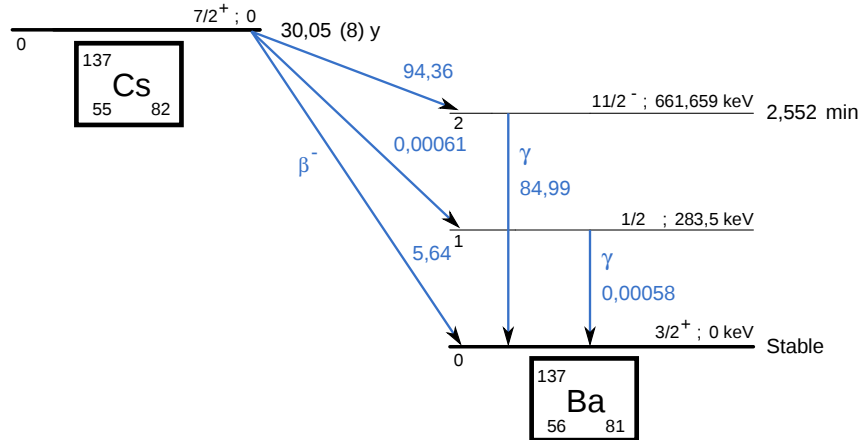


Figure 4.6: ^{137}Cs decays by β^- emission to the ground state of ^{137}Ba ($BR = 5.64\%$) and via the 662 keV isomeric level of ^{137}Ba ($BR = 94.36\%$) whose half-life is 2.55 min.

4.2.1.2 GIF++

The new Gamma Irradiation Facility (GIF++), located in the SPS North Area at the downstream end of the H4 test beam, has replaced its predecessor during LS1 and has been operational since spring 2015 [56]. Like GIF, GIF++ features a ^{137}Cs source of 662 keV gamma photons, their fluence being controlled with a set of filters of various attenuation factors. The source provides two separated large irradiation areas for testing several full-size muon detectors with continuous homogeneous irradiation, as presented in Figure 4.7.

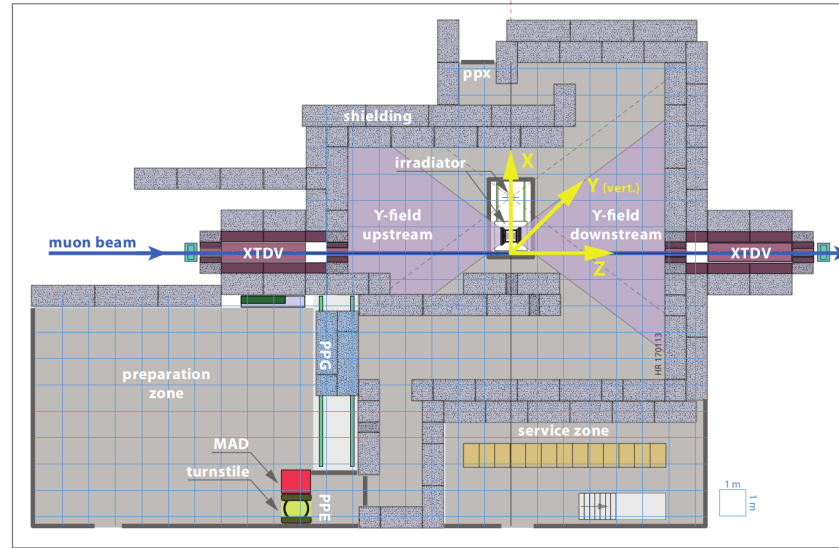


Figure 4.7: Floor plan of the GIF++ facility. When the facility downstream of the GIF++ takes electron beam, a beam pipe is installed along the beam line (z -axis). The irradiator can be displaced laterally (its center moves from $x = 0.65 \text{ m}$ to 2.15 m), to increase the distance to the beam pipe.

1261 The source activity was measured to be about 13.5 TBq in March 2016. The photon flux being
 1262 far greater than HL-LHC expectations, GIF++ provides an excellent facility for accelerated aging
 1263 tests of muon detectors.

1264

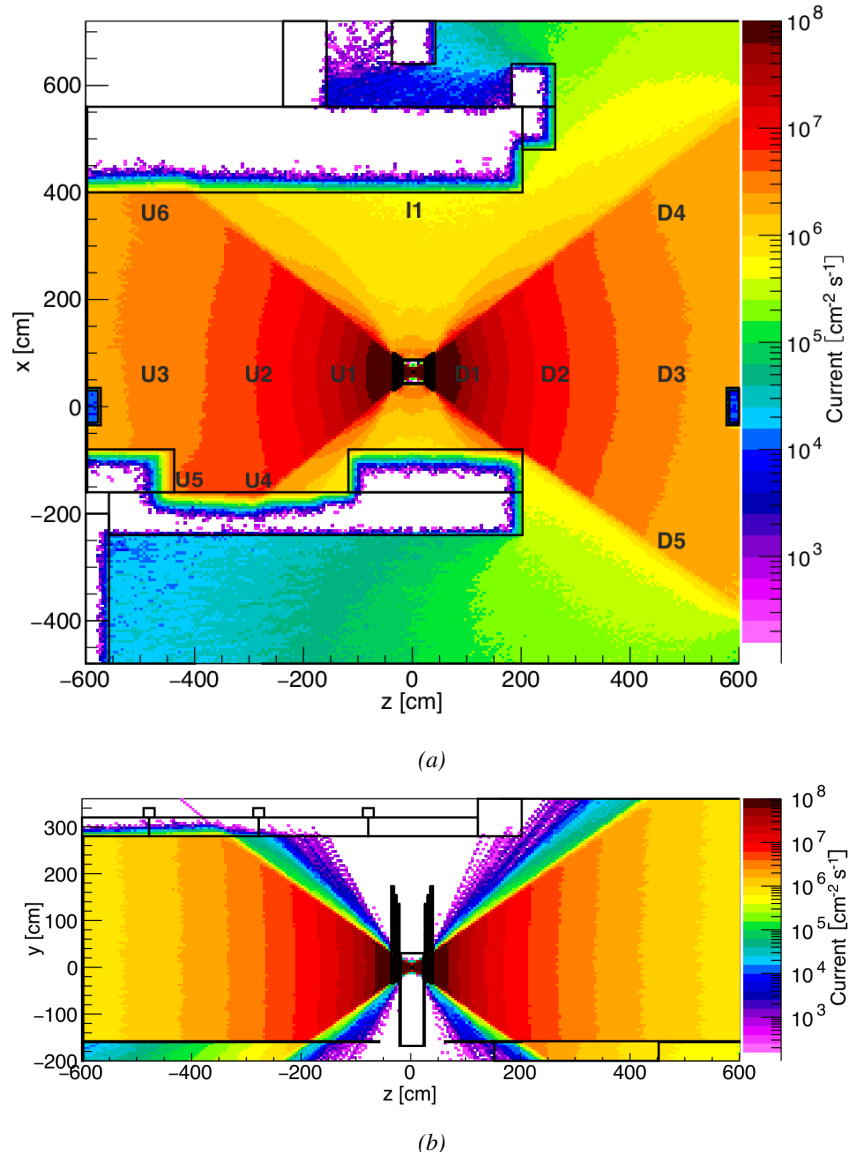


Figure 4.8: Simulated unattenuated current of photons in the xz plane (Figure 4.8a) and yz plane (Figure 4.8b) through the source at $x = 0.65$ m and $y = 0$ m. With angular correction filters, the current of 662 keV photons is made uniform in xy planes.

1265
 1266
 1267

The source is situated in the muon beam line with the muon beam being available a few times a year. The H4 beam, composed of muons with a momentum of about 150 GeV/c, passes through the GIF++ zone and is used to study the performance of the detectors. Its flux is of 104 particles/s/cm²

1268 focused in an area similar to $10 \times 10 \text{ cm}^2$. Therefore, with properly adjusted filters, one can imitate
 1269 the HL-LHC background and study the performance of muon detectors with their trigger/readout
 1270 electronics in HL-LHC environment.

1271

1272 4.3 Preliminary tests at GIF

1273 4.3.1 Resistive Plate Chamber test setup

1274 During summer 2014, preliminary tests have been conducted in the GIF area on a newly produced
 1275 RE4/2 chamber labelled RE-4-2-BARC-161. This chamber has been placed into a trolley covered
 1276 with a tent. The position of the RPC inside the tent and of the tent related to the source is described
 1277 in Figure 4.9. To test this CMS RPC, three different absorber settings were used. First of all,
 1278 measurements were done with fully opened source. Then, to complete this preliminary study, the
 1279 gamma flux has been attenuated from a factor 2 and a factor 5. The expected gamma flux at the level
 1280 of our detector will be discussed in subsection ??.

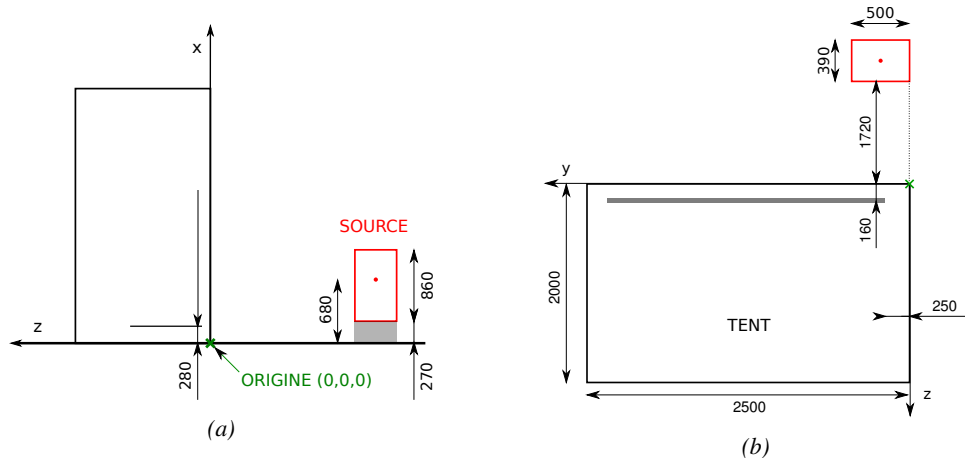


Figure 4.9: Description of the RPC setup. Dimensions are given in mm. A tent containing RPCs is placed at 1720 mm from the source container. The source is situated in the center of the container. RE-4-2-BARC-161 chamber is 160 mm inside the tent. This way, the distance between the source and the chambers plan is 2060 mm. Figure 4.9a provides a side view of the setup in the xz plane while Figure 4.9b shows a top view in the yz plane.



Figure 4.10: RE-4-2-BARC-I61 chamber is inside the tent as described in Figure 4.9. In the top right, the two scintillators used as trigger can be seen. This trigger system has an inclination of 10° relative to horizontal and is placed above half-partition B2 of the RPCs. PMT electronics are shielded thanks to lead blocks placed in order to protect them without stopping photons from going through the scintillators and the chamber.

1281 At the time of the tests, the beam not being operational anymore, a trigger composed of 2 plastic
 1282 scintillators has been placed in front of the setup with an inclination of 10 deg with respect to the
 1283 detector plane in order to look at cosmic muons. Using this particular trigger layout, shown on Fig-
 1284 ure 4.10, leads to a cosmic muon hit distribution into the chamber similar to the one in Figure 4.11.
 1285 Measured without gamma irradiation, two peaks can be seen on the profile of partition B, centered
 1286 on strips 52 and 59. Section ?? will help us understand that these two peaks are due respectively to
 1287 forward and backward coming cosmic particles where forward coming particles are first detected by
 1288 the scintillators and then the RPC while the backward coming muons are first detected in the RPC.

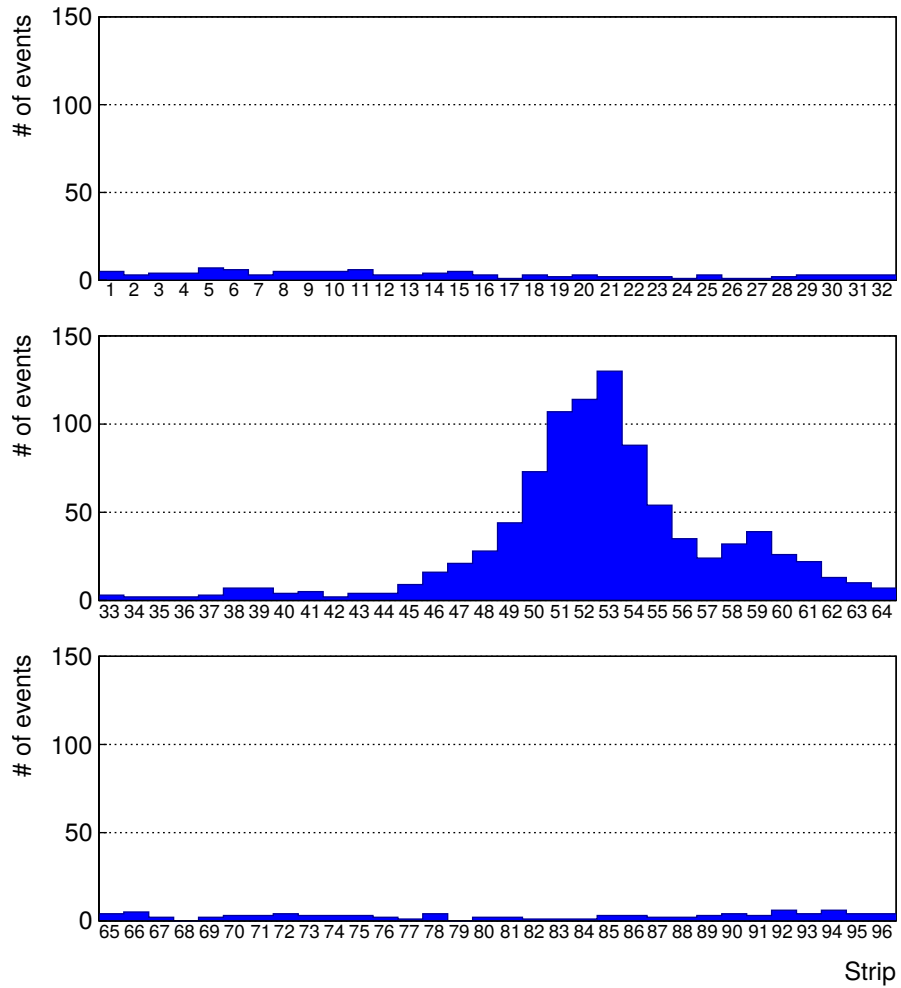


Figure 4.11: Hit distributions over all 3 partitions of RE-4-2-BARC-161 chamber is showed on these plots. Top, middle and bottom figures respectively correspond to partitions A, B, and C. These plots show that some events still occur in other half-partitions than B2, which corresponds to strips 49 to 64, in front of which the trigger is placed, contributing to the inefficiency of detection of cosmic muons. In the case of partitions A and C, the very low amount of data can be interpreted as noise. On the other hand, it is clear that a little portion of muons reach the half-partition B1, corresponding to strips 33 to 48.

1289 4.3.2 Data Acquisition

1290 4.3.3 Geometrical acceptance of the setup layout to cosmic muons

1291 In order to profit from a constant gamma irradiation, the detectors inside of the GIF bunker need
 1292 to be placed in a plane orthogonal to the beam line. The muon beam that used to be available was
 1293 meant to test the performance of detectors under test. This beam not being active anymore, another
 1294 solution to test detector performance had to be used. Thus, it has been decided to use cosmic muons
 1295 detected through a telescope composed of two scintillators. Lead blocks were used as shielding to

1296 protect the photomultipliers from gammas as can be seen from Figure 4.10.

1297 An inclination has been given to the cosmic telescope to maximize the muon flux. A good com-
 1298 promise had to be found between good enough muon flux and narrow enough hit distribution to
 1299 be sure to contain all the events into only one half partitions as required from the limited available
 1300 readout hardware. Nevertheless, a consequence of the misplaced trigger, that can be seen as a loss
 1301 of events in half-partition B1 in Figure 4.11, is an inefficiency. Nevertheless, the inefficiency of ap-
 1302 proximately 20 % highlighted in Figure 4.12 by comparing the performance of chamber BARC-161
 1303 in 904 and at GIF without irradiation seems too important to be explained only by the geometri-
 1304 cal acceptance of the setup itself. Simulations have been conducted to show how the setup brings
 1305 inefficiency.

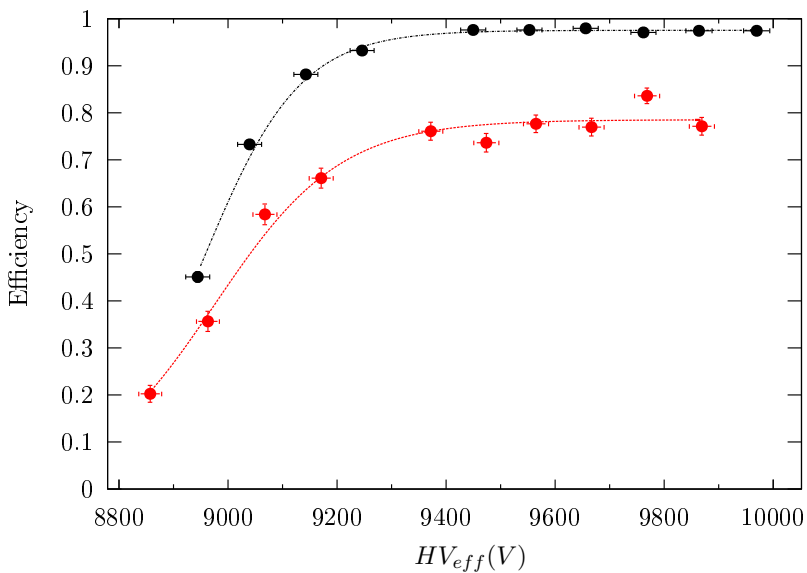


Figure 4.12: Results are derived from data taken on half-partition B2 only. On the 18th of June 2014, data has been taken on chamber RE-2-BARC-161 at building 904 (Prevessin Site) with cosmic muons providing us a reference efficiency plateau of $(97.54 \pm 0.15)\%$ represented by a black curve. A similar measurement has been done at GIF on the 21st of July with the same chamber giving a plateau of $(78.52 \pm 0.94)\%$ represented by a red curve.

1306 4.3.3.1 Description of the simulation layout

1307 The layout of GIF setup has been reproduced and incorporated into a Monte Carlo (MC) simulation
 1308 to study the influence of the disposition of the telescope on the final distribution measured by the
 1309 RPC. A 3D view of the simulated layout is given into Figure 4.13. Muons are generated randomly
 1310 in a horizontal plane located at a height corresponding to the lowest point of the PMTs. This way,
 1311 the needed size of the plane in order to simulate events happening at very big azimuthal angles (i.e.
 1312 $\theta \approx \pi$) can be kept relatively small. The muon flux is designed to follow the usual $\cos^2\theta$ distribution
 1313 for cosmic particle. The goal of the simulation is to look at muons that pass through the muon
 1314 telescope composed of the two scintillators and define their distribution onto the RPC plane. During
 1315 the reconstruction, the RPC plane is then divided into its strips and each muon track is assigned to a
 1316 strip.

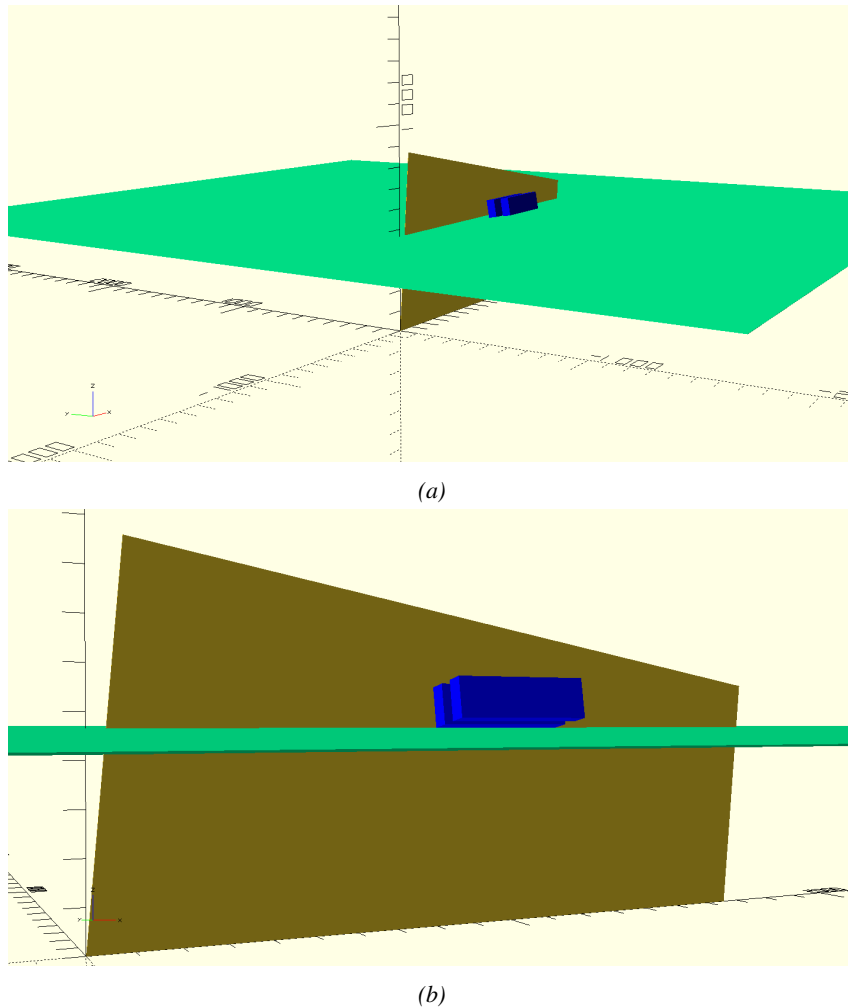


Figure 4.13: Representation of the layout used for the simulations of the test setup. The RPC is represented as a yellow trapezoid while the two scintillators as blue cuboids looking at the sky. A green plane corresponds to the muon generation plane within the simulation. Figure 4.9a shows a global view of the simulated setup. Figure 4.9b shows a zoomed view that allows to see the 2 scintillators as well as the full RPC plane.

1317 In order to further refine the quality of the simulation and understand deeper the results the
 1318 dependance of the distribution has been studied for a range of telescope inclinations. Moreover,
 1319 the threshold applied on the PMT signals has been included into the simulation in the form of a
 1320 cut. In the approximation of uniform scintillators, it has been considered that the threshold can be
 1321 understood as the minimum distance particles need to travel through the scintillating material to give
 1322 a strong enough signal. Particles that travel a distance smaller than the set "threshold" are thus not
 1323 detected by the telescope and cannot trigger the data taking. Finally, the FEE threshold also has
 1324 been considered in a similar way. The mean momentum of horizontal cosmic rays is higher than
 1325 those of vertical ones but the stopping power of matter for momenta ranging from 1 GeV to 1 TeV
 1326 stays comparable. It is then possible to assume that the mean number of primary e^- /ion pairs per
 1327 unit length will stay similar and thus, depending on the applied discriminator threshold, muons with

1328 the shortest path through the gas volume will deposit less charge and induce a smaller signal on the
 1329 pick-up strips that could eventually not be detected. These two thresholds also restrain the overall
 1330 geometrical acceptance of the system.

1331 **4.3.3.2 Simulation procedure**

1332 The simulation software has been designed using C++ and the output data is saved into ROOT
 1333 histograms. Simulations start for a threshold T_{scint} varying in a range from 0 to 45 mm in steps
 1334 of 5 mm, where $T_{scint} = 0$ mm corresponds to the case where there isn't any threshold apply on
 1335 the input signal while $T_{scint} = 45$ mm, which is the scintillator thickness, is the case where muons
 1336 cannot arrive orthogonally onto the scintillator surface. For a given T_{scint} , a set of RPC thresholds
 1337 are considered. The RPC threshold, T_{RPC} varies from 2 mm, the thickness of the gas volume, to
 1338 3 mm in steps of 0.25 mm. For each $(T_{scint}; T_{RPC})$ pair, $N_\mu = 10^8$ muons are randomly generated
 1339 inside the muon plane described in the previous paragraph with an azimuthal angle θ chosen to follow
 1340 a $\cos^2\theta$ distribution.

1341 Planes are associated to each surface of the scintillators. Knowing muon position into the muon
 1342 plane and its direction allows us, by assuming that muons travel in a straight line, to compute the
 1343 intersection of the muon track with these planes. Applying conditions to the limits of the surfaces
 1344 of the scintillator faces then gives us an answer to whether or not the muon passed through the
 1345 scintillators. In the case the muon has indeed passed through the telescope, the path through each
 1346 scintillator is computed and muons whose path was shorter than T_{scint} are rejected and are thus
 1347 considered as having not interacted with the setup.

1348 On the contrary, if the muon is labeled as good, its position within the RPC plane is computed
 1349 and the corresponding strip, determined by geometrical tests in the case the distance through the
 1350 gas volume was enough not to be rejected because of T_{RPC} , gets a hit and several histograms
 1351 are filled in order to keep track of the generation point on the muon plane, the intersection points
 1352 of the reconstructed muons within the telescope, or on the RPC plane, the path traveled through
 1353 each individual scintillator or the gas volume, as well as other histograms. Moreover, muons fill
 1354 different histograms whether they are forward or backward coming muons. They are discriminated
 1355 according to their direction components. When a muon is generated, an (x, y, z) position is assigned
 1356 into the muon plane as well as a $(\theta; \phi)$ pair that gives us the direction it's coming from. This way,
 1357 muons satisfying the condition $0 \leq \phi < \pi$ are designated as backward coming muons while muons
 1358 satisfying $\pi \leq \phi < 2\pi$ as forward coming muons.

1359 This simulation is then repeated for different telescope inclinations ranging in between 4 and 20°
 1360 and varying in steps of 2°. Due to this inclination and to the vertical position of the detector under
 1361 test, the muon distribution reconstructed in the detector plane is asymmetrical. The choice as been
 1362 made to chose a skew distribution formula to fit the data built as the multiplication of gaussian and
 1363 sigmoidal curves together. A typical gaussian formula is given as 4.1 and has three free parameters
 1364 as A_g , its amplitude, \bar{x} , its mean value and σ , its root mean square. Sigmoidal curves as given by
 1365 formula 4.2 are functions converging to 0 and A_s as x diverges. The inflection point is given as x_i
 1366 and λ is proportional to the slope at $x = x_i$. In the limit where $\lambda \rightarrow \infty$, the sigmoid becomes a
 1367 step function.

$$g(x) = A_g e^{-\frac{(x-\bar{x})^2}{2\sigma^2}} \quad (4.1)$$

$$s(x) = \frac{A_s}{1 + e^{-\lambda(x-x_i)}} \quad (4.2)$$

Finally, a possible representation of a skew distribution is given by formula 4.3 and is the product of 4.1 and 4.2. Naturally, here $A_{sk} = A_g \times A_s$ and represents the theoretical maximum in the limit where the skew tends to a gaussian function.

$$sk(x) = g(x) \times s(x) = A_{sk} \frac{e^{\frac{-(x-\bar{x})^2}{2\sigma^2}}}{1 + e^{-\lambda(x-x_i)}} \quad (4.3)$$

4.3.3.3 Results

Influence of T_{scint} on the muon distribution

Influence of T_{RPC} on the muon distribution

Influence of the telescope inclination on the muon distribution

Comparison to data taken at GIF without irradiation

4.3.4 Photon flux at GIF

4.3.4.1 Expectations from simulations

In order to understand and evaluate the γ flux in the GIF area, simulations had been conducted in 1999 and published by S. Agosteo et al [55]. Table 4.1 presented in this article gives us the γ flux for different distances D to the source. This simulation was done using GEANT and a Monte Carlo N-Particle (MCNP) transport code, and the flux F is given in number of γ per unit area and unit time along with the estimated error from these packages expressed in %.

Nominal ABS	Photon flux F [$s^{-1}cm^{-2}$]			
	at $D = 50$ cm	at $D = 155$ cm	at $D = 300$ cm	at $D = 400$ cm
1	$0.12 \cdot 10^8 \pm 0.2\%$	$0.14 \cdot 10^7 \pm 0.5\%$	$0.45 \cdot 10^6 \pm 0.5\%$	$0.28 \cdot 10^6 \pm 0.5\%$
2	$0.68 \cdot 10^7 \pm 0.3\%$	$0.80 \cdot 10^6 \pm 0.8\%$	$0.25 \cdot 10^6 \pm 0.8\%$	$0.16 \cdot 10^6 \pm 0.6\%$
5	$0.31 \cdot 10^7 \pm 0.4\%$	$0.36 \cdot 10^6 \pm 1.2\%$	$0.11 \cdot 10^6 \pm 1.2\%$	$0.70 \cdot 10^5 \pm 0.9\%$

Table 4.1: Total photon flux ($E\gamma \leq 662$ keV) with statistical error predicted considering a ^{137}Cs activity of 740 GBq at different values of the distance D to the source along the x -axis of irradiation field [55].

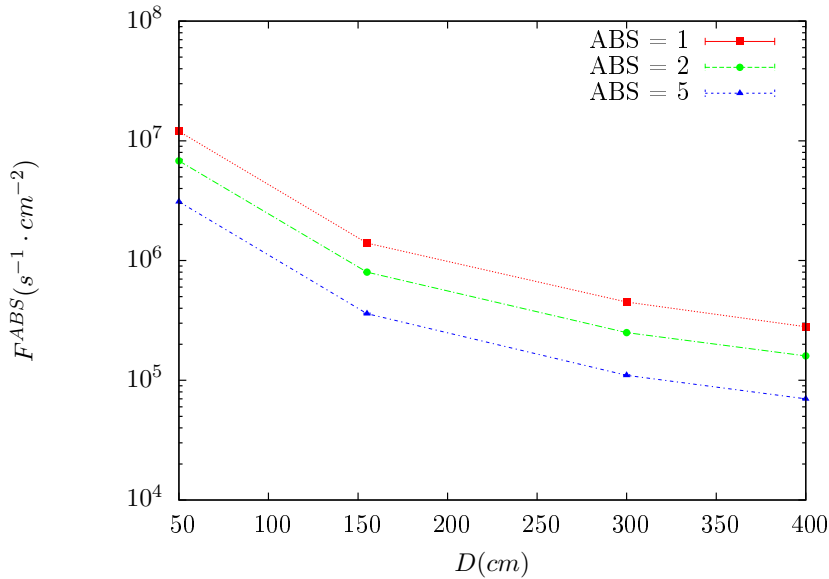


Figure 4.14: γ flux $F(D)$ is plot using values from table 4.1. As expected, the plot shows similar attenuation behaviours with increasing distance for each absorption factors.

The simulation doesn't directly provide us with an estimated flux at the level of our RPC. First of all, it is needed to extract the value of the flux from the available data contained in the original paper and then to estimate the flux in 2014 at the time the experimentation took place. Figure 4.14 that contains the data from Table 4.1. In the case of a pointlike source emitting isotropic and homogeneous gamma radiations, the gamma flux F at a distance D to the source with respect to a reference point situated at D_0 where a known flux F_0 is measured will be expressed like in Equation 4.4, assuming that the flux decreases as $1/D^2$, where c is a fitting factor.

$$F^{ABS} = F_0^{ABS} \times \left(\frac{cD_0}{D} \right)^2 \quad (4.4)$$

By rewriting Equation 4.4, it comes that :

$$c = \frac{D}{D_0} \sqrt{\frac{F^{ABS}}{F_0^{ABS}}} \quad (4.5)$$

$$\Delta c = \frac{c}{2} \left(\frac{\Delta F^{ABS}}{F^{ABS}} + \frac{\Delta F_0^{ABS}}{F_0^{ABS}} \right) \quad (4.6)$$

Finally, using Equation 4.5 and the data in Table 4.1 with $D_0 = 50$ cm as reference point, we can build Table 4.2. It is interesting to note that c for each value of D doesn't depend on the absorption factor.

Nominal ABS	Correction factor c		
	at $D = 155$ cm	at $D = 300$ cm	at $D = 400$ cm
1	$1.059 \pm 0.70\%$	$1.162 \pm 0.70\%$	$1.222 \pm 0.70\%$
2	$1.063 \pm 1.10\%$	$1.150 \pm 1.10\%$	$1.227 \pm 0.90\%$
5	$1.056 \pm 1.60\%$	$1.130 \pm 1.60\%$	$1.202 \pm 1.30\%$

Table 4.2: Correction factor c is computed thanks to formulae 4.5 taking as reference $D_0 = 50$ cm and the associated flux F_0^{ABS} for each absorption factor available in table 4.1.

1394 For the range of D/D_0 values available, it is possible to use a simple linear fit to get the evolution
 1395 of c . The linear fit will then use only 2 free parameters, a and b , as written in Equation 4.7. This gives
 1396 us the results showed in Figure 4.15. Figure 4.15b confirms that using only a linear fit to extract c is
 1397 enough as the evolution of the rate that can be obtained superimposes well on the simulation points.

$$c \left(\frac{D}{D_0} \right) = a \frac{D}{D_0} + b \quad (4.7)$$

$$F^{ABS} = F_0^{ABS} \left(a + \frac{bD_0}{D} \right)^2 \quad (4.8)$$

$$\Delta F^{ABS} = F^{ABS} \left[\frac{\Delta F_0^{ABS}}{F_0^{ABS}} + 2 \frac{\Delta a + \Delta b \frac{D_0}{D}}{a + \frac{bD_0}{D}} \right] \quad (4.9)$$

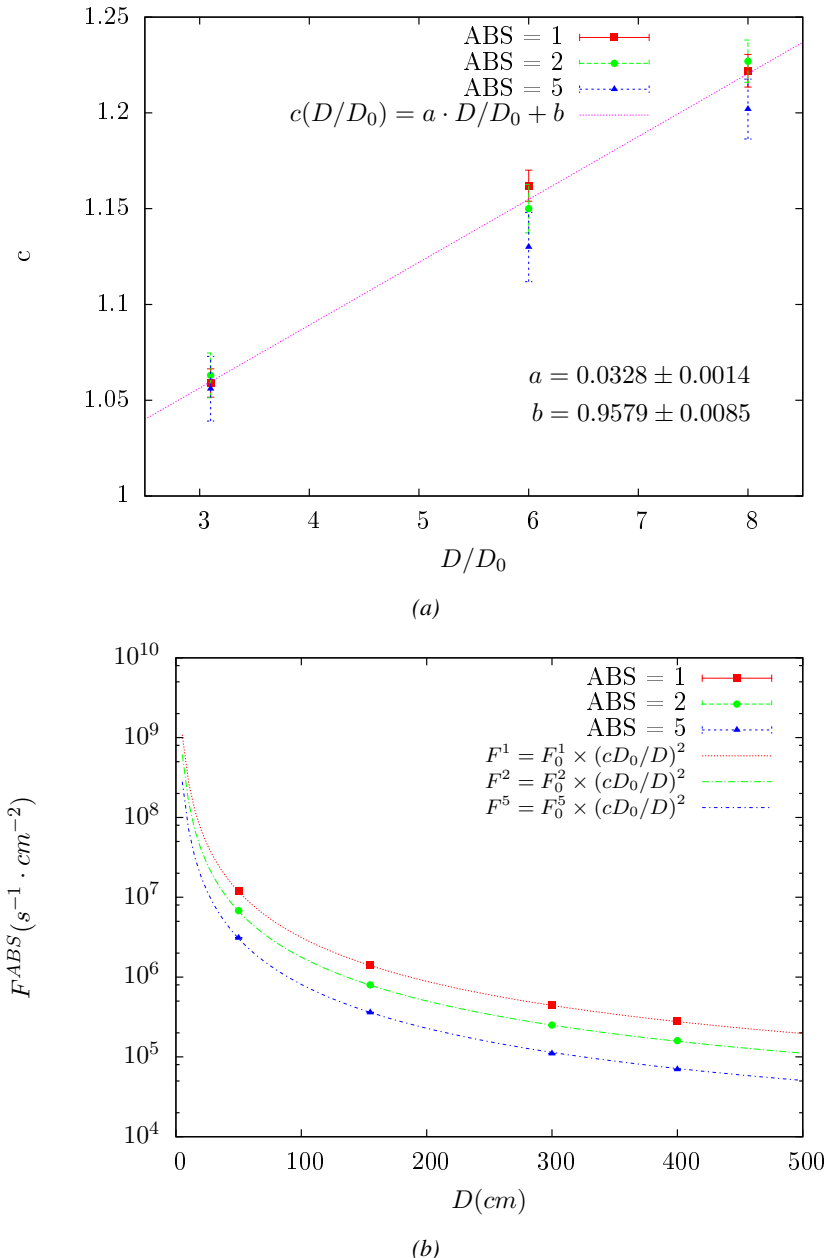


Figure 4.15: Figure 4.15a shows the linear approximation fit done via formulae 4.7 on data from table 4.2. Figure 4.15b shows a comparison of this model with the simulated flux using a and b given in figure 4.15a in formulae 4.4 and the reference value $D_0 = 50\text{cm}$ and the associated flux for each absorption factor F_0^{ABS} from table 4.1

1398 In the case of the 2014 GIF tests, the RPC plane is located at a distance $D = 206\text{ cm}$ to the source.
 1399 Moreover, to estimate the strength of the flux in 2014, it is necessary to consider the nuclear decay
 1400 through time associated to the Cesium source whose half-life is well known ($t_{1/2} = (30.05 \pm 0.08)\text{ y}$).
 1401 The very first source activity measurement has been done on the 5th of March 1997 while the GIF

1402 tests where done in between the 20th and the 31st of August 2014, i.e. at a time $t = (17.47 \pm 0.02)$ y
 1403 resulting in an attenuation of the activity from 740 GBq in 1997 to 494 GBq in 2014. All the needed
 1404 information to extrapolate the flux through our detector in 2014 has now been assembled, leading
 1405 to the Table 4.3. It is interesting to note that for a common RPC sensitivity to γ of $2 \cdot 10^{-3}$, the
 1406 order of magnitude of the estimated hit rate per unit area is of the order of the kHz for the fully
 1407 opened source. Moreover, taking profit of the two working absorbers, it will be possible to scan
 1408 background rates at 0 Hz, ~ 300 Hz as well as ~ 600 Hz. Without source, a good estimate of the
 1409 intrinsic performance will be available. Then at 300 Hz, the goal will be to show that the detectors
 1410 fulfill the performance certification of CMS RPCs. Then a first idea of the performance of the
 1411 detectors at higher background will be provided with absorption factors 2 (~ 600 Hz) and 1 (no
 1412 absorption). *[Here I will also put a reference to the plot showing the estimated background rate at
 1413 the level of RE3/1 in the case of HL-LHC but this one being in another chapter, I will do it later.]*

Nominal ABS	Photon flux F [$s^{-1}cm^{-2}$]			Hit rate/unit area [$Hz cm^{-2}$] at $D^{2014} = 206$ cm
	at $D_0^{1997} = 50$ cm	at $D^{1997} = 206$ cm	at $D^{2014} = 206$ cm	
1	$0.12 \cdot 10^8 \pm 0.2\%$	$0.84 \cdot 10^6 \pm 0.3\%$	$0.56 \cdot 10^6 \pm 0.3\%$	1129 ± 32
2	$0.68 \cdot 10^7 \pm 0.3\%$	$0.48 \cdot 10^6 \pm 0.3\%$	$0.32 \cdot 10^6 \pm 0.3\%$	640 ± 19
5	$0.31 \cdot 10^7 \pm 0.4\%$	$0.22 \cdot 10^6 \pm 0.3\%$	$0.15 \cdot 10^6 \pm 0.3\%$	292 ± 9

Table 4.3: The data at D_0 in 1997 is taken from [55]. In a second step, using Equations 4.8 and 4.9, the flux at D can be estimated in 1997. Then, taking into account the attenuation of the source activity, the flux at D can be estimated at the time of the tests in GIF in 2014. Finally, assuming a sensitivity of the RPC to γ $s = 2 \cdot 10^{-3}$, an estimation of the hit rate per unit area is obtained.

1414 **4.3.4.2 Dose measurements**

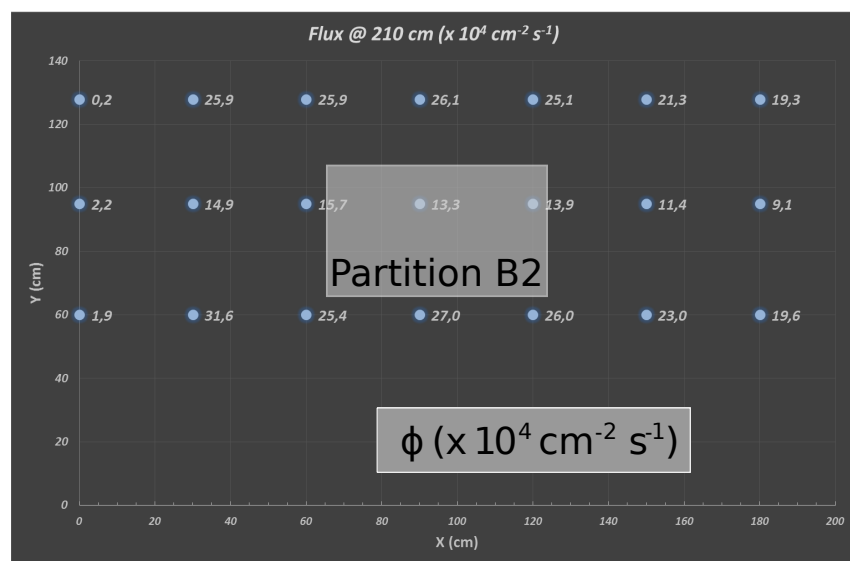


Figure 4.16: Dose measurements has been done in a plane corresponding to the tents front side. This plan is 1900 mm away from the source. As explained in the first chapter, a lens-shaped lead filter provides a uniform photon flux in the vertical plan orthogonal to the beam direction. If the second line of measured fluxes is not taken into account because of lower values due to experimental equipments in the way between the source and the tent, the uniformity of the flux is well showed by the results.

¹⁴¹⁵ **4.3.5 Results and discussions**

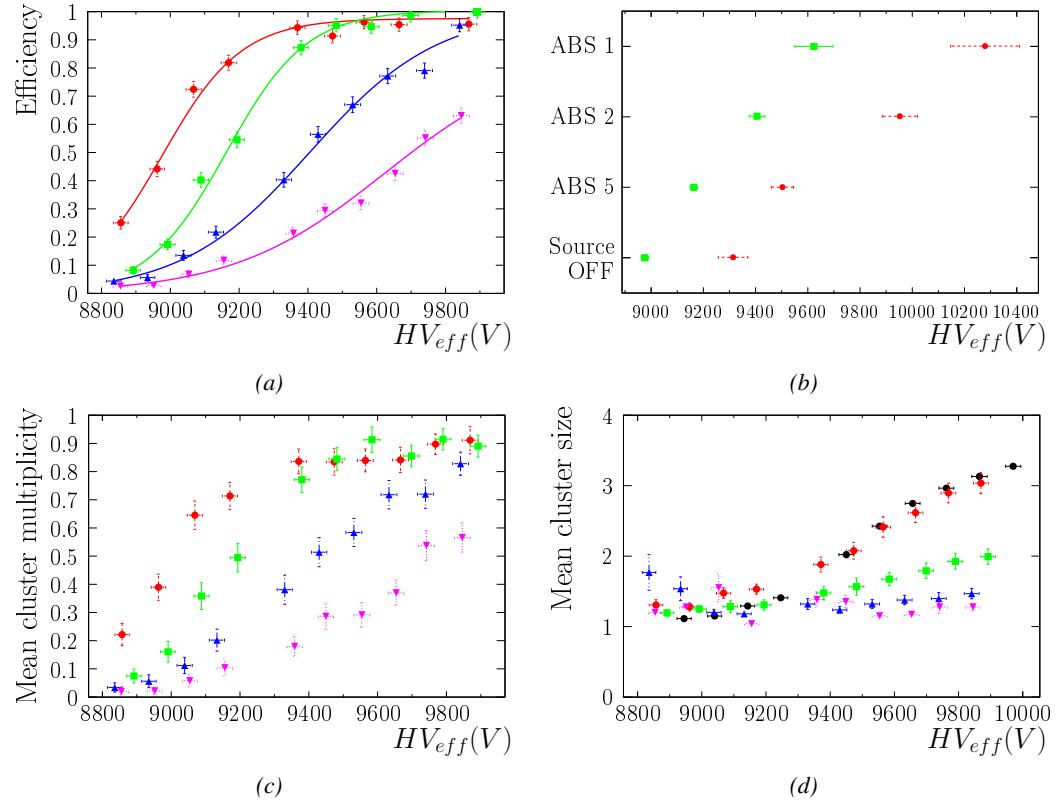


Figure 4.17

1416 4.4 Longevity tests at GIF++

1417 Longevity studies imply a monitoring of the performance of the detectors probed using a high inten-
1418 sity muon beam in a irradiated environment by periodically measuring their rate capability, the dark
1419 current running through them and the bulk resistivity of the Bakelite composing their electrodes.
1420 GIF++, with its very intense ^{137}Cs source, provides the perfect environment to perform such kind
1421 of tests. Assuming a maximum acceleration factor of 3, it is expected to accumulate the equivalent
1422 charge in 1.7 years.

1423 As the maximum background is found in the endcap, the choice naturally was made to focus the
1424 GIF++ longevity studies on endcap chambers. Most of the RPC system was installed in 2007. Nev-
1425 ertheless, the large chambers in the fourth endcap (RE4/2 and RE4/3) have been installed during
1426 LS1 in 2014. The Bakelite of these two different productions having different properties, four spare
1427 chambers of the present system were selected, two RE2,3/2 spares and two RE4/2 spares. Having
1428 two chambers of each type allows to always keep one of them non irradiated as reference, the per-
1429 formance evolution of the irradiated chamber being then compared through time to the performance
1430 of the non irradiated one.

1431 The performance of the detectors under different level of irradiation is measured periodically dur-
1432 ing dedicated test beam periods using the H4 muon beam. In between these test beam periods, the
1433 two RE2,3/2 and RE4/2 chambers selected for this study are irradiated by the ^{137}Cs source in order
1434 to accumulate charge and the gamma background is monitored, as well as the currents. The two
1435 remaining chambers are kept non-irradiated as reference detectors. Due to the limited gas flow in
1436 GIF++, the RE4 chamber remained non-irradiated until end of November 2016 where a new mass
1437 flow controller has been installed allowing for bigger volumes of gas to flow in the system.

1438 Figures 4.18 and 4.19 give us for different test beam periods, and thus for increasing integrated
1439 charge through time, a comparison of the maximum efficiency, obtained using a sigmoid-like func-
1440 tion, and of the working point of both irradiated and non irradiated chambers [**SIGMOID2005**]. No
1441 aging is yet to see from this data, the shifts in γ rate per unit area in between irradiated and non
1442 irradiated detectors and RE2 and RE4 types being easily explained by a difference of sensitivity due
1443 to the various Bakelite resistivities of the HPL electrodes used for the electrode production.

1444 Collecting performance data at each test beam period allows us to extrapolate the maximum effi-
1445 ciency for a background hit rate of $300\text{ Hz}/\text{cm}^2$ corresponding to the expected HL-LHC conditions.
1446 Aging effects could emerge from a loss of efficiency with increasing integrated charge over time,
1447 thus Figure 4.20 helps us understand such degradation of the performance of irradiated detectors in
1448 comparison with non irradiated ones. The final answer for an eventual loss of efficiency is given in
1449 Figure 4.21 by comparing for both irradiated and non irradiated detectors the efficiency sigmoids
1450 before and after the longevity study. Moreover, to complete the performance information, the Bake-
1451 lite resistivity is regularly measured thanks to Ag scans (Figure 4.22) and the noise rate is monitored
1452 weekly during irradiation periods (Figure 4.23). At the end of 2016, no signs of aging were observed
1453 and further investigation is needed to get closer to the final integrated charge requirements proposed
1454 for the longevity study of the present CMS RPC sub-system.

1455

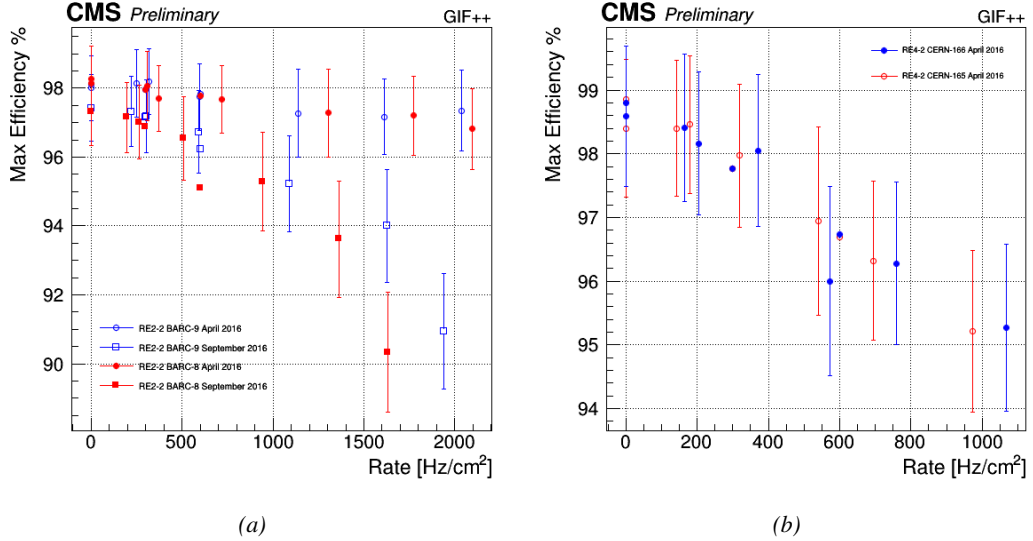


Figure 4.18: Evolution of the maximum efficiency for RE2 (4.18a) and RE4 (4.18b) chambers with increasing extrapolated γ rate per unit area at working point. Both irradiated (blue) and non irradiated (red) chambers are shown.

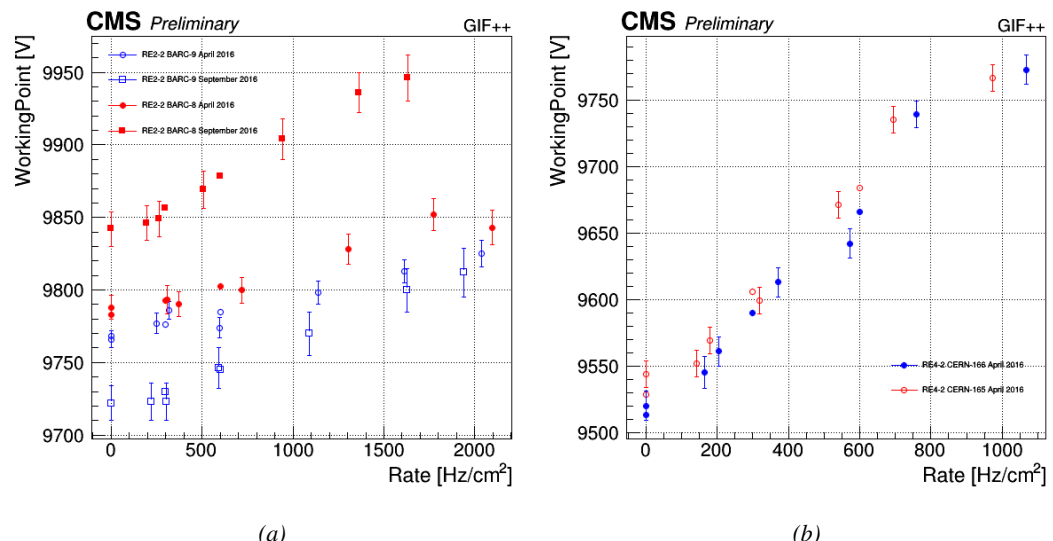


Figure 4.19: Evolution of the working point for RE2 (4.19a) and RE4 (4.19b) with increasing extrapolated γ rate per unit area at working point. Both irradiated (blue) and non irradiated (red) chambers are shown.

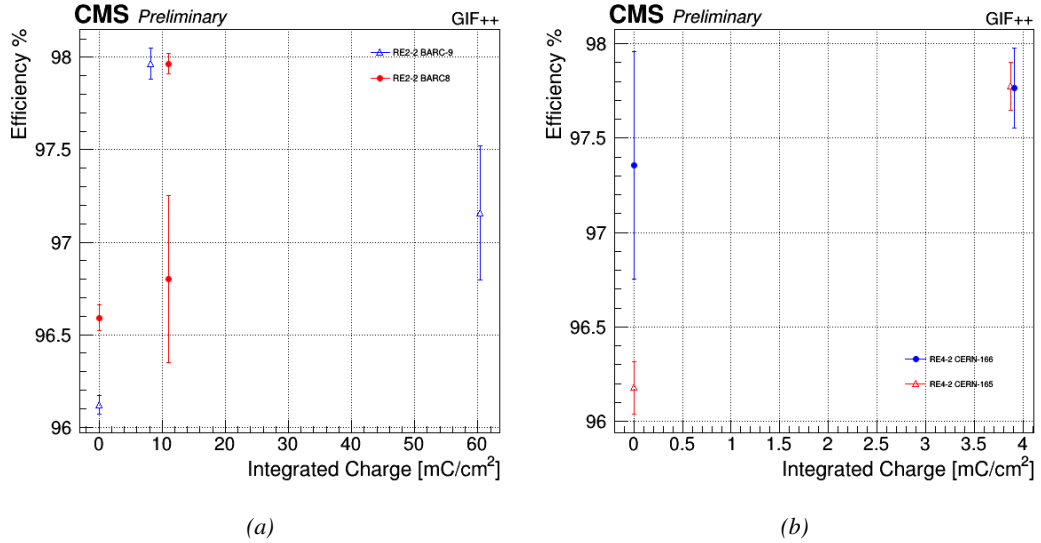


Figure 4.20: Evolution of the maximum efficiency at HL-LHC conditions, i.e. a background hit rate per unit area of 300 Hz/cm², with increasing integrated charge for RE2 (4.20a) and RE4 (4.20b) detectors. Both irradiated (blue) and non irradiated (red) chambers are shown. The integrated charge for non irradiated detectors is recorded during test beam periods and stays small with respect to the charge accumulated in irradiated chambers.

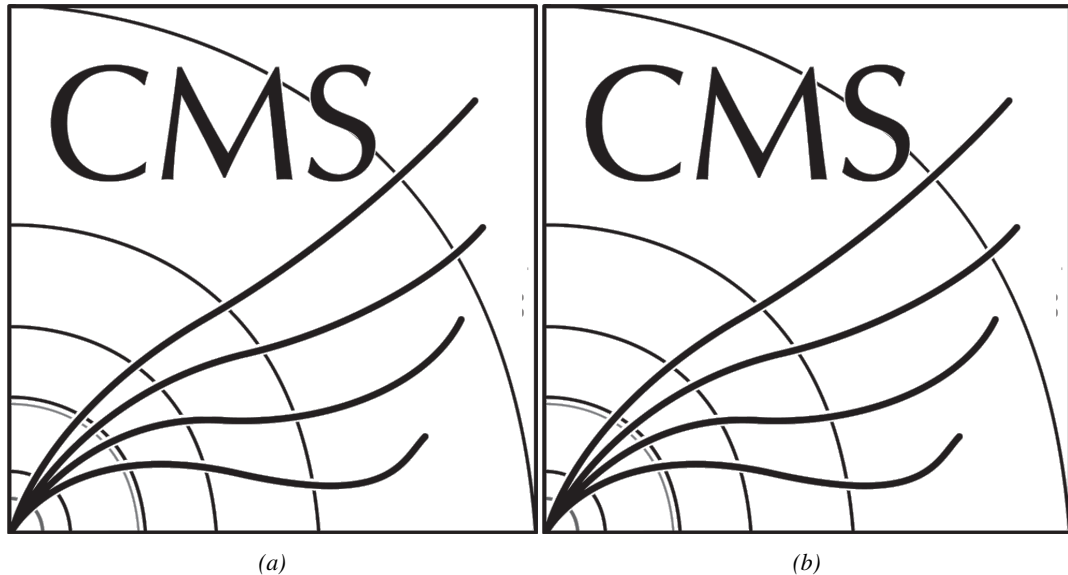


Figure 4.21: Comparison of the efficiency sigmoid before (triangles) and after (circles) irradiation for RE2 (4.21a) and RE4 (4.21b) detectors. Both irradiated (blue) and non irradiated (red) chambers are shown.

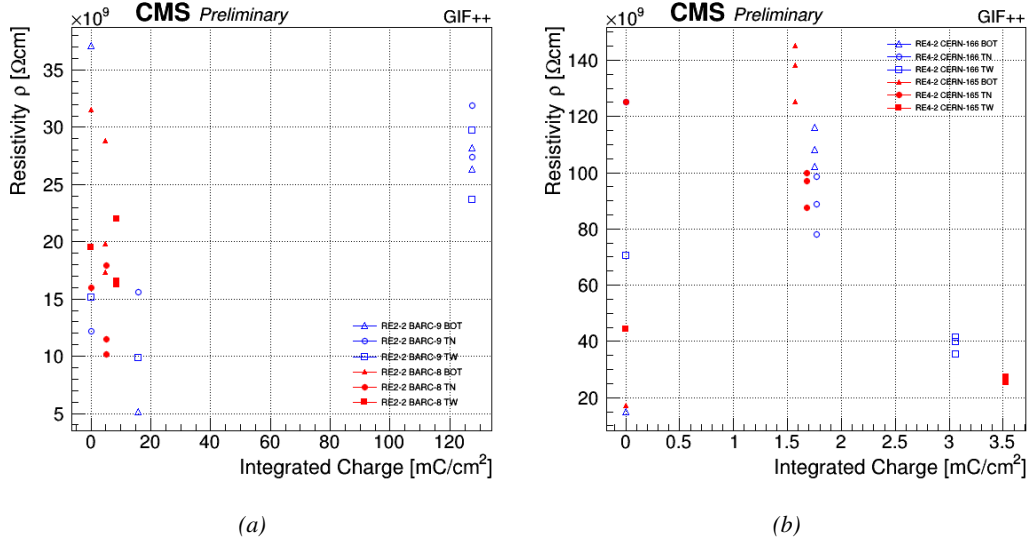


Figure 4.22: Evolution of the Bakelite resistivity for RE2 (4.22a) and RE4 (4.22b) detectors. Both irradiated (blue) and non-irradiated (red) chambers are shown.

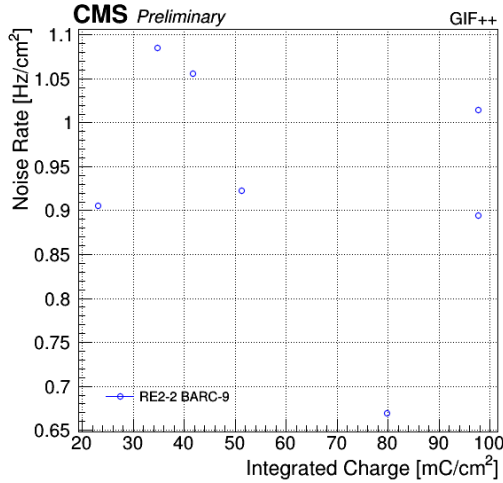


Figure 4.23: Evolution of the noise rate per unit area for the irradiated chamber RE2-2-BARC-9 only.

4.4.1 Description of the Data Acquisition

For the longevity studies, four spare chambers of the present system are used. Two spare RPCs of the RE2,3 stations as well as two spare RPCs from the new RE4 stations have been mounted in a Trolley. Six RE4 gaps are also placed in the trolley. The trolley is placed inside the GIFT++ in the upstream region of the bunker, taking the cesium source as a reference. The trolley is oriented for the detection surface of the chambers to be orthogonal to the beam line. The system can be moved along the orthogonal plane in order to have the beam in all η -partitions. For the aging the trolley is

1463 moved outside the beam line and is placed in a distance of 5.2 m to the source, which irradiates the
 1464 bunker using an attenuation filter of 2.2 which corresponds to a fluence of 10^7 gamma/cm^2 .

1465 During GIF++ operation, the data collected can be divided into different categories as several
 1466 parameters are monitored in addition to the usual RPC performance data. On one hand, to know
 1467 the performance of a chamber, it is need to measure its efficiency and to know the background
 1468 conditions in which it is operated. To do this, the hit signals from the chamber are recorded and
 1469 stored in a ROOT file via a Data Acquisition (DAQ) software. On the other hand, it is also very
 1470 important to monitor parameters such as environmental pressure and temperature, gas temperature
 1471 and humidity, RPC HV, LV, and currents, or even source and beam status. This is done through the
 1472 GIF++ web Detector Control Software (DCS) that stores this information in a database.

1473 Two different types of tests are conducted on RPCs via the DAQ. Indeed, the performance of the
 1474 detectors is measured periodically during dedicated test beam periods using the H4 muon beam. In
 1475 between these test beam periods, when the beam is not available, the chambers are irradiated by the
 1476 ^{137}Cs in order to accumulate deposited charge and the gamma background is measured.

1477 RPCs under test are connected through LVDS cables to V1190A Time-to-Digital Converter
 1478 (TDC) modules manufactured by CAEN. These modules, located in the rack area outside of the
 1479 bunker, get the logic signals sent by the chambers and save them into their buffers. Due to the
 1480 limited size of the buffers, the collected data is regularly erased and replaced. A trigger signal is
 1481 needed for the TDC modules to send the useful data to the DAQ computer via a V1718 CAEN USB
 1482 communication module.

1483 In the case of performance test, the trigger signal used for data acquisition is generated by the
 1484 coincidence of three scintillators. A first one is placed upstream outside of the bunker, a second one
 1485 is placed downstream outside of the bunker, while a third one is placed in front of the trolley, close by
 1486 the chambers. Every time a trigger is sent to the TDCs, i.e. every time a muon is detected, knowing
 1487 the time delay in between the trigger and the RPC signals, signals located in the right time window
 1488 are extracted from the buffers and saved for later analysis. Signals are taken in a time window of
 1489 400 ns centered on the muon peak (here we could show a time spectrum). On the other hand, in the
 1490 case of background rate measurement, the trigger signal needs to be "random" not to measure muons
 1491 but to look at gamma background. A trigger pulse is continuously generated at a rate of 300 Hz using
 1492 a dual timer. To integrate an as great as possible time, all signals contained within a time window of
 1493 10us prior to the random trigger signal are extracted form the buffers and saved for further analysis
 1494 (here another time spectrum to illustrate could be useful, maybe even place both spectrum together
 1495 as a single Figure).

1496 The signals sent to the TDCs correspond to hit collections in the RPCs. When a particle hits
 1497 a RPC, it induce a signal in the pickup strips of the RPC readout. If this signal is higher than the
 1498 detection threshold, a LVDS signal is sent to the TDCs. The data is then organised into 4 branches
 1499 keeping track of the event number, the hit multiplicity for the whole setup, and the time and channel
 1500 profile of the hits in the TDCs.

1501 **4.4.2 RPC current, environmental and operation parameter monitoring**

1502 In order to take into account the variation of pressure and temperature between different data taking
 1503 periods the applied voltage is corrected following the relationship :

$$1504 \quad HV_{eff} = HV_{app} \times \left(0.2 + 0.8 \cdot \frac{P_0}{P} \times \frac{T}{T_0} \right) \quad (4.10)$$

1504 where T_0 (=293 K) and P_0 (=990 mbar) are the reference values.

1505 **4.4.3 Measurement procedure**

1506 Insert a short description of the online tools (DAQ, DCS, DQM).

1507 Insert a short description of the offline tools : tracking and efficiency algorithm.

1508 Identify long term aging effects we are monitoring the rates per strip.

1509 **4.4.4 Longevity studies results**

5

1510

1511

Investigation on high rate RPCs

1512 **5.1 Rate limitations and ageing of RPCs**

1513 **5.1.1 Low resistivity electrodes**

1514 **5.1.2 Low noise front-end electronics**

1515 **5.2 Construction of prototypes**

1516 **5.3 Results and discussions**

6

Conclusions and outlooks

1517

1518

¹⁵¹⁹ **6.1 Conclusions**

¹⁵²⁰ **6.2 Outlooks**

A

1521

1522

1523

A data acquisition software for CAEN VME TDCs

1524 Certifying detectors in the perspective of HL-LHC required to develop tools for the GIF++ experiment.
1525 Among them was the C++ Data Acquisition (DAQ) software that allows to make the communications
1526 in between a computer and TDC modules in order to retrieve the RPC data [57]. In this
1527 appendix, details about this software, as of how the software was written, how it functions and how
1528 it can be exported to another similar setup, will be given.

1529 A.1 GIF++ DAQ file tree

1530 GIF++ DAQ source code is fully available on github at https://github.com/afagot/GIF_DAQ. The software requires 3 non-optional dependencies:

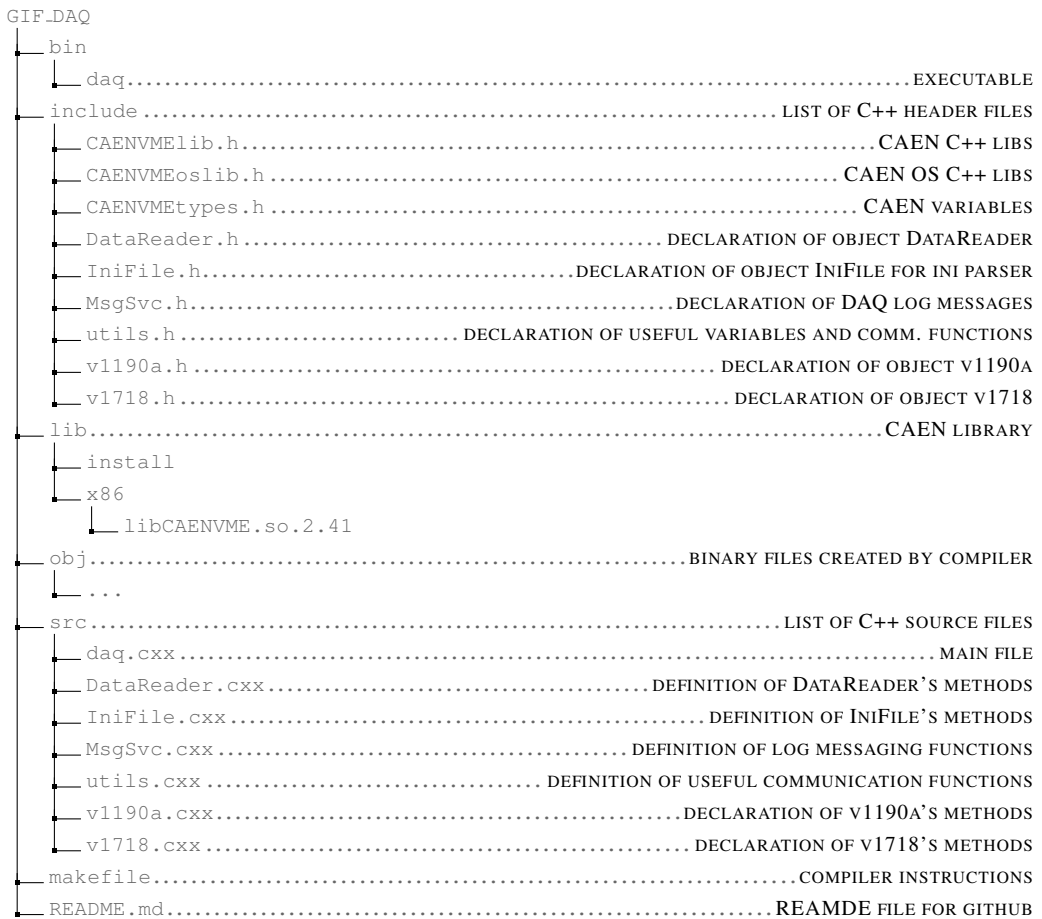
- 1532 • CAEN USB Driver, to mount the VME hardware,
- 1533 • CAEN VME Library, to communicate with the VME hardware, and
- 1534 • ROOT, to organize the collected data into a TTree.

1535 The CAEN VME library will not be packaged by distributions and will need to be installed man-
1536 ually. To compile the GIF++ DAQ project via a terminal, from the DAQ folder use the command:

1537 `make`

1539 The source code tree is provided below along with comments to give an overview of the files' con-
1540 tent. The different objects created for this project (`v1718`, `v1190a`, `IniFile` & `DataReader`) will be
1541 described in details in the following sections.

1542



1543 A.2 Usage of the DAQ

1544 GIF++ DAQ, as used in GIF++, is not a standalone software. Indeed, the system being more complexe,
 1545 the DAQ only is a sub-layer of the software architecture developped to control and monitor
 1546 the RPCs that are placed into the bunker for performance study in an irradiated environment. The top
 1547 layer of GIF++ is a Web Detector Control System (webDCS) application. The DAQ is only called
 1548 by the webDCS when data needs to be acquired. The webDCS operates the DAQ through command
 1549 line. To start the DAQ, the webDCS calls:

1550
 1551 bin/daq /path/to/the/log/file/in/the/output/data/folder

1552 where /path/to/the/log/file/in/the/output/data/folder is the only argument required. This
 1553 log file is important for the webDCS as this file contains all the content of the communication of the
 1554 webDCS and the different systems monitored by the webDCS. Its content is constantly displayed
 1555 during data taking for the users to be able to follow the operations. The communication messages
 1556 are normally sent to the webDCS log file via the functions declared in file MsgSvc.h, typically
 1557 MSG_INFO(string message).

1558

1559 A.3 Description of the readout setup

1560 The CMS RPC setup at GIF++ counts 5 V1190A Time-to-Digital Converter (TDC) manufactured
 1561 by CAEN [58]. V1190A are VME units accepting 128 independent Multi-Hit/Multi-Event TDC
 1562 channels whose signals are treated by 4 100 ps high performance TDC chips developed by CERN
 1563 / ECP-MIC Division. The communication between the computer and the TDCs to transfer data is
 1564 done via a V1718 VME master module also manufactured by CAEN and operated from a USB
 1565 port [59]. These VME modules are all hosted into a 6U VME 6021 powered crate manufactured by
 1566 W-Ie-Ne-R than can accommodate up to 21 VME bus cards [60]. These 3 components of the DAQ
 1567 setup are shown in Figure A.1.

1568

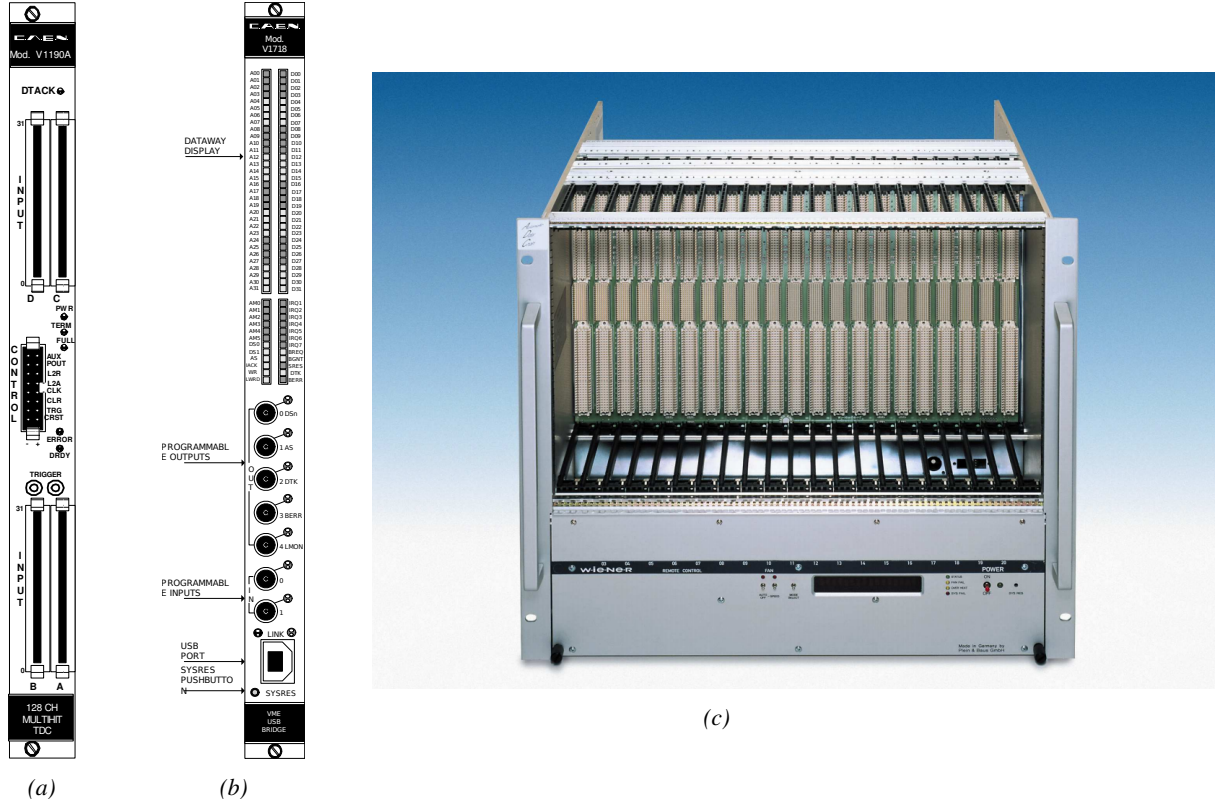


Figure A.1: (A.1a) View of the front panel of a V1190A TDC module [58]. (A.1b) View of the front panel of a V1718 Bridge module [59]. (A.1c) View of the front panel of a 6U 6021 VME crate [60].

1569

A.4 Data read-out

1570 To efficiently perform a data readout algorithm, C++ objects to handle the VME modules (TDCs
 1571 and VME bridge) have been created along with objects to store data and read the configuration file

1572 that comes as an input of the DAQ software.

1573

1574 A.4.1 V1190A TDCs

1575 The DAQ used at GIF takes profit of the *Trigger Matching Mode* offered by V1190A modules.
 1576 This setting is enabled through the method `v1190a::SetTrigMatching (int ntdcs)` where `ntdcs`
 1577 is the total number of TDCs in the setup this setting needs to be enabled for (Source Code A.1). A
 1578 trigger matching is performed in between a trigger time tag, a trigger signal sent into the TRIGGER
 1579 input of the TDC visible on Figure A.1a, and the channel time measurements, signals recorded from
 1580 the detectors under test in our case. Control over this data acquisition mode, explained through
 1581 Figure A.2, is offered via 4 programmable parameters:

- 1582 • **match window:** the matching between a trigger and a hit is done within a programmable time
 1583 window. This is set via the method

```
1584     void v1190a::SetTrigWindowWidth(UINT windowWidth, int ntdcs)
```

- 1585 • **window offset:** temporal distance between the trigger tag and the start of the trigger matching
 1586 window. This is set via the method

```
1587     void v1190a::SetTrigWindowWidth(UINT windowWidth, int ntdcs)
```

- 1588 • **extra search margin:** an extended time window is used to ensure that all matching hits are
 1589 found. This is set via the method

```
1590     void v1190a::SetTrigSearchMargin(UINT searchMargin, int ntdcs)
```

- 1591 • **reject margin:** older hits are automatically rejected to prevent buffer overflows and to speed
 1592 up the search time. This is set via the method

```
1593     void v1190a::SetTrigRejectionMargin(UINT rejectMargin, int ntdcs)
```

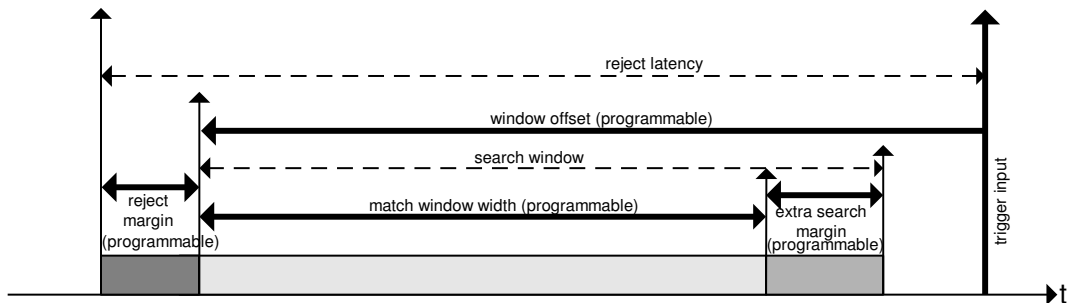


Figure A.2: Module V1190A Trigger Matching Mode timing diagram [58].

1594 Each of these 4 parameters are given in number of clocks, 1 clock being 25 ns long. It is easy to
 1595 understand at this level that there are 3 possible functioning settings:

- 1596 • **1:** the match window is entirely contained after the trigger signal,

- 1597 • **2:** the match window overlaps the trigger signal, or

- 1598 • **3:** the match window is entirely contained before the trigger signal as displayed on Figure A.2.

1599 In both the first and second cases, the sum of the window width and of the offset can be set to
1600 a maximum of 40 clocks, which corresponds to 1 μ s. Evidently, the offset can be negative, allowing
1601 for a longer match window, with the constraint of having the window ending at most 1 μ s after the
1602 trigger signal. In the third case, the maximum negative offset allowed is of 2048 clocks (12 bit) cor-
1603 responding to 51.2 μ s, the match window being strictly smaller than the offset. In the case of GIF++,
1604 the choice has been made to use this last setting by delaying the trigger signal. During the studies
1605 performed in GIF++, both the efficiency of the RPCs, probed using a muon beam, and the noise or
1606 gamma background rate are monitored. The extra search and reject margins are left unused.
1607 To probe the efficiency of RPC detectors, the trigger time tag is provided by the coïncidence of
1608 scintillators when a bunch of muons passes through GIF++ area is used to trigger the data acquisi-
1609 tion. For this measurement, it is useful to reduce the match window width only to contain the muon
1610 information. Indeed, the delay in between a trigger signal and the detection of the corresponding
1611 muon in the RPC being very contant (typically a few tens of ns due to jitter and cable length), the
1612 muon signals are very localised in time. Thus, due to a delay of approximalety 325 ns in between
1613 the muons and the trigger, the settings where chosen to have a window width of 24 clocks (600 ns)
1614 centered on the muon peak thanks to a negative offset of 29 clocks (725 ns).
1615 On the otherhand, monitoring the rates don't require for the DAQ to look at a specific time window.
1616 It is important to integrate enough time to have a robust measurement of the rate as the number of
1617 hits per time unit. The triggerring signal is provided by a pulse generator at a frequency of 300 Hz
1618 to ensure that the data taking occurs in a random way, with respect to beam physics, to probe only
1619 the irradiation spectrum on the detectors. The match window is set to 400 clocks (10 μ s) and the
1620 negative offset to 401 clocks as it needs to exceed the value of the match window.

```

1621
class v1190a
{
    private :
        long Handle;
        vector<Data32> Address;
        CVDataWidth DataWidth;
        CVAAddressModifier AddressModifier;

    public:

        v1190a(long handle, IniFile *inifile, int ntdcs);
        ~v1190a();
        Data16 write_op_reg(Data32 address, int code, string error);
        Data16 read_op_reg(Data32 address, string error);
        void Reset(int ntdcs);
        void Clear(int ntdcs);
        void TestWR(Data16 value,int ntdcs);
        void CheckTDCStatus(int ntdcs);
        void CheckCommunication(int ntdcs);
        void SetTDCTestMode(Data16 mode,int ntdcs);
        void SetTrigMatching(int ntdcs);
        void SetTrigTimeSubtraction(Data16 mode,int ntdcs);
        void SetTrigWindowWidth(Uint windowHeight,int ntdcs);
        void SetTrigWindowOffset(Uint windowOffset,int ntdcs);
        void SetTrigSearchMargin(Uint searchMargin,int ntdcs);
        void SetTrigRejectionMargin(Uint rejectMargin,int ntdcs);
        void GetTrigConfiguration(int ntdcs);
        void SetTrigConfiguration(IniFile *inifile,int ntdcs);
        void SetTDCDetectionMode(Data16 mode,int ntdcs);
        void SetTDCResolution(Data16 lsb,int ntdcs);
        void SetTDCDeadTime(Data16 time,int ntdcs);
        void SetTDCHeadTrailer(Data16 mode,int ntdcs);
        void SetTDCEventSize(Data16 size,int ntdcs);
        void SwitchChannels(IniFile *inifile,int ntdcs);
        void SetIRQ(Data32 level, Data32 count,int ntdcs);
        void SetBlockTransferMode(Data16 mode,int ntdcs);
        void Set(IniFile *inifile,int ntdcs);
        void CheckStatus(CVErrorCodes status) const;
        int ReadBlockD32(Uint tdc, const Data16 address,
                           Data32 *data, const Uint words, bool ignore_berr);
        Uint Read(RAWData *DataList,int ntdcs);
};

1622

```

1623 *Source Code A.1: Description of C++ object v1190a.*

1624 The v1190a object, defined in the DAQ software as in Source Code A.1, offers the possibility to
 1625 concatenate all TDCs in the readout setup into a single object containing a list of hardware addresses
 1626 (addresses to access the TDCs' buffer through the VME crate) and each constructor and method acts
 1627 on the list of TDCs.

1628

1629 A.4.2 DataReader

1630 Enabled thanks to v1190a::SetBlockTransferMode(Data16 mode, **int** ntdcs), the data transfer
 1631 is done via Block Transfer (BLT). Using BLT allows to tranfer a fixed number of events called a
 1632 *block*. This is used together with an Almost Full Level (AFL) of the TDCs' output buffers, defined

1633 through `v1190a::SetIRQ(Data32 level, Data32 count, int ntdcs)`. This AFL gives the maximum amount of 32735 words (16 bits, corresponding to the depth of a TDC output buffer) that can
 1634 written in a buffer before an Interrupt Request (IRQ) is generated and seen by the VME Bridge,
 1635 stopping the data acquisition to transfer the content of each TDC buffers before resuming. For each
 1636 trigger, 6 words or more are written into the TDC buffer:

- 1638 • a **global header** providing information of the event number since the beginning of the data
 acquisition,
- 1640 • a **TDC header**,
- 1641 • the **TDC data** (*if any*), 1 for each hit recorded during the event, providing the channel and the
 time stamp associated to the hit,
- 1643 • a **TDC error** providing error flags,
- 1644 • a **TDC trailer**,
- 1645 • a **global trigger time tag** that provides the absolute trigger time relatively to the last reset,
 and
- 1647 • a **global trailer** providing the total word count in the event.

1648 As previously described in Section ??, CMS RPC FEEs provide us with 100 ns long LVDS output
 1649 signals that are injected into the TDCs' input. Any avalanche signal that gives a signal above the
 1650 FEEs threshold is thus recorded by the TDCs as a hit within the match window. Each hit is assigned
 1651 to a specific TDC channel with a time stamp, with a precision of 100 ps. The reference time, $t_0 = 0$,
 1652 is provided by the beginning of the match window. Thus for each trigger, coming from a scintillator
 1653 coïncidence or the pulse generator, a list of hits is stored into the TDCs' buffers and will then be
 1654 transferred into a ROOT Tree.

1655 When the BLT is used, it is easy to understand that the maximum number of words that have
 1656 been set as ALF will not be a finite number of events or, at least, the number of events that would
 1657 be recorded into the TDC buffers will not be a multiple of the block size. In the last BLT cycle to
 1658 tranfer data, the number of events to transfer will most probably be lower than the block size. In that
 1659 case, the TDC can add fillers at the end of the block but this option requires to send more data to the
 1660 computer and is thus a little slower. Another solution is to finish the transfer after the last event by
 1661 sending a bus error that states that the BLT reached the last event in the pile. This method has been
 1662 chosen in GIF++.

1664 Due to irradiation, an event in GIF++ can count up to 300 words per TDC. A limit of 4096 words
 1665 (12 bits) has been set to generate IRQ which represent from 14 to almost 700 events depending on
 1666 the average of hits collected per event. Then the block size has been set to 100 events with enabled
 1667 bus errors. When an AFL is reached for one of the TDCs, the VME bridge stops the acquisition by
 1668 sending a BUSY signal.

1670

1671 The data is then transferred one TDC at a time into a structure called `RAWData` (Source Code A.2).

```
1672
1673   struct RAWData{
1674     vector<int>           *EventList;
1675     vector<int>           *NHitsList;
1676     vector<int>           *QFlagList;
1677     vector<vector<int> >  *Channellist;
1678     vector<vector<float> > *TimeStampList;
1679   };
```

1674 *Source Code A.2: Description of data holding C++ structure `RAWData`.*

1675 In order to organize the data transfer and the data storage, an object called `DataReader` was
1676 created (Source Code A.3). On one hand, it has `v1718` and `v1190a` objects as private members for
1677 communication purposes, such as VME modules settings via the configuration file `*iniFile` or data
1678 read-out through `v1190a::Read()` and on the other hand, it contains the structure `RAWData` that allows
1679 to organise the data in vectors reproducing the tree structure of a ROOT file.

```
1680
1681   class DataReader
1682   {
1683     private:
1684       bool      StopFlag;
1685       IniFile *iniFile;
1686       Data32  MaxTriggers;
1687       v1718   *VME;
1688       int      nTDCs;
1689       v1190a  *TDCs;
1690       RAWData TDCData;
1691
1692     public:
1693       DataReader();
1694       virtual ~DataReader();
1695       void      SetIniFile(string inifilename);
1696       void      SetMaxTriggers();
1697       Data32  GetMaxTriggers();
1698       void      SetVME();
1699       void      SetTDC();
1700       int      GetQFlag(Uint it);
1701       void      Init(string inifilename);
1702       void      FlushBuffer();
1703       void      Update();
1704       string  GetFileName();
1705       void      WriteRunRegistry(string filename);
1706       void      Run();
1707   };
```

1682 *Source Code A.3: Description of C++ object `DataReader`.*

1683 Each event is transferred from `TDCData` and saved into branches of a ROOT `TTree` as 3 integers
1684 that represent the event ID (`EventCount`), the number of hits read from the TDCs (`nHits`), and the
1685 quality flag that provides information for any problem in the data transfer (`qflag`), and 2 lists of
1686 `nHits` elements containing the fired TDC channels (`TDCCh`) and their respective time stamps (`TDCTS`),
1687 as presented in Source Code A.4. The ROOT file file is named using information contained into
1688 the configuration file, presented in section A.5.2. The needed information is extracted using method
1689 `DataReader::GetFileName()` and allow to build the output filename format `ScanXXXXXX_HVX_DAQ.root`

1690 where ScanXXXXXX is a 6 digit number representing the scan number into GIFT++ database and HVX
 1691 the HV step within the scan that can be more than a single digit. An example of ROOT data file is
 1692 provided with Figure A.3.

```
1693
RAWData TDCData;
TFile *outputFile = new TFile(outputFileName.c_str(),"recreate");
TTree *RAWDataTree = new TTree("RAWData","RAWData");

int EventCount = -9;
int nHits = -8;
int qflag = -7;
vector<int> TDCCh;
vector<float> TDCTS;

RAWDataTree->Branch("EventNumber",&EventCount, "EventNumber/I");
RAWDataTree->Branch("number_of_hits",&nHits,"number_of_hits/I");
RAWDataTree->Branch("Quality_flag",&qflag,"Quality_flag/I");
RAWDataTree->Branch("TDC_channel",&TDCCh);
RAWDataTree->Branch("TDC_TimeStamp",&TDCTS);

1694
//...
//Here read the TDC data using v1190a::Read() and place it into
//TDCData for as long as you didn't collect the requested amount
//of data.
//...

for(Uint i=0; i<TDCData.EventList->size(); i++){
    EventCount = TDCData.EventList->at(i);
    nHits = TDCData.NHitsList->at(i);
    qflag = TDCData.QFlagList->at(i);
    TDCCh = TDCData.ChannelList->at(i);
    TDCTS = TDCData.TimeStampList->at(i);
    RAWDataTree->Fill();
}
```

1695 *Source Code A.4: Highlight of the data transfer and organisation within DataReader::Run() after the data has been collected into TDCData.*

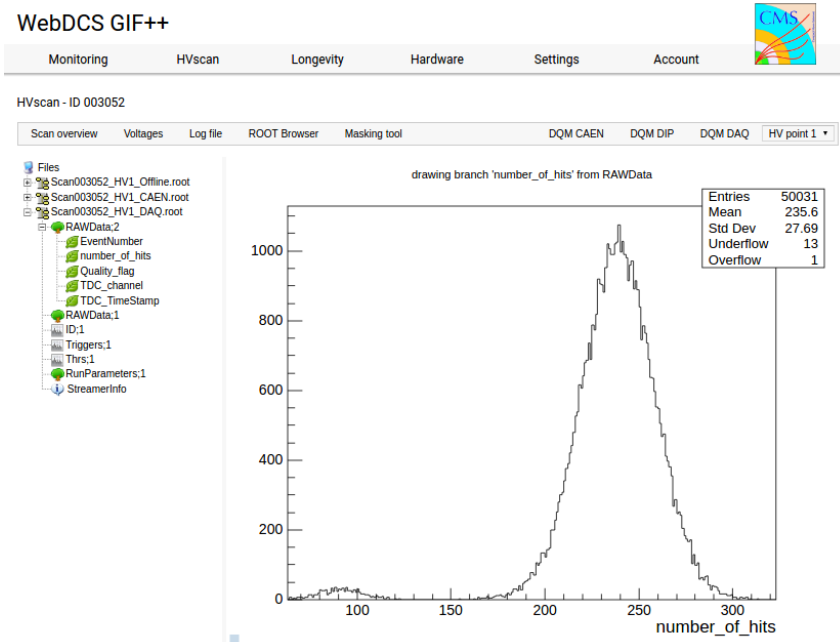


Figure A.3: Structure of the ROOT output file generated by the DAQ. The 5 branches (EventNumber, number_of_hits, Quality_flag, TDC_channel and TDC_TimeStamp) are visible on the left panel of the ROOT browser. On the right panel is visible the histogram corresponding to the variable nHits. In this specific example, there were approximately 50k events recorded to measure the gamma irradiation rate on the detectors. Each event is stored as a single entry in the TTree.

1696 A.4.3 Data quality flag

1697 Among the parameters that are recorded for each event, the quality flag, defined in Source Code A.5,
 1698 is determined on the fly by checking the data recorded by every single TDC. From method `v1190a::Read()`,
 1699 it can be understood that the content of each TDC buffer is readout one TDC at a time. Entries are
 1700 created in the data list for the first TDC and then, when the second buffer is readout, events corre-
 1701 sponding to entries that have already been created to store data for the previous TDC are added to
 1702 the existing list element. On the contrary, when an event entry has not been yet created in the data
 1703 list, a new entry is created.

```
1704
 1705 typedef enum _QualityFlag {
    GOOD      = 1,
    CORRUPTED = 0
} QualityFlag;
```

1706 *Source Code A.5: Definition of the quality flag `enum`.*

1707 It is possible that each TDC buffer contains a different number of events. In cases where the first
 1708 element in the buffer list is an event for corresponds to a new entry, the difference in between the
 1709 entry from the buffer and the last entry in the data list is recorded and checked. If it is greater than 1,
 1710 what should never be the case, the quality flag is set to CORRUPTED for this TDC and an empty entry
 1711 is created in the place of the missing ones. Missing entries are believe to be the result of a bad hold

1712 on the TDC buffers at the moment of the readout. Indeed, the software hold is effective only on 1
 1713 TDC at a time and no solution as been found yet to completely block the writting in the buffers when
 1714 an IRQ is received.

1715 At the end of each BLT cycle, the ID of the last entry stored for each TDC buffer is not recorded.
 1716 When starting the next cycle, if the first entry in the pile corresponds to an event already existing
 1717 in the list, the readout will start from this list element and will not be able to check the difference
 1718 in between this entry's ID and the one of the last entry that was recorded for this TDC buffer in
 1719 the previous cycle. In the case events were missing, the flag stays at its initial value of 0, which is
 1720 similar to CORRUPTED and it is assumed that then this TDC will not contribute to `number_of_hits`,
 1721 `TDC_channel` or `TDC_TimeStamp`.

1722 Finally, since there will be 1 `RAWData` entry per TDC for each event (meaning `nTDCs` entries,
 1723 referring to `DataReader` private attribute), the individual flags of each TDC will be added together.
 1724 The final format is an integer composed `nTDCs` digits where each digit is the flag of a specific TDC.
 1725 This is constructed using powers of 10 like follows:

```
1726     TDC 0: QFlag = 100 × _QualityFlag
1727     TDC 1: QFlag = 101 × _QualityFlag
1728     ...
1729     TDC N: QFlag = 10N × _QualityFlag
```

1730 and the final flag to be with N digits:

```
1731     QFlag = n....3210
```

1732 each digit being 1 or 0. Below is given an example with a 4 TDCs setup.

```
1733     If all TDCs were good : QFlag = 1111,
1734     but if TDC 2 was corrupted : QFlag = 1011.
```

1735 When data taking is over and the data contained in the dynamical `RAWData` structure is transferred
 1736 to the ROOT file, all the 0s are changed into 2s by calling the method `DataReader::GetQFlag()`.
 1737 This will help translating the flag without knowing the number of TDCs beforehand. Indeed, a flag
 1738 111 could be due to a 3 TDC setup with 3 good individual TDC flags or to a more than 3 TDC setup
 1739 with TDCs those ID is greater than 2 being CORRUPTED, thus giving a 0.

1740 The quality flag has been introduced quite late, in October 2017 only, to the list of GIFT++ DAQ
 1741 parameters to be recorded into the output ROOT file. Before this addition, the missing data, corrupting
 1742 the quality for the offline analysis, was contributing to artificially fill data with lower multiplicity.
 1743 Looking at `TBranch number_of_hits` provides an information about the data of the full GIFT++
 1744 setup. When a TDC is not able to transfer data for a specific event, the effect is a reduction of the
 1745 total number of hits recorded in the full setup, this is what can be seen from Figure A.4. After offline
 1746 reconstruction detector by detector, the effect of missing events can be seen in the artificially filled
 1747 bin at multiplicity 0 shown in Figure A.5. Nonetheless, for data with high irradiation levels, as it is
 1748 the case for Figure A.5a, discarding the fake multiplicity 0 data can be done easily during the offline
 1749 analysis. At lower radiation, the missing events contribution becomes more problematic as the multi-
 1750 tiplicity distribution overlaps the multiplicity 0 and that in the same time the proportion of missing

events decreases. Attempts to fit the distribution with a Poisson or skew distribution function were not conclusive and this very problem has been at the origin of the quality flag that allows to give a non ambiguous information about each event quality.

1754

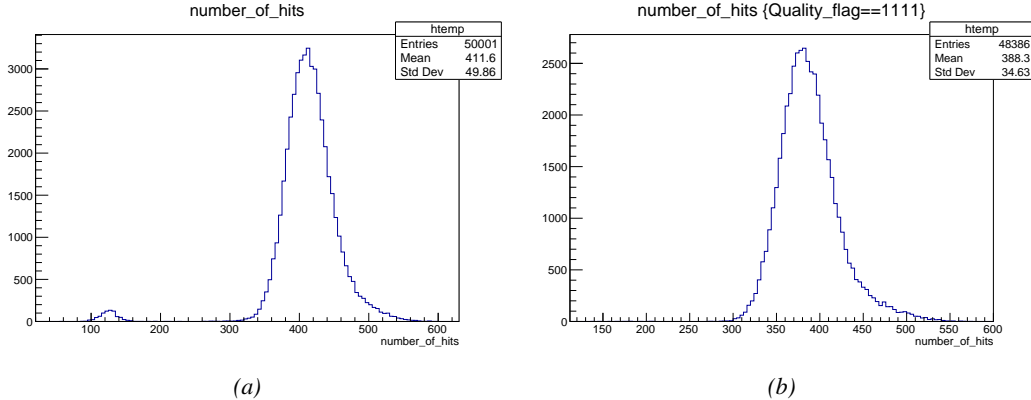


Figure A.4: The effect of the quality flag is explained by presenting the content of TBranch `number_of_hits` of a data file without `Quality_flag` in Figure A.4a and the content of the same TBranch for data corresponding to a `Quality_flag` where all TDCs were labelled as `GOOD` in Figure A.4b taken with similar conditions. It can be noted that the number of entries in Figure A.4b is slightly lower than in Figure A.4a due to the excluded events.

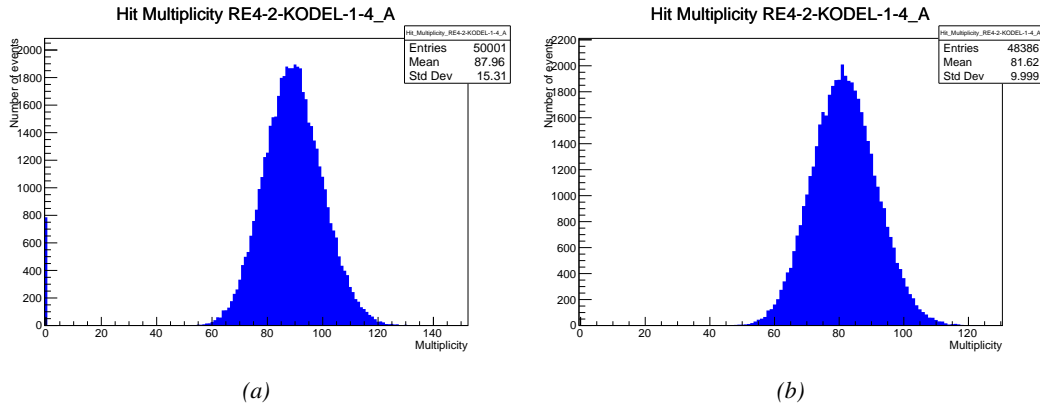


Figure A.5: Using the same data as previously showed in Figure A.4, the effect of the quality flag is explained by presenting the reconstructed hit multiplicity of a data file without `Quality_flag` in Figure A.5a and the reconstructed content of the same RPC partition for data corresponding to a `Quality_flag` where all TDCs were labelled as `GOOD` in Figure A.5b taken with similar conditions. The artificial high content of bin 0 is completely suppressed.

A.5 Communications

To ensure data readout and dialog in between the machine and the TDCs or in between the webDCS and the DAQ, different communication solutions were used. First of all, it is important to have a

1755

1756

1757

1758 module to allow the communication in between the TDCs and the computer from which the DAQ
 1759 operates. When this communication is effective, shifters using the webDCS to control data taking
 1760 can thus send instructions to the DAQ.

1761

1762 A.5.1 V1718 USB Bridge

1763 In the previous section, the data transfer has been discussed. The importance of the `v1718` object
 1764 (Source Code A.6), used as private member of `DataReader`, was not explicated. VME master
 1765 modules are used for communication purposes as they host the USB port that connects the pow-
 1766 ered crate buffer to the computer where the DAQ is installed. From the source code point of view,
 1767 this object is used to control the communication status, by reading the returned error codes with
 1768 `v1718::CheckStatus()`, or to check for IRQs coming from the TDCs through `v1718::CheckIRQ()`.
 1769 Finally, to ensure that triggers are blocked at the hardware level, a NIM pulse is sent out of one of the
 1770 5 programmable outputs (`v1718::SendBUSY()`) to the VETO of the coincidence module where the
 1771 trigger signals originate from. As long as this signal is ON, no trigger can reach the TDCs anymore.
 1772

```
1773
1774
1775
1776
1777
1778
1779
1780
1781
1782
1783
1784
1785
1786
1787
1788
1789
1790
1791
1792
1793
1794
1795
1796
1797
1798
1799
1800
1801
1802
1803
1804
1805
1806
1807
1808
1809
1810
1811
1812
1813
1814
1815
1816
1817
1818
1819
1820
1821
1822
1823
1824
1825
1826
1827
1828
1829
1830
1831
1832
1833
1834
1835
1836
1837
1838
1839
1840
1841
1842
1843
1844
1845
1846
1847
1848
1849
1850
1851
1852
1853
1854
1855
1856
1857
1858
1859
1860
1861
1862
1863
1864
1865
1866
1867
1868
1869
1870
1871
1872
1873
1874
1875
1876
1877
1878
1879
1880
1881
1882
1883
1884
1885
1886
1887
1888
1889
1890
1891
1892
1893
1894
1895
1896
1897
1898
1899
1900
1901
1902
1903
1904
1905
1906
1907
1908
1909
1910
1911
1912
1913
1914
1915
1916
1917
1918
1919
1920
1921
1922
1923
1924
1925
1926
1927
1928
1929
1930
1931
1932
1933
1934
1935
1936
1937
1938
1939
1940
1941
1942
1943
1944
1945
1946
1947
1948
1949
1950
1951
1952
1953
1954
1955
1956
1957
1958
1959
1960
1961
1962
1963
1964
1965
1966
1967
1968
1969
1970
1971
1972
1973
1974
1975
1976
1977
1978
1979
1980
1981
1982
1983
1984
1985
1986
1987
1988
1989
1990
1991
1992
1993
1994
1995
1996
1997
1998
1999
2000
2001
2002
2003
2004
2005
2006
2007
2008
2009
2010
2011
2012
2013
2014
2015
2016
2017
2018
2019
2020
2021
2022
2023
2024
2025
2026
2027
2028
2029
2030
2031
2032
2033
2034
2035
2036
2037
2038
2039
2040
2041
2042
2043
2044
2045
2046
2047
2048
2049
2050
2051
2052
2053
2054
2055
2056
2057
2058
2059
2060
2061
2062
2063
2064
2065
2066
2067
2068
2069
2070
2071
2072
2073
2074
2075
2076
2077
2078
2079
2080
2081
2082
2083
2084
2085
2086
2087
2088
2089
2090
2091
2092
2093
2094
2095
2096
2097
2098
2099
2100
2101
2102
2103
2104
2105
2106
2107
2108
2109
2110
2111
2112
2113
2114
2115
2116
2117
2118
2119
2120
2121
2122
2123
2124
2125
2126
2127
2128
2129
2130
2131
2132
2133
2134
2135
2136
2137
2138
2139
2140
2141
2142
2143
2144
2145
2146
2147
2148
2149
2150
2151
2152
2153
2154
2155
2156
2157
2158
2159
2160
2161
2162
2163
2164
2165
2166
2167
2168
2169
2170
2171
2172
2173
2174
2175
2176
2177
2178
2179
2180
2181
2182
2183
2184
2185
2186
2187
2188
2189
2190
2191
2192
2193
2194
2195
2196
2197
2198
2199
2200
2201
2202
2203
2204
2205
2206
2207
2208
2209
2210
2211
2212
2213
2214
2215
2216
2217
2218
2219
2220
2221
2222
2223
2224
2225
2226
2227
2228
2229
2230
2231
2232
2233
2234
2235
2236
2237
2238
2239
2240
2241
2242
2243
2244
2245
2246
2247
2248
2249
2250
2251
2252
2253
2254
2255
2256
2257
2258
2259
2260
2261
2262
2263
2264
2265
2266
2267
2268
2269
2270
2271
2272
2273
2274
2275
2276
2277
2278
2279
2280
2281
2282
2283
2284
2285
2286
2287
2288
2289
2290
2291
2292
2293
2294
2295
2296
2297
2298
2299
2300
2301
2302
2303
2304
2305
2306
2307
2308
2309
2310
2311
2312
2313
2314
2315
2316
2317
2318
2319
2320
2321
2322
2323
2324
2325
2326
2327
2328
2329
2330
2331
2332
2333
2334
2335
2336
2337
2338
2339
2340
2341
2342
2343
2344
2345
2346
2347
2348
2349
2350
2351
2352
2353
2354
2355
2356
2357
2358
2359
2360
2361
2362
2363
2364
2365
2366
2367
2368
2369
2370
2371
2372
2373
2374
2375
2376
2377
2378
2379
2380
2381
2382
2383
2384
2385
2386
2387
2388
2389
2390
2391
2392
2393
2394
2395
2396
2397
2398
2399
2400
2401
2402
2403
2404
2405
2406
2407
2408
2409
2410
2411
2412
2413
2414
2415
2416
2417
2418
2419
2420
2421
2422
2423
2424
2425
2426
2427
2428
2429
2430
2431
2432
2433
2434
2435
2436
2437
2438
2439
2440
2441
2442
2443
2444
2445
2446
2447
2448
2449
2450
2451
2452
2453
2454
2455
2456
2457
2458
2459
2460
2461
2462
2463
2464
2465
2466
2467
2468
2469
2470
2471
2472
2473
2474
2475
2476
2477
2478
2479
2480
2481
2482
2483
2484
2485
2486
2487
2488
2489
2490
2491
2492
2493
2494
2495
2496
2497
2498
2499
2500
2501
2502
2503
2504
2505
2506
2507
2508
2509
2510
2511
2512
2513
2514
2515
2516
2517
2518
2519
2520
2521
2522
2523
2524
2525
2526
2527
2528
2529
2530
2531
2532
2533
2534
2535
2536
2537
2538
2539
2540
2541
2542
2543
2544
2545
2546
2547
2548
2549
2550
2551
2552
2553
2554
2555
2556
2557
2558
2559
2560
2561
2562
2563
2564
2565
2566
2567
2568
2569
2570
2571
2572
2573
2574
2575
2576
2577
2578
2579
2580
2581
2582
2583
2584
2585
2586
2587
2588
2589
2590
2591
2592
2593
2594
2595
2596
2597
2598
2599
2600
2601
2602
2603
2604
2605
2606
2607
2608
2609
2610
2611
2612
2613
2614
2615
2616
2617
2618
2619
2620
2621
2622
2623
2624
2625
2626
2627
2628
2629
2630
2631
2632
2633
2634
2635
2636
2637
2638
2639
2640
2641
2642
2643
2644
2645
2646
2647
2648
2649
2650
2651
2652
2653
2654
2655
2656
2657
2658
2659
2660
2661
2662
2663
2664
2665
2666
2667
2668
2669
2670
2671
2672
2673
2674
2675
2676
2677
2678
2679
2680
2681
2682
2683
2684
2685
2686
2687
2688
2689
2690
2691
2692
2693
2694
2695
2696
2697
2698
2699
2700
2701
2702
2703
2704
2705
2706
2707
2708
2709
2710
2711
2712
2713
2714
2715
2716
2717
2718
2719
2720
2721
2722
2723
2724
2725
2726
2727
2728
2729
2730
2731
2732
2733
2734
2735
2736
2737
2738
2739
2740
2741
2742
2743
2744
2745
2746
2747
2748
2749
2750
2751
2752
2753
2754
2755
2756
2757
2758
2759
2760
2761
2762
2763
2764
2765
2766
2767
2768
2769
2770
2771
2772
2773
2774
2775
2776
2777
2778
2779
2780
2781
2782
2783
2784
2785
2786
2787
2788
2789
2790
2791
2792
2793
2794
2795
2796
2797
2798
2799
2800
2801
2802
2803
2804
2805
2806
2807
2808
2809
2810
2811
2812
2813
2814
2815
2816
2817
2818
2819
2820
2821
2822
2823
2824
2825
2826
2827
2828
2829
2830
2831
2832
2833
2834
2835
2836
2837
2838
2839
2840
2841
2842
2843
2844
2845
2846
2847
2848
2849
2850
2851
2852
2853
2854
2855
2856
2857
2858
2859
2860
2861
2862
2863
2864
2865
2866
2867
2868
2869
2870
2871
2872
2873
2874
2875
2876
2877
2878
2879
2880
2881
2882
2883
2884
2885
2886
2887
2888
2889
2890
2891
2892
2893
2894
2895
2896
2897
2898
2899
2900
2901
2902
2903
2904
2905
2906
2907
2908
2909
2910
2911
2912
2913
2914
2915
2916
2917
2918
2919
2920
2921
2922
2923
2924
2925
2926
2927
2928
2929
2930
2931
2932
2933
2934
2935
2936
2937
2938
2939
2940
2941
2942
2943
2944
2945
2946
2947
2948
2949
2950
2951
2952
2953
2954
2955
2956
2957
2958
2959
2960
2961
2962
2963
2964
2965
2966
2967
2968
2969
2970
2971
2972
2973
2974
2975
2976
2977
2978
2979
2980
2981
2982
2983
2984
2985
2986
2987
2988
2989
2990
2991
2992
2993
2994
2995
2996
2997
2998
2999
3000
3001
3002
3003
3004
3005
3006
3007
3008
3009
3010
3011
3012
3013
3014
3015
3016
3017
3018
3019
3020
3021
3022
3023
3024
3025
3026
3027
3028
3029
3030
3031
3032
3033
3034
3035
3036
3037
3038
3039
3040
3041
3042
3043
3044
3045
3046
3047
3048
3049
3050
3051
3052
3053
3054
3055
3056
3057
3058
3059
3060
3061
3062
3063
3064
3065
3066
3067
3068
3069
3070
3071
3072
3073
3074
3075
3076
3077
3078
3079
3080
3081
3082
3083
3084
3085
3086
3087
3088
3089
3090
3091
3092
3093
3094
3095
3096
3097
3098
3099
3100
3101
3102
3103
3104
3105
3106
3107
3108
3109
3110
3111
3112
3113
3114
3115
3116
3117
3118
3119
3120
3121
3122
3123
3124
3125
3126
3127
3128
3129
3130
3131
3132
3133
3134
3135
3136
3137
3138
3139
3140
3141
3142
3143
3144
3145
3146
3147
3148
3149
3150
3151
3152
3153
3154
3155
3156
3157
3158
3159
3160
3161
3162
3163
3164
3165
3166
3167
3168
3169
3170
3171
3172
3173
3174
3175
3176
3177
3178
3179
3180
3181
3182
3183
3184
3185
3186
3187
3188
3189
3190
3191
3192
3193
3194
3195
3196
3197
3198
3199
3200
3201
3202
3203
3204
3205
3206
3207
3208
3209
3210
3211
3212
3213
3214
3215
3216
3217
3218
3219
3220
3221
3222
3223
3224
3225
3226
3227
3228
3229
3230
3231
3232
3233
3234
3235
3236
3237
3238
3239
3240
3241
3242
3243
3244
3245
3246
3247
3248
3249
3250
3251
3252
3253
3254
3255
3256
3257
3258
3259
3260
3261
3262
3263
3264
3265
3266
3267
3268
3269
3270
3271
3272
3273
3274
3275
3276
3277
3278
3279
3280
3281
3282
3283
3284
3285
3286
3287
3288
3289
3290
3291
3292
3293
3294
3295
3296
3297
3298
3299
3300
3301
3302
3303
3304
3305
3306
3307
3308
3309
3310
3311
3312
3313
3314
3315
3316
3317
3318
3319
3320
3321
3322
3323
3324
3325
3326
3327
3328
3329
3330
3331
3332
3333
3334
3335
3336
3337
3338
3339
3340
3341
3342
3343
3344
3345
3346
3347
3348
3349
3350
3351
3352
3353
3354
3355
3356
3357
3358
3359
3360
3361
3362
3363
3364
3365
3366
3367
3368
3369
3370
3371
3372
3373
3374
3375
3376
3377
3378
3379
3380
3381
3382
3383
3384
3385
3386
3387
3388
3389
3390
3391
3392
3393
3394
3395
3396
3397
3398
3399
3400
3401
3402
3403
3404
3405
3406
3407
3408
3409
3410
3411
3412
3413
3414
3415
3416
3417
3418
3419
3420
3421
3422
3423
3424
3425
3426
3427
3428
3429
3430
3431
3432
3433
3434
3435
3436
3437
3438
3439
3440
3441
3442
3443
3444
3445
3446
3447
3448
3449
3450
3451
3452
3453
3454
3455
3456
3457
3458
3459
3460
3461
3462
3463
3464
3465
3466
3467
3468
3469
3470
3471
3472
3473
3474
3475
3476
3477
3478
3479
3480
3481
3482
3483
3484
3485
3486
3487
3488
3489
3490
3491
3492
3493
3494
3495
3496
3497
3498
3499
3500
3501
3502
3503
3504
3505
3506
3507
3508
3509
3510
3511
3512
3513
3514
3515
3516
3517
3518
3519
3520
3521
3522
3523
3524
3525
3526
3527
3528
3529
3530
3531
3532
3533
3534
3535
3536
3537
3538
3539
3540
3541
3542
3543
3544
3545
3546
3547
3548
3549
3550
3551
3552
3553
3554
3555
3556
3557
3558
3559
3560
3561
3562
3563
3564
3565
3566
3567
3568
3569
3570
3571
3572
3573
3574
3575
3576
3577
3578
3579
3580
3581
3582
3583
3584
3585
3586
3587
3588
3589
3590
3591
3592
3593
3594
3595
3596
3597
3598
3599
3599
3600
3601
3602
3603
3604
3605
3606
3607
3608
3609
3610
3611
3612
3613
3614
3615
3616
3617
3618
3619
3620
3621
3622
3623
3624
3625
3626
3627
3628
3629
3630
3631
3632
3633
3634
3635
3636
3637
3638
3639
3639
3640
3641
3642
3643
3644
3645
3646
3647
3648
3649
3649
3650
3651
3652
3653
3654
3655
3656
3657
3658
3659
3659
3660
3661
3662
3663
3664
3665
3666
3667
3668
3669
3669
3670
3671
3672
3673
3674
3675
3676
3677
3678
3679
3679
3680
3681
3682
3683
3684
3685
3686
3687
3688
3689
3689
3690
3691
3692
3693
3694
3695
3696
3697
3698
3699
3699
3700
3701
3702
3703
3704
3705
3706
3707
3708
3709
3709
3710
3711
3712
3713
3714
3715
3716
3717
3718
3719
3719
3720
3721
3722
3723
3724
3725
3726
3727
3728
3729
3729
3730
3731
3732
3733
3734
3735
3736
3737
3738
3739
3739
3740
3741
3742
3743
3744
3745
3746
3747
3748
3749
3749
3750
3751
3752
3753
3754
3755
3756
3757
3758
3759
3759
3760
3761
3762
3763
3764
3765
3766
3767
3768
3769
3769
3770
3771
3772
3773
3774
3775
3776
3777
3778
3779
3779
3780
3781
3782
3783
3784
3785
3786
3787
3788
3789
3789
3790
3791
3792
3793
3794
3795
3796
3797
3798
3799
3799
3800
3801
3802
3803
3804
3805
3806
3807
3808
3809
3809
3810
3811
3812
3813
3814
3815
3816
3817
3818
3819
3819
3820
3821
3822
3823
3824
3825
3826
3827
3828
3829
3829
3830
3831
3832
3833
3834
3835
3836
3837
3838
3839
3839
3840
3841
3842
3843
3844
3845
3846
3847
3848
3849
3849
3850
3851
3852
3853
3854
3855
3856
3857
3858
```

1779 be stored in the ROOT file that contains the DAQ data as can be seen from Figure A.3. Indeed,
 1780 another `TTree` called `RunParameters` as well as the 2 histograms `ID`, containing the scan number,
 1781 start and stop time stamps, and `Triggers`, containing the number of triggers requested by the shifter,
 1782 are available in the data files. Moreover, `ScanID` and `HV` are then used to construct the file name
 1783 thanks to the method `DataReader::GetFileName()`.

Chamber	RE2-2-NPD-BARC-8	RE2-2-CERN-106	RE2-3-NPD-BARC-9	RE4-2-CERN-165	RE4-2-KODEL-1-4	Max triggers
HV _{eff} 1	8600	8500	8600	8500	6500	
HV _{eff} 2	8700	8600	8700	8600	6600	
HV _{eff} 3	8800	8700	8800	8700	6700	
HV _{eff} 4	8900	8800	8900	8800	6800	
HV _{eff} 5	9000	8900	9000	8900	6900	
HV _{eff} 6	9100	9000	9100	9000	7000	
HV _{eff} 7	9200	9100	9200	9100	7100	
HV _{eff} 8	9300	9200	9300	9200	7200	
HV _{eff} 9	9400	9300	9400	9300	7300	
HV _{eff} 10	9500	9400	9500	9400	7400	

Figure A.6: WebDCS DAQ scan page. On this page, shifters need to choose the type of scan (Rate, Efficiency or Noise Reference scan), the gamma source configuration at the moment of data taking, the beam configuration, and the trigger mode. These information will be stored in the DAQ ROOT output. Are also given the minimal measurement time and waiting time after ramping up of the detectors is over before starting the data acquisition. Then, the list of HV points to scan and the number of triggers for each run of the scan are given in the table underneath.

1784 The rest of the information is written beforehand in the configuration file template, as explicated
 1785 in Source Code A.7, and contains the hardware addresses to the different VME modules in the
 1786 setup as well as settings for the TDCs. As the TDC settings available in the configuration file are not
 1787 supposed to be modified, an improvement would be to remove them from the configuration file and
 1788 to hardcode them inside of the DAQ code itself or to place them into a different INI file that would
 1789 host only the TDC settings to lower the probability for a bad manipulation of the configuration file
 1790 that can be modified from one of webDCS' menus.

1791

```
[General]
TdcS=4
ScanID=$scanid
HV=$HV
RunType=$runtype
MaxTriggers=$maxtriggers
Beam=$beam
[VMEInterface]
Type=V1718
BaseAddress=0xFF0000
Name=VmeInterface
[TDC0]
Type=V1190A
BaseAddress=0x00000000
Name=Tdc0
StatusA00-15=1
StatusA16-31=1
StatusB00-15=1
StatusB16-31=1
StatusC00-15=1
StatusC16-31=1
StatusD00-15=1
StatusD16-31=1
[TDC1]
Type=V1190A
BaseAddress=0x11110000
Name=Tdc1
StatusA00-15=1
StatusA16-31=1
StatusB00-15=1
StatusB16-31=1
StatusC00-15=1
StatusC16-31=1
StatusD00-15=1
StatusD16-31=1
[TDC2]
Type=V1190A
BaseAddress=0x22220000
Name=Tdc2
StatusA00-15=1
StatusA16-31=1
StatusB00-15=1
StatusB16-31=1
StatusC00-15=1
StatusC16-31=1
StatusD00-15=1
StatusD16-31=1
[TDC3]
Type=V1190A
BaseAddress=0x44440000
Name=Tdc3
StatusA00-15=1
StatusA16-31=1
StatusB00-15=1
StatusB16-31=1
StatusC00-15=1
StatusC16-31=1
StatusD00-15=1
StatusD16-31=1
[TDCSettings]
TriggerExtraSearchMargin=0
TriggerRejectMargin=0
TriggerTimeSubtraction=0b1
TdcDetectionMode=0b01
TdcResolution=0b10
TdcDeadTime=0b00
TdcHeadTrailer=0b1
TdcEventSize=0b1001
TdcTestMode=0b0
BLTMode=1
```

1792

Source Code A.7: INI configuration file template for 4 TDCs. In section [General], the number of TDCs is explicitated and information about the ongoing run is given. Then, there are sections for each and every VME modules. There buffer addresses are given and for the TDCs, the list of channels to enable is given. Finally, in section [TDCSettings], a part of the TDC settings are given.

1794 In order to retrieve the information of the configuration file, the object `IniFile` has been developed
 1795 to provide an INI parser, presented in Source Code A.8. It contains private methods returning a
 1796 boolean to check the type of line written in the file, whether a comment, a group header or a key line
 1797 (`IniFile::CheckIfComment()`, `IniFile::CheckIfGroup()` and `IniFile::CheckIfToken()`). The
 1798 key may sometimes be referred to as *token* in the source code. Moreover, the private element
 1799 `FileData` is a map of `const string` to `string` that allows to store the data contained inside the
 1800 configuration file via the public method `IniFile::GetFileData()` following the formatting (see
 1801 method `IniFile::Read()`):

```
1802
  1802     string group, token, value;
  1803     // Get the field values for the 3 strings.
  1803     // Then concatenate group and token together as a single string
  1803     // with a dot separation.
  1803     token = group + "." + token;
  1803     FileData[token] = value;
```

1804 More methods have been written to translate the different keys into the right variable format
 1805 when used by the DAQ. For example, to get a `float` value out of the configuration file data, knowing
 1806 the group and the key needed, the method `IniFile::floatType()` can be used. It takes 3 arguments
 1807 being the group name and key name (both `string`), and a default `float` value used as exception in
 1808 the case the expected combination of group and key cannot be found in the configuration file. This
 1809 default value is then used and the DAQ continues on working after sending an alert in the log file for
 1810 further debugging.

```

1811
typedef map< const string, string > IniFileData;

class IniFile{
    private:
        bool      CheckIfComment(string line);
        bool      CheckIfGroup(string line, string& group);
        bool      CheckIfToken(string line, string& key, string& value);
        string    FileName;
        IniFileData FileData;
        int       Error;

    public:
        IniFile();
        IniFile(string filename);
        virtual ~IniFile();

        // Basic file operations
        void      SetFileName(string filename);
        int       Read();
        int       Write();
        IniFileData GetFileData();

        // Data readout methods
        Data32   addressType (string groupname, string keyname, Data32
→      defaultvalue);
        long     intType     (string groupname, string keyname, long
→      defaultvalue);
        long long longType   (string groupname, string keyname, long long
→      defaultvalue );
        string   stringType  (string groupname, string keyname, string
→      defaultvalue );
        float    floatType   (string groupname, string keyname, float
→      defaultvalue );

        // Error methods
        string   GetErrorMsg();
};

1812

```

1813 *Source Code A.8: Description of C++ object `IniFile` used as a parser for INI file format.*

1814 A.5.3 WebDCS/DAQ intercommunication

1815 When shifters send instructions to the DAQ via the configuration file, it is the webDCS itself that
 1816 gives the start command to the DAQ and then the 2 softwares use inter-process communication
 1817 through file to synchronise themselves. This communication file is represented by the variable `const`
 1818 `string __runstatuspath`.

1819 On one side, the webDCS sends commands or status that are readout by the DAQ:

- 1820 ● INIT, status sent when launching a scan and read via function `CtrlRunStatus(...)`,
- 1821 ● START, command to start data taking and read via function `CheckSTART()`,
- 1822 ● STOP, command to stop data taking at the end of the scan and read via function `CheckSTOP()`,
 1823 and
- 1824 ● KILL, command to kill data taking sent by user and read via function `CheckKILL()`

1825 and on the other, the DAQ sends status that are controled by the webDCS:

- 1826 ● `DAQ_RDY`, sent with `SendDAQReady()` to signify that the DAQ is ready to receive commands
1827 from the webDCS,
- 1828 ● `RUNNING`, sent with `SendDAQRunning()` to signify that the DAQ is taking data,
- 1829 ● `DAQ_ERR`, sent with `SendDAQError()` to signify that the DAQ didn't receive the expected com-
1830 mand from the webDCS or that the launch command didn't have the right number of argu-
1831 ments,
- 1832 ● `RD_ERR`, sent when the DAQ wasn't able to read the communication file, and
- 1833 ● `WR_ERR`, sent when the DAQ wasn't able to write into the communication file.

1834 **A.5.4 Example of inter-process communication cycle**

1835 Under normal conditions, the webDCS and the DAQ processes exchange commands and status via
1836 the file hosted at the address `__runstatuspath`, as explained in subsection A.5.3. An example of
1837 cycle is given in Table A.1. In this example, the steps 3 to 5 are repeated as long as the webDCS tells
1838 the DAQ to take data. A data taking cycle is the equivalent as what is called a *Scan* in GIFT++ jargon,
1839 referring to a set a runs with several HV steps. Each repetition of steps 3 to 5 is then equivalent to a
1840 single *Run*.

1841

1842 At any moment during the data taking, for any reason, the shifter can decide that the data taking
1843 needs to be stopped before it reached the end of the scheduled cycle. Thus at any moment on the
1844 cycle, the content of the inter-process communication file will be changed to `KILL` and the DAQ will
1845 shut down right away. The DAQ checks for `KILL` signals every 5s after the TDCs configuration is
1846 over. So far, the function `CheckKILL()` has been used only inside of the data taking loop of method
1847 `DataReader::Run()` and thus, if the shifter decides to KILL the data taking during the TDC con-
1848 figuration phase or the HV ramping in between 2 HV steps, the DAQ will not be stopped smoothly
1849 and a *force kill* command will be sent to stop the DAQ process that is still awake on the computer.
1850 Improvements can be brought on this part of the software to make sure that the DAQ can safely
1851 shutdown at any moment.

1852

1853 **A.6 Software export**

1854 In section A.2 was discussed the fact that the DAQ as written in its last version is not a standalone
1855 software. It is possible to make it a standalone program that could be adapted to any VME setup
1856 using V1190A and V1718 modules by creating a GUI for the software or by printing the log mes-
1857 sages that are normally printed in the webDCS through the log file, directly into the terminal. This
1858 method was used by the DAQ up to version 3.0 moment where the webDCS was completed. Also, it
1859 is possible to check branches of DAQ v2.X to have example of communication through a terminal.

1860

1861 DAQ v2.X is nonetheless limited in it's possibilities and requires a lot of offline manual interven-
1862 tions from the users. Indeed, there is no communication of the software with the detectors' power
1863 supply system that would allow for a user a predefine a list of voltages to operate the detectors at

step	actions of webDCS	status of DAQ	__runstatuspath
1	launch DAQ ramp voltages ramping over wait for currents stabilization	readout of IniFile configuration of TDCs	INIT
2		configuration done send DAQ ready wait for START signal	DAQ_RDY
3	waiting time over send START		START
4	wait for run to end monitor DAQ run status	data taking ongoing check for KILL signal	RUNNING
5		run over send DAQ_RDY wait for next DCS signal	DAQ_RDY
6	ramp voltages ramping over wait for currents stabilization		DAQ_RDY
3	waiting time over send START		START
4	wait for run to end monitor DAQ run status	update IniFile information data taking ongoing check for KILL signal	RUNNING
5		run over send DAQ_RDY wait for next DCS signal	DAQ_RDY
7	send command STOP	DAQ shuts down	STOP

Table A.1: Inter-process communication cycles in between the webDCS and the DAQ through file string signals.

1864 and loop over to take data without any further manual intervention. In v2.X, the data is taken for a
1865 single detector setting and at the end of each run, the softwares asks the user if he intends on taking
1866 more runs. If so, the software invites the user to set the operating voltages accordingly to what is
1867 necessary and to manual update the configuration file in consequence. This working mode can be a
1868 very first approach before an evolution and has been successfully used by colleagues from different
1869 collaborations.

1870
1871 For a more robust operation, it is recommended to develop a GUI or a web application to inter-
1872 face the DAQ. Moreover, to limit the amount of manual interventions, and thus the probability to
1873 make mistakes, it is also recommended to add an extra feature into the DAQ by installing the HV
1874 Wrapper library provided by CAEN of which an example of use in a similar DAQ software devel-
1875 opped by a master student of UGent, and called TinyDAQ, is provided on UGent's github. Then, this
1876 HV Wrapper will help you communicating with and give instructions to a CAEN HV powered crate
1877 and can be added into the DAQ at the same level where the communication with the user was made
1878 in DAQ v2.X. In case you are using another kind of power system for your detectors, it is stringly
1879 adviced to use HV modules or crates that can be remotely controled via a using C++ libraries.
1880

B

1881

1882

Details on the offline analysis package

1883 The data collected in GIF++ thanks to the DAQ described in Appendix A is difficult to interpret by
1884 a human user that doesn't have a clear idea of the raw data architecture of the ROOT data files. In
1885 order to render the data human readable, a C++ offline analysis tool was designed to provide users
1886 with detector by detector histograms that give a clear overview of the parameters monitored during
1887 the data acquisition [62]. In this appendix, details about this software in the context of GIF++, as of
1888 how the software was written and how it functions will be given.

1889 **B.1 GIF++ Offline Analysis file tree**

1890 GIF++ Offline Analysis source code is fully available on github at https://github.com/afagot/GIF_OfflineAnalysis. The software requires ROOT as non-optionnal dependency
1891 as it takes ROOT files in input and write an output ROOT file containing histograms. To compile the
1892 GIF++ Offline Analysis project is compiled with cmake. To compile, first a build/ directory must
1893 be created to compile from there:

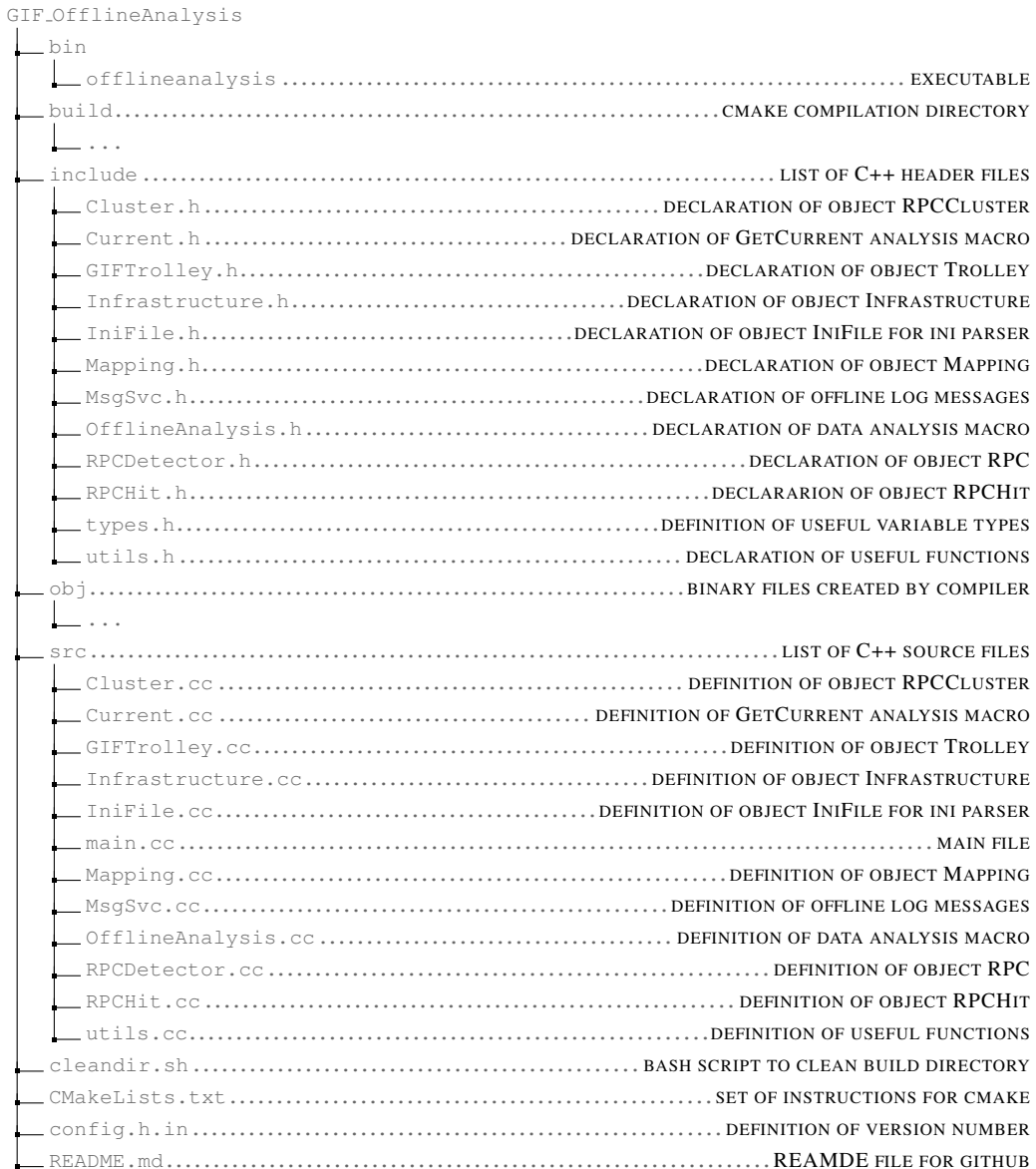
```
1895     mkdir build
1896     cd build
1897     cmake ..
1898     make
1899     make install
```

1897 To clean the directory and create a new build directory, the bash script cleandir.sh can be used:

```
1898
1899     ./cleandir.sh
```

1900 The source code tree is provided below along with comments to give an overview of the files' con-
1901 tent. The different objects created for this project (`Infrastructure`, `Trolley`, `RPC`, `Mapping`, `RPCHit`,
1902 `RPCCluster` and `Inifile`) will be described in details in the following sections.

1903



1904

B.2 Usage of the Offline Analysis

1905

In order to use the Offline Analysis tool, it is necessary to know the Scan number and the HV Step of the run that needs to be analysed. This information needs to be written in the following format:

1907

1908

```
Scan00XXXX_HVY
```

1909

where XXXX is the scan ID and Y is the high voltage step (in case of a high voltage scan, data will be taken for several HV steps). This format corresponds to the base name of data files in the database

1910

1911 of the GIF++ webDCS. Usually, the offline analysis tool is automatically called by the webDCS at
 1912 the end of data taking or by a user from the webDCS panel if an update of the tool was brought.
 1913 Nonetheless, an expert can locally launch the analysis for tests on the GIF++ computer, or a user can
 1914 get the code on its local machine from github and download data from the webDCS for its own anal-
 1915 ysis. To launch the code, the following command can be used from the `GIF_OfflineAnalysis` folder:

```
1916
1917 bin/offlineanalysis /path/to/Scan00XXXX_HVY
```

1918 where, `/path/to/Scan00XXXX_HVY` refers to the local data files. Then, the offline tool will by itself
 1919 take care of finding all available ROOT data files present in the folder, as listed below:

- 1920 • `Scan00XXXX_HVY_DAQ.root` containing the TDC data as described in Appendix ?? (events, hit
 1921 and timestamp lists), and
- 1922 • `Scan00XXXX_HVY_CAEN.root` containing the CAEN mainframe data recorded by the monitor-
 1923 ing tool webDCS during data taking (HVs and currents of every HV channels). This file is
 1924 created independently of the DAQ.

1925 **B.2.1 Output of the offline tool**

1926 **B.2.1.1 ROOT file**

1927 The analysis gives in output ROOT datafiles that are saved into the data folder and called using the
 1928 naming convention `Scan00XXXX_HVY_Offline.root`. Inside those, a list of `TH1` histograms can be
 1929 found. Its size will vary as a function of the number of detectors in the setup as each set of histograms
 1930 is produced detector by detector. For each partition of each chamber, can be found:

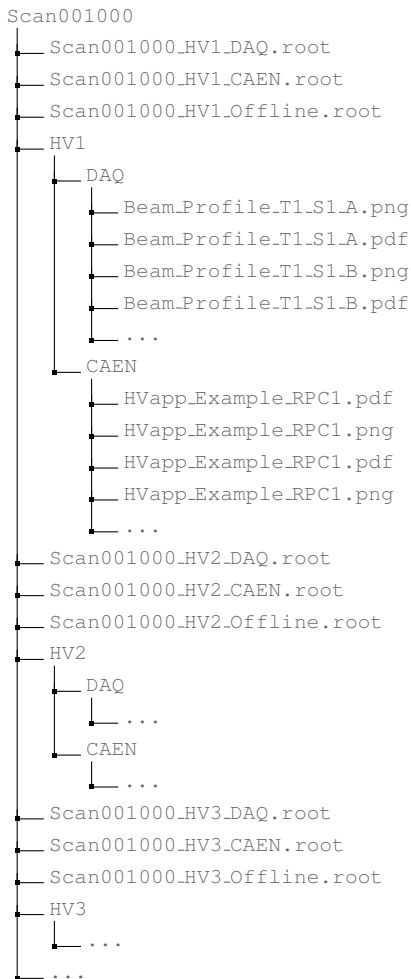
- 1931 • `Time_Profile_Tt_Sc_p` shows the time profile of all recorded events (number of events per
 1932 time bin),
- 1933 • `Hit_Profile_Tt_Sc_p` shows the hit profile of all recorded events (number of events per chan-
 1934 nel),
- 1935 • `Hit_Multiplicity_Tt_Sc_p` shows the hit multiplicity (number of hits per event) of all recorded
 1936 events (number of occurrences per multiplicity bin),
- 1937 • `Strip_Mean_Noise_Tt_Sc_p` shows noise/gamma rate per unit area for each strip in a se-
 1938 lected time range. After filters are applied on `Time_Profile_Tt_Sc_p`, the filtered version
 1939 of `Hit_Profile_Tt_Sc_p` is normalised to the total integrated time and active detection area
 1940 of a single channel,
- 1941 • `Strip_Activity_Tt_Sc_p` shows noise/gamma activity for each strip (normalised version of
 1942 previous histogram - strip activity = strip rate / average partition rate),
- 1943 • `Strip_Homogeneity_Tt_Sc_p` shows the *homogeneity* of a given partition ($\text{homogeneity} = \exp(-\text{strip rates standard deviation(strip rates in partition/average partition rate)})$),
- 1945 • `mask_Strip_Mean_Noise_Tt_Sc_p` shows noise/gamma rate per unit area for each masked
 1946 strip in a selected time range. Offline, the user can control the noise/gamma rate and decide to
 1947 mask the strips that are judged to be noisy or dead. This is done via the *Masking Tool* provided
 1948 by the webDCS,

- 1949 ● `mask_Strip_Activity_Tt_Sc_p` shows noise/gamma activity per unit area for each masked
1950 strip with respect to the average rate of active strips,
- 1951 ● `NoiseCSize_H_Tt_Sc_p` shows noise/gamma cluster size, a cluster being constructed out of
1952 adjacent strips giving a signal at the *same time* (hits within a time window of 25 ns),
- 1953 ● `NoiseCMult_H_Tt_Sc_p` shows noise/gamma cluster multiplicity (number of reconstructed
1954 clusters per event),
- 1955 ● `Chip_Mean_Noise_Tt_Sc_p` shows the same information than `Strip_Mean_Noise_Tt_Scp` us-
1956 ing a different binning (1 chip corresponds to 8 strips),
- 1957 ● `Chip_Activity_Tt_Sc_p` shows the same information than `Strip_Activity_Tt_Scp` using
1958 chip binning,
- 1959 ● `Chip_Homogeneity_Tt_Sc_p` shows the homogeneity of a given partition using chip binning,
- 1960 ● `Beam_Profile_Tt_Sc_p` shows the estimated beam profile when taking efficiency scan. This
1961 is obtained by filtering `Time_Profile_Tt_Sc_p` to only consider the muon peak where the
1962 noise/gamma background has been subtracted. The resulting hit profile corresponds to the
1963 beam profile on the detector channels,
- 1964 ● `L0_Efficiency_Tt_Sc_p` shows the level 0 efficiency that was estimated **without** muon track-
1965 ing,
- 1966 ● `MuonCSize_H_Tt_Sc_p` shows the level 0 muon cluster size that was estimated **without** muon
1967 tracking, and
- 1968 ● `MuonCMult_H_Tt_Sc_p` shows the level 0 muon cluster multiplicity that was estimated **without**
1969 muon tracking.

1970 In the histogram labels, t stands for the trolley number (1 or 3), c for the chamber slot label in
1971 trolley t and p for the partition label (A, B, C or D depending on the chamber layout) as explained
1972 in Chapter ??.

1973 In the context of GIF++, an extra script called by the webDCS is called to extract the histograms
1974 from the ROOT files. The histograms are then stored in PNG and PDF formats into the correspond-
1975 ing folder (a single folder per HV step, so per ROOT file). the goal is to then display the histograms
1976 on the Data Quality Monitoring (DQM) page of the webDCS in order for the users to control the
1977 quality of the data taking at the end of data taking. An example of histogram organisation is given
1978 below:

1980



1981 Here can put some screens from the webDCS to show the DQM and the plots available to users.

1982

1983 B.2.1.2 CSV files

1984 Moreover, up to 3 CSV files can be created depending on which ones of the 3 input files were in the

1985 data folder:

- 1986 • Offline-Corrupted.csv , is used to keep track of the amount of data that was corrupted and**
- 1987 removed from old data format files that don't contain any data quality flag.**
- 1988 • Offline-Current.csv , contains the summary of the currents and voltages applied on each**
- 1989 RPC HV channel.**
- 1990 • Offline-L0-EffC1.csv , is used to write the efficiencies, cluster size and cluster multiplicity**
- 1991 of efficiency runs. Note that L0 refers here to *Level 0* and means that the results of efficiency and**
- 1992 clusterization are a first approximation calculated without performing any muon tracking in**

1993 between the different detectors. This offline tool provides the user with a preliminar calculation
 1994 of the efficiency and of the muon event parameters. Another analysis software especially
 1995 dedicated to muon tracking is called on selected data to retrieve the results of efficiency and
 1996 muon clusterization using a tracking algorithm to discriminate noise or gamma from muons
 1997 as muons are the only particles that pass through the full setup, leaving hits than can be used
 1998 to reconstruct their tracks.

- 1999 ● `Offline-Rate.csv`, is used to write the noise or gamma rates measured in the detector readout
 2000 partitions.

2001 Note that these 4 CSV files are created along with their *headers* (`Offline-[...]-Header.csv`
 2002 containing the names of each data columns) and are automatically merged together when the offline
 2003 analysis tool is called from the webDCS, contrary to the case where the tool is runned locally from
 2004 the terminal as the merging bash script is then not called. Thus, the resulting files, used to make
 2005 official plots, are:

- 2006 ● `Corrupted.csv`,
 2007 ● `Current.csv`,
 2008 ● `L0-EffCl.csv`.
 2009 ● `Rate.csv`.

2010 **B.3 Analysis inputs and information handling**

2011 The usage of the Offline Analysis tool as well as its output have been presented in the previous section.
 2012 It is now important to dig further and start looking at the source code and the inputs necessary
 2013 for the tool to work. Indeed, other than the raw ROOT data files that are analysed, more information
 2014 needs to be imported inside of the program to perform the analysis such as the description of the
 2015 setup inside of GIFT++ at the time of data taking (number of trolleys, of RPCs, dimensions of the
 2016 detectors, etc...) or the mapping that links the TDC channels to the coresponding RPC channels in
 2017 order to translate the TDC information into human readable data. 2 files are used to transmit all this
 2018 information:
 2019

- 2020 ● `Dimensions.ini`, that provides the necessary setup and RPC information, and
 2021 ● `ChannelsMapping.csv`, that gives the link between the TDC and RPC channels as well as the
 2022 *mask* for each channel (masked or not?).

2023 **B.3.1 Dimensions file and InFile parser**

2024 This input file, present in every data folder, allows the analysis tool to know of the number of active
 2025 trolleys, the number of active RPCs in those trolleys, and the details about each RPCs such as
 2026 the number of RPC gaps, the number of pseudo-rapidity partitions (for CMS-like prototypes), the
 2027 number of strips per partion or the dimensions. To do so, there are 3 types of groups in the INI file
 2028 architecture. A first general group, appearing only once at the head of the document, gives information
 2029 about the number of active trolleys as well as their IDs, as presented in Source Code B.1. For

2030 each active trolley, a group similar to Source Code B.2 can be found containing information about
 2031 the number of active detectors in the trolley and their IDs. Each trolley group as a `Tt` name format,
 2032 where `t` is the trolley ID. Finally, for each detector stored in slots of an active trolley, there is a group
 2033 providing information about their names and dimensions, as shown in Source Code B.3. Each slot
 2034 group as a `TtSs` name format, where `s` is the slot ID of trolley `t` where the active RPC is hosted.

```
2035 [General]
2036 nTrolleys=2
  TrolleysID=13
```

2037 *Source Code B.1: Example of `[General]` group as might be found in `Dimensions.ini`. In Gif++, only 2 trolleys are available to hold RPCs and place them inside of the bunker for irradiation. The IDs of the trolleys are written in a single string as "13" and then read character by character by the program.*

```
2038 [T1]
  nSlots=4
  SlotsID=1234
```

2039 *Source Code B.2: Example of trolley group as might be found in `Dimensions.ini`. In this example, the file tells that there are 4 detectors placed in the holding slots of the trolley `T1` and that their IDs, written as a single string variable, are 1, 2, 3 and 4.*

```
2040 [T1S1]
  Name=RE2-2-NPD-BARC-8
  Partitions=3
  Gaps=3
  Gap1=BOT
  Gap2=TN
  Gap3=TW
  AreaGap1=11694.25
  AreaGap2=6432
  AreaGap3=4582.82
  Strips=32
  ActiveArea-A=157.8
  ActiveArea-B=121.69
  ActiveArea-C=93.03
```

2041 *Source Code B.3: Example of slot group as might be found in `Dimensions.ini`. In this example, the file provides information about a detector named `RE2-2-NPD-BARC-8`, having 3 pseudo-rapidity readout partitions and stored in slot `S1` of trolley `T1`. This is a CMS RE2-2 type of detector. This information will then be used for example to compute the rate per unit area calculation.*

2042 This information is readout and stored in a C++ object called `IniFile`, that parses the information
 2043 in the INI input file and stores it into a local buffer for later use. This INI parser is the exact same
 2044 one that was previously developed for the Gif++ DAQ and described in Appendix A.5.2.

2045 B.3.2 TDC to RPC link file and Mapping

2046 The same way the INI dimension file information is stored using `map`, the channel mapping and mask
 2047 information is stored and accessed through `map`. First of all, the mapping CSV file is organised into
 2048 3 columns separated by tabulations (and not by commas, as expected for CSV files as it is easier using
 2049 streams to read tab or space separated data using C++):

2050

2051 RPC_channel TDC_channel mask

2052 using as formatting for each field:

2053
2054 TSCCC TCCC M

2055 TSCCC is a 5-digit integer where T is the trolley ID, s the slot ID in which the RPC is held insite
2056 the trolley T and ccc is the RPC channel number, or *strip* number, that can take values up to
2057 3-digits depending on the detector,

2058 TCCC is a 4 digit integer where T is the TDC ID, ccc is the TDC channel number that can take values
2059 in between 0 and 127, and

2060 M is a 1-digit integer indicating if the channel should be considered ($M = 1$) or discarded ($M = 0$)
2061 during analysis.

2062 This mapping and masking information is readout and stored thanks to the object `Mapping`, pre-
2063 sented in Source Code B.4. Similarly to `IniFile` objects, this class has private methods. The first
2064 one, `Mapping::CheckIfNewLine()` is used to find the newline character '`\n`' or return character
2065 '`\r`' (depending on which kind of operating system interacted with the file). This is used for the
2066 simple reason that the masking information has been introduced only during the year 2017 but the
2067 channel mapping files exist since 2015 and the very beginning of data taking at GIF++. This means
2068 that in the older data folders, before the upgrade, the channel mapping file only had 2 columns, the
2069 RPC channel and the TDC channel. For compatibility reasons, this method helps controling the
2070 character following the readout of the 2 first fields of a line. In case any end of line character is
2071 found, no mask information is present in the file and the default $M = 1$ is used. On the contrary, if
2072 the next character was a tabulation or a space, the mask information is present.

2073 Once the 3 fields have been readout, the second private method `Mapping::CheckIfTDCCh()` is
2074 used to control that the TDC channel is an existing TDC channel. Finally, the information is stored
2075 into 3 different maps (`Link`, `ReverseLink` and `Mask`) thanks to the public method `Mapping::Read()`.
2076 `Link` allows to get the RPC channel by knowing the TDC channel while `ReverseLink` does the op-
2077 posite by returning the TDC channel by knowing the RPC channel. Finally, `Mask` returns the mask
2078 associated to a given RPC channel.

```

2079 typedef map<Uint,Uint> MappingData;

2080 class Mapping {
2081     private:
2082         bool          CheckIfNewLine(char next);
2083         bool          CheckIfTDCCh(Uint channel);
2084         string        FileName;
2085         MappingData  Link;
2086         MappingData  ReverseLink;
2087         MappingData  Mask;
2088         int           Error;
2089
2090     public:
2091         Mapping();
2092         Mapping(string baseName);
2093         ~Mapping();

2094         void SetFileName(const string filename);
2095         int Read();
2096         Uint GetLink(Uint tdcchannel);
2097         Uint GetReverse(Uint rpcchannel);
2098         Uint GetMask(Uint rpcchannel);
2099     };

```

2081 *Source Code B.4: Description of C++ object Mapping used as a parser for the channel mapping and mask file.*

2082 B.4 Description of GIF++ setup within the Offline Analysis tool

2083 In the previous section, the tool input files have been discussed. The dimension file information is
 2084 stored in a map hosted by the `IniFile` object. But this information is then used to create a series of
 2085 new objects that helps defining the GIF++ infrastructure directly into the Offline Analysis. Indeed,
 2086 from the `RPC`, to the more general `Infrastructure`, every element of the GIF++ infrastrucutre is
 2087 recreated for each data analysis based on the information provided in input. All this information
 2088 about the infrastructure will be used to assign each hit signal to a specific strip channel of a specific
 2089 detector, and having a specific active area. This way, rate per unit area calculation is possible.
 2090

2091 B.4.1 RPC objects

2092 `RPC` objects have been developped to represent physical active detectors in GIF++ at the moment
 2093 of data taking. Thus, there are as many `RPC` objects created during the analysis than there were
 2094 active `RPC`s tested during a run. Each `RPC` hosts the information present in the corresponding INI
 2095 slot group, as shown in B.3, and organises it using a similar architecture. This can be seen from
 2096 *Source Code B.5*.

2097 To make the object more compact, the lists of gap labels, of gap active areas and strip active
 2098 areas are stored into `vector` dynamical containers. `RPC` objects are always contructed thanks to the
 2099 dimension file information stored into the `IniFILE` and their ID, using the format `TtSs`. Using the
 2100 `RPC` ID, the constructor calls the methods of `IniFILE` to initialise the `RPC`. The other constructors
 2101 are not used but exist in case of need. Finally, some getters have been written to access the different
 2102 private parameters storing the detector information.

```

2103
class RPC{
    private:
        string      name;           //RPC name as in webDCS database
        Uint        nGaps;          //Number of gaps in the RPC
        Uint        nPartitions;    //Number of partitions in the RPC
        Uint        nStrips;         //Number of strips per partition
        vector<string> gaps;       //List of gap labels (BOT, TOP, etc...)
        vector<float>  gapGeo;        //List of gap active areas
        vector<float>  stripGeo;      //List of strip active areas

    public:
        RPC();
        RPC(string ID, IniFile* geofile);
        RPC(const RPC& other);
        ~RPC();
        RPC& operator=(const RPC& other);

        string GetName();
        Uint GetNGaps();
        Uint GetNPartitions();
        Uint GetNStrips();
        string GetGap(Uint g);
        float GetGapGeo(Uint g);
        float GetStripGeo(Uint p);
};

2104

```

2105 *Source Code B.5: Description of C++ objects RPC that describe each active detectors used during data taking.*

2106 B.4.2 Trolley objects

2107 Trolley objects have been developped to represent physical active trolleys in GIFT++ at the moment
 2108 of data taking. Thus, there are as many trolley objects created during the analysis than there were
 2109 active trolleys hosting tested RPCs during a run. Each Trolley hosts the information present in the
 2110 corresponding INI trolley group, as shown in B.2, and organises it using a similar architecture. In
 2111 addition to the information hosted in the INI file, these object have a dynamical container of RPC
 2112 objects, representing the active detectors the active trolley was hosting at the time of data taking.
 2113 This can been seen from Source Code B.6.

2114 Trolley objects are always contructed thanks to the dimension file information stored into the
 2115 IniFILE and their ID, using the format Tt. Using the Trolley ID, the constructor calls the methods
 2116 of IniFILE to initialise the Trolley. Retrieving the information of the RPC IDs via SlotsID, a new
 2117 RPC is constructed and added to the container RPCs for each character in the ID string. The other
 2118 constructors are not used but exist in case of need. Finally, some getters have been written to access
 2119 the different private parameters storing the trolley and detectors information.

```

2120
class Trolley{
    private:
        Uint          nSlots; //Number of active RPCs in the considered trolley
        string        SlotsID; //Active RPC IDs written into a string
        vector<RPC*> RPCs;   //List of active RPCs

    public:
        //Constructors, destructor and operator =
        Trolley();
        Trolley(string ID, IniFile* geofile);
        Trolley(const Trolley& other);
        ~Trolley();
        Trolley& operator=(const Trolley& other);

        //Get GIFTrolley members
        Uint  GetNSlots();
        string GetSlotsID();
        Uint   GetSlotID(Uint s);

        //Manage RPC list
        RPC*  GetRPC(Uint r);
        void  DeleteRPC(Uint r);

        //Methods to get members of RPC objects stored in RPCs
        string GetName(Uint r);
        Uint   GetNGaps(Uint r);
        Uint   GetNPartitions(Uint r);
        Uint   GetNStrips(Uint r);
        string GetGap(Uint r, Uint g);
        float  GetGapGeo(Uint r, Uint g);
        float  GetStripGeo(Uint r, Uint p);
    };

```

Source Code B.6: Description of C++ objects `Trolley` that describe each active trolley used during data taking.

2123 B.4.3 Infrastructure object

2124 The `Infrastructure` object has been developped to represent the GIFT++ bunker area dedicated to
 2125 CMS RPC experiments. With this very specific object, all the information about the CMS RPC
 2126 setup within GIFT++ at the moment of data taking is stored. It hosts the information present in the
 2127 corresponding INI general group, as shown in B.1, and organises it using a similar architecture. In
 2128 addition to the information hosted in the INI file, this object have a dynamical container of `Trolley`
 2129 objects, representing the active tolleys in GIFT++ area. This can be seen from Source Code B.7.

2130 The `Infrastructure` object is always contructed thanks to the dimension file information stored
 2131 into the `IniFILE`. Retrieving the information of the trolley IDs via `TrolleysID`, a new `Trolley` is
 2132 constructed and added to the container `Trolleys` for each character in the ID `string`. By extension,
 2133 it is easy to understand that the process described in Section B.4.2 for the construction of RPCs
 2134 takes place when a trolley is constructed. The other constructors are not used but exist in case of
 2135 need. Finally, some getters have been written to access the different private parameters storing the
 2136 infrastructure, tolleys and detectors information.

2137

```

class Infrastructure {
    private:
        Uint             nTrolleys;   //Number of active Trolleys in the run
        string          TrolleysID;  //Active trolley IDs written into a string
        vector<Trolley*> Trolleys;  //List of active Trolleys (struct)

    public:
        //Constructors and destructor
        Infrastructure();
        Infrastructure(IniFile* geofile);
        Infrastructure(const Infrastructure& other);
        ~Infrastructure();
        Infrastructure& operator=(const Infrastructure& other);

        //Get Infrastructure members
        Uint  GetNTrolleys();
        string GetTrolleysID();
        Uint   GetTrolleyID(Uint t);

    2138   //Manage Trolleys
        Trolley* GetTrolley(Uint t);
        void     DeleteTrolley(Uint t);

        //Methods to get members of GIFTrolley objects stored in Trolleys
        Uint  GetNSlots(Uint t);
        string GetSlotsID(Uint t);
        Uint   GetSlotID(Uint t, Uint s);
        RPC*  GetRPC(Uint t, Uint r);

        //Methods to get members of RPC objects stored in RPCs
        string GetName(Uint t, Uint r);
        Uint   GetNGaps(Uint t, Uint r);
        Uint   GetNPartitions(Uint t, Uint r);
        Uint   GetNStrips(Uint t, Uint r);
        string GetGap(Uint t, Uint r, Uint g);
        float  GetGapGeo(Uint t, Uint r, Uint g);
        float  GetStripGeo(Uint t, Uint r, Uint p);
    };

```

2139

Source Code B.7: Description of C++ object Infrastructure that contains the full information about CMS RPC experiment in GIF++.

2140

B.5 Handeling of data

2141

As discussed in Appendix A.4.2, the raw data as a `TTree` architecture where every entry is related to a trigger signal provided by a muon or a random pulse, whether the goal of the data taking was to measure the performance of the detector or the noise/gamma background respectively. Each of these entries, referred also as events, contain a more or less full list of hits in the TDC channels to which the detectors are connected. To this list of hits corresponds a list of time stamps, marking the arrival of the hits within the TDC channel.

2147

The infrastructure of the CMS RPC experiment within `GIF++` being defined, combining the information about the raw data with the information provided by both the mapping/mask file and the dimension file allows to build new physical objects that will help in computing efficiency or rates.

2150 B.5.1 RPC hits

2151 The raw data stored in the ROOT file as output of the GIFT++ DAQ, is readout by the analysis tool
 2152 using the structure `RAWData` presented in Source Code B.9 that differs from the structure presented
 2153 in Appendix A.4.2 as it is not meant to hold all of the data contained in the ROOT file. In this sense,
 2154 this structure is in the case of the offline analysis tool not a dynamical object and will only be storing
 2155 a single event contained in a single entry of the `TTree`.

```
2156
2157 class RPCHit {
2158     private:
2159         Uint Channel;      //RPC channel according to mapping (5 digits)
2160         Uint Trolley;      //0, 1 or 3 (1st digit of the RPC channel)
2161         Uint Station;      //Slot where is held the RPC in Trolley (2nd digit)
2162         Uint Strip;        //Physical RPC strip where the hit occurred (last 3
2163             digits)
2164         Uint Partition;    //Readout partition along eta segmentation
2165         float TimeStamp;   //Time stamp of the arrival in TDC
2166
2167     public:
2168         //Constructors, destructor & operator =
2169         RPCHit();
2170         RPCHit(Uint channel, float time, Infrastructure* Infra);
2171         RPCHit(const RPCHit& other);
2172         ~RPCHit();
2173         RPCHit& operator=(const RPCHit& other);
2174
2175         //Get RPCHit members
2176         Uint GetChannel();
2177         Uint GetTrolley();
2178         Uint GetStation();
2179         Uint GetStrip();
2180         Uint GetPartition();
2181         float GetTime();
2182     };
2183
2184     typedef vector<RPCHit> HitList;
2185     typedef struct GIFHitList { HitList rpc[NTROLLEYS][NSLOTS][NPARTITIONS]; } →
2186         GIFHitList;
2187
2188     bool SortHitbyStrip(RPCHit h1, RPCHit h2);
2189     bool SortHitbyTime(RPCHit h1, RPCHit h2);
2190 }
```

2158 *Source Code B.8: Description of C++ object RPCHit.*

```
2159
2160     struct RAWData{
2161         int iEvent;          //Event i
2162         int TDCNHits;       //Number of hits in event i
2163         int QFlag;           //Quality flag list (1 flag digit per TDC)
2164         vector<Uint> *TDCCh; //List of channels giving hits per event
2165         vector<float> *TDCTS; //List of the corresponding time stamps
2166     };
2167 }
```

2160 *Source Code B.9: Description of C++ structure RAWData.*

2161 Each member of the structure is then linked to the corresponding branch of the ROOT data tree,
 2162 as shown in the example of Source Code B.10, and using the method `GetEntry(int i)` of the ROOT
 2163 class `TTree` will update the state of the members of `RAWData`.

```

2164 TTree* dataTree = (TTree*)dataFile.Get("RAWData");
2165 RAWData data;
2166
2167 dataTree->SetBranchAddress("EventNumber", &data.iEvent);
2168 dataTree->SetBranchAddress("number_of_hits", &data.TDCNHits);
2169 dataTree->SetBranchAddress("Quality_flag", &data.QFlag);
2170 dataTree->SetBranchAddress("TDC_channel", &data.TDCCh);
2171 dataTree->SetBranchAddress("TDC_TimeStamp", &data.TDCTS);

```

2166 *Source Code B.10: Example of link in between RAWData and TTree.*

2167 The data is then analysed entry by entry and to each element of the TDC channel list, a `RPCHit` is
 2168 constructed by linking each TDC channel to the corresponding RPC channel thanks to the `Mapping`
 2169 object. The information carried by the RPC channel format allows to easily retrieve the trolley and
 2170 slot from which the hit was recorded (see section B.3.2). Using these 2 values, the readout partition
 2171 can be found by knowing the strip channel and comparing it with the number of partitions and strips
 2172 per partition stored into the `Infrastructure` object.

2173 Thus `RPCHit` objects are then stored into 3D dynamical list called `GIFHitList` (Source Code B.9)
 2174 where the 3 dimensions refer to the 3 layers of the readout in `GIF++` : in the bunker there are *trolleys*
 2175 (τ) holding detectors in *slots* (s) and each detector readout is divided into 1 or more pseudo-rapidity
 2176 *partitions* (p). Using these 3 information allows to assign an address to each readout partition and
 2177 this address will point to a specific hit list.

2178

2179 **B.5.2 Clusters of hits**

2180 All the hits contained in the ROOT file have been sorted into the different hit lists through the
 2181 `GIFHitList`. At this point, it is possible to start looking for clusters. A cluster is a group of adjacent
 2182 strips getting hits within a time window of 25 ns. These strips are then assumed to be part of the same
 2183 physical avalanche signal generated by a muon passing through the chamber or by the interaction of
 2184 a gamma stopping into the electrodes of the RPCs.

2185 To keep the cluster information, `RPCCluster` objects have been defined as shown in Source
 2186 Code B.11. Using the information of each individual `RPCHit` taken out of the hit list, it stores
 2187 the cluster size (number of adjacent strips composing the cluster), the first and last hit, the center for
 2188 spatial reconstruction and finally the start and stop time stamps as well as te time spread in between
 2189 the first and last hit.

```

2190
class RPCCluster{
    private:
        Uint ClusterSize; //Size of cluster #ID
        Uint FirstStrip; //First strip of cluster #ID
        Uint LastStrip; //Last strip of cluster #ID
        float Center; //Center of cluster #ID ((first+last)/2)
        float StartStamp; //Time stamp of the earliest hit of cluster #ID
        float StopStamp; //Time stamp of the latest hit of cluster #ID
        float TimeSpread; //Time difference between earliest and latest hits
                           //of cluster #ID
    public:
        //Constructors, destructor & operator =
        RPCCluster();
        RPCCluster(HitList List, Uint cID, Uint cSize, Uint first, Uint firstID);
        RPCCluster(const RPCCluster& other);
        ~RPCCluster();
        RPCCluster& operator=(const RPCCluster& other);

        //Get Cluster members
        Uint GetID();
        Uint GetSize();
        Uint GetFirstStrip();
        Uint GetLastStrip();
        float GetCenter();
        float GetStart();
        float GetStop();
        float GetSpread();
    };

typedef vector<RPCCluster> ClusterList;

//Other functions to build cluster lists out of hit lists
void BuildClusters(HitList &cluster, ClusterList &clusterList);
void Clusterization(HitList &hits, TH1 *hcSize, TH1 *hcMult);

```

2192 *Source Code B.11: Description of C++ object Cluster.*

2193 To investigate the hit list of a given detector partition, the function `Clusterization()` defined
 2194 in `include/Cluster.h` needs the hits in the list to be time sorted. This is achieved by calling func-
 2195 tion `sort()` of library `<algorithm>` using the comparator `SortHitbyTime(RPCHit h1, RPCHit h2)`
 2196 defined in `include/RPCHit.h` that returns `true` if the time stamp of hit `h1` is lower than that of `h2`.
 2197 A first isolation of strips is made only based on time information. All the hits within the 25 ns win-
 2198 dow are taken separately from the rest. Then, this sub-list of hits is sorted this time by ascending
 2199 strip number, using this time the comparator `SortHitbyStrip(RPCHit h1, RPCHit h2)`. Finally, the
 2200 groups of adjacent strips are used to construct `RPCCluster` objects that are then stored in a temporary
 2201 list of clusters that is at the end of the process used to know how many clusters were reconstructed
 2202 and to fill their sizes into an histogram that will allows to know the mean size of muon or gamma
 2203 clusters.

2204

2205 **B.6 DAQ data Analysis**

2206 All the ingredients to analyse GIF++ data have been defined. This section will focus on the different
 2207 part of the analysis performed on the data, from determining the type of data the tool is dealing with

2208 to calculating the rate in each detector or reconstructing muon or gamma clusters.

2209 B.6.1 Determination of the run type

2210 In GIF++, both the performance of the detectors in detecting muons in an irradiated environment and
 2211 the gamma background can be independantly measured. These corresponds to different run types
 2212 and thus, to different TDC settings giving different data to look at.

2213

2214 In the case of performance measurements, the trigger for data taking is provided by the coïncidence
 2215 of several scintillators when muons from the beam passing through the area are detected. Data
 2216 is collected in a 600 ns wide window around the arrival of muons in the RPCs. The expected time
 2217 distribution of hits is shown in Figure B.1a. The muon peak is clearly visible in the center of the
 2218 distribution and is to be extracted from the gamma background that composes the flat part of the
 2219 distribution.

2220 On the other hand, gamma background or noise measurements are focussed on the non muon
 2221 related physics and the trigger needs to be independant from the muons to give a good measurement
 2222 of the gamma/noise distribution as seen by the detectors. The trigger is then provided by a pulse
 2223 generator at a frequency of 300 Hz whose pulse is not likely to be on time with a muon. In order
 2224 to increase the integrated time without increasing the acquisition time too much, the width of the
 2225 acquisition windows are increased to 10 μ s. The time distribution of the hits is expected to be flat, as
 2226 shown by Figure B.1b.

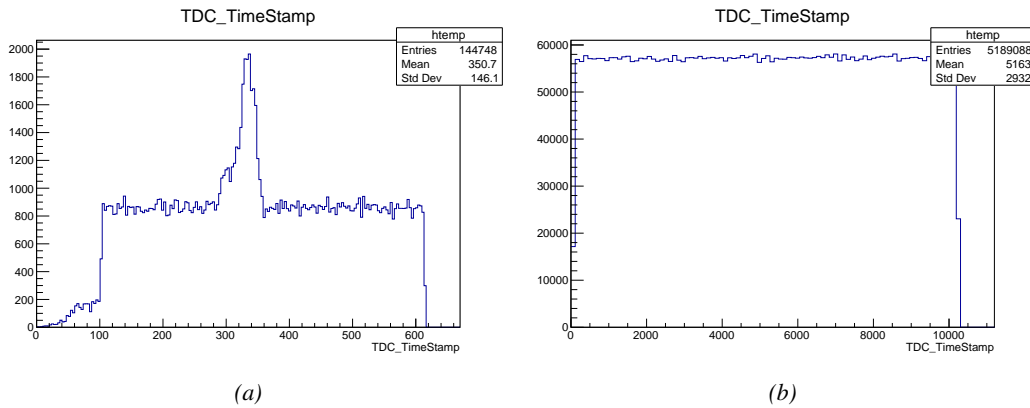


Figure B.1: Example of expected hit time distributions in the cases of efficiency (Figure B.1a) and noise/gamma rate per unit area (Figure B.1b) measurements as extracted from the raw ROOT files. The unit along the x-axis corresponds to ns. The fact that "the" muon peak is not well defined in Figure B.1a is due to the contribution of all the RPCs being tested at the same time that don't necessarily have the same signal arrival time. Each individual peak can have an offset with the ones of other detectors. The inconsistency in the first 100 ns of both time distributions is an artefact of the TDCs and are systematically rejected during the analysis.

2227 The ROOT files include a TTree called RunParameters containing, among other things, the in-
 2228 formation related to the type of run. The run type can then be accessed as described by Source
 2229 Code B.12 and the function IsEfficiencyRun() is then used to determine if the run file is an effi-
 2230 ciency run or, on the contrary, another type of run (noise or gamma measurement).

```

2231     TTree* RunParameters = (TTree*)dataFile.Get("RunParameters");
2232     TString* RunType = new TString();
2233     RunParameters->SetBranchAddress("RunType", &RunType);
2234     RunParameters->GetEntry(0);

```

2233 *Source Code B.12: Access to the run type contained in TTree* RunParameters.*

2234 Finally, the data files will have a slightly different content whether it was collected before or after
 2235 October 2017 and the upgrade of the DAQ software that brought a new information into the ROOT
 2236 output. This is discussed in Appendix A.4.3 and implies that the analysis will differ a little depending
 2237 on the data format. Indeed, as no information on the data quality is stored, in older data files, the cor-
 2238 rections for missing events has to be done at the end of the analysis. The information about the type
 2239 of data format is stored in the variable **bool** `isNewFormat` by checking the list of branches contained
 2240 in the data tree via the methods `TTree::GetListOfBranches()` and `TCollection::Contains()`.

2241 **B.6.2 Beam time window calculation for efficiency runs**

2242 Knowing the run type is important first of all to know the width of the acquisition window to be used
 2243 for the rate calculation and finally to be able to seek for muons. Indeed, the peak that appears in the
 2244 time distribution for each detectors is then fitted to extract the most probable time window in which
 2245 the tool should look for muon hits. The data outside of this time window is then used to evaluate the
 2246 noise or gamma background the detector was subjected to during the data taking. Computing the
 2247 position of the peak is done calling the function `SetBeamWindow()` defined in file `src/RPCHit.cc` that
 2248 loops a first time on the data. The data is first sorted in a 3D array of 1D histograms (`GIFH1Array`, see
 2249 include/types.h). Then the location of the highest bin is determined using `TH1::GetMaximumBin()`
 2250 and is used to define a window in which a gaussian fit will be applied to compute the peak width.
 2251 This window is a 80 ns defined by Formula B.1 around the central bin.

$$t_{center}(ns) = bin \times width_{bin}(ns) \quad (\text{B.1a})$$

$$[t_{low}; t_{high}] = [t_{center} - 40; t_{center} + 40] \quad (\text{B.1b})$$

2252 Before the fit is performed, the average number of noise/gamma hits per bin is evaluated using
 2253 the data outside of the fit window. Excluding the first 100 ns, the average number of hits per bin
 2254 due to the noise or gamma is defined by Formula B.2 after extracting the amount of hits in the time
 2255 windows $[100; t_{low}]$ and $[t_{high}; 600]$ thanks to the method `TH1::Integral()`. This average number
 2256 of hits is then subtracted to every bin of the 1D histogram, in order to *clean* it from the noise or
 2257 gamma contribution as much as possible to improve the fit quality. Bins where $\langle n_{hits} \rangle$ is greater
 2258 than the actual bin content are set to 0.

$$\Delta t_{noise}(ns) = 600 \overbrace{-t_{high} + t_{low}}^{-80ns} - 100 = 420ns \quad (\text{B.2a})$$

$$\langle n_{hits} \rangle = width_{bin}(ns) \times \frac{\sum_{t=100}^{t_{low}} + \sum_{t=t_{high}}^{600}}{\Delta t_{noise}(ns)} \quad (\text{B.2b})$$

2259 Finally, the fit parameters are extracted and saved for each detector in 3D arrays of **float**
 2260 (`muonPeak`, see include/types.h), a first one for the mean arrival time of the muons, `PeakTime`,

2261 and a second one for the width of the peak, `PeakWidth`. The width is defined as 6σ of the gaussian
 2262 fit. The same settings are applied to every partitions of the same detector. To determine which one
 2263 of the detector's partitions is directly illuminated by the beam, the peak height of each partition is
 2264 compared and the highest one is then used to define the peak settings.

2265 B.6.3 Data loop and histogram filling

2266 3D arrays of histogram are created to store the data and display it on the DQM of GIF++ webDCS
 2267 for the use of shifters. These histograms, presented in section B.2.1.1, are filled while looping on
 2268 the data. Before starting the analysis loop, it is necessary to control the entry quality for the new
 2269 file formats featuring `QFlag`. If the `QFlag` value for this entry shows that 1 TDC or more have a
 2270 `CORRUPTED` flag, then this event is discarded. The loss of statistics is low enough to be neglected.
 2271 `QFlag` is controled using the function `IsCorruptedEvent()` defined in `src/utils.cc`. As explained
 2272 in Appendix A.4.3, each digit of this integer represent a TDC flag that can be 1 or 2. Each 2 is
 2273 the sign of a `CORRUPTED` state. Then, the data is accessed entry by entry in the ROOT `TTree` using
 2274 `RAWData` and each hit in the hit list is assigned to a detector channel and saved in the corresponding
 2275 histograms. In the first part of the analysis, in which the loop over the ROOT file's content is
 2276 performed, the different steps are:

2277 **1- RPC channel assignment and control:** a check is done on the RPC channel extracted thanks
 2278 to the mapping via the method `Mapping::GetLink()`. If the channel is not initialised and is 0, or if
 2279 the TDC channel was greater than 5127, the hit is discarded. This means there was a problem in the
 2280 mapping. Often a mapping problem leads to the crash of the offline tool.

2281 **2- Creation of a `RPCHit` object:** to easily get the trolley, slot and partition in which the hit has
 2282 been assigned, this object is particularly helpful.

2283 **3- General histograms are filled:** the hit is filled into the time distribution and the general hit
 2284 distribution histograms, and if the arrival time is within the first 100 ns, it is discarded and nothing
 2285 else happens and the loop proceeds with the next hit in the list.

2286 **4- Multiplicity counter:** the hit multiplicity counter of the corresponding detectors incremented.

2287 **5-a- Efficiency runs - Is the hit within the peak window? :** if the peak is contained in the peak
 2288 window previously defined in section B.6.2, the hit is filled into the beam hit profile histogram of
 2289 the corresponding chamber, added into the list of muon hits and increments the counter of *in time*
 2290 hits. The term *in time* here refers to the hits that are likely to be muons by arriving in the expected
 2291 time window. If the hit is outside of the peak window, it is filled into the noise profile histogram
 2292 of the corresponding detector, added into the list of noise/gamma hits and increments the counter of
 2293 noise/gamma hits.

2294 **5-b- Noise/gamma rate runs - Noise histograms are filled:** the hit is filled into the noise profile
 2295 histogram of the corresponding detector, added into the list of noise/gamma hits and increments the
 2296 counter of noise/gamma hits.

2297

2298 After the loop on the hit list of the entry is over, the next step is to clusterize the 3D lists filled
 2299 in the previous steps. A 3D loop is then started over the active trolley, slot and RPC partitions to
 2300 access these objects. Each `NoiseHitList` and `MuonHitList`, in case of efficiency run, are clusterized
 2301 as described in section B.5.2. There corresponding cluster size and multiplicity histograms are filled
 2302 at the end of the clustering process. Then, the efficiency histogram is filled in case of efficiency run.
 2303 The selection is simply made by checking whether the RPC detected signals in the peak window
 2304 during this event. Nevertheless, it is useful to highlight that at this level, it is not possible yet to
 2305 discriminate in between a muon hit and noise or gamma hit. Thus, `MuonCSize_H`, `MuonCMult_H`
 2306 and `Efficiency0_H` are subjected to noise and gamma contamination. This contamination will be
 2307 estimated and corrected at the moment the results will be written into output CSV files. Finally, the
 2308 loop ends on the filling of the general hit multiplicity histogram.

2309 **B.6.4 Results calculation**

2310 As mentioned in section B.2.1, the analysis of DAQ data provides the user with 3 CSV files and
 2311 a ROOT file associated to each and every ROOT data file. The fourth CSV file is provided by the
 2312 extraction of the CEAN main frame data monitored during data taking and will be discussed later.
 2313 After looping on the data in the previous part of the analysis macro, the output files are created and a
 2314 3D loop on each RPC readout partitions is started to extract the histograms parameters and compute
 2315 the final results.

2316

2317 **B.6.4.1 Rate normalisation**

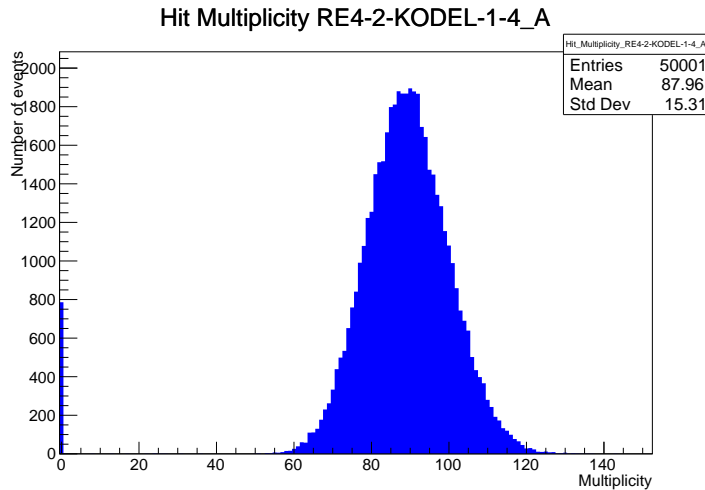


Figure B.2: The effect of the quality flag is explained by presenting the reconstructed hit multiplicity of a data file without `Quality_flag`. The artificial high content of bin 0 is the effect of corrupted data.

2318 To analyse old data format files, not containing any quality flag, it is needed to estimate the amount
 2319 of corrupted data via a fit as the corrupted data will always fill events with a fake "0 multiplicity".
 2320 Indeed, as no hits were stored in the DAQ ROOT files, these events artificially contribute to fill
 2321 the bin corresponding to a null multiplicity, as shown in Figure B.2. In the case the mean of the

hit multiplicity distribution is high, the contribution of the corrupted data can easily be evaluated for later correction by comparing the level of the bin at multiplicity 0 and of a skew fit curve that should indicate a value consistent with 0. A skew fit has been chosen over a Poisson fit as it was giving better results for lower mean multiplicity values. Nevertheless, for low irradiation cases, as explained in Appendix A.4.3, the hit multiplicity distribution mean is, on the contrary, rather small and the probability to record events without hits can't be considered small anymore, leading to a difficult and non-reliable estimation of the corruption. As can be seen in Source Code B.13, conditions have been applied to prevent bad fits and wrong corruption estimation in cases where :

- The difference in between the data for multiplicity 1 and the corresponding fit value should be lower than 1% of the total amount of data : $\frac{|n_{m=1} - sk(1)|}{N_{tot}} < 0.01$ where $n_{m=1}$ is the number of entries with multiplicity 1, $sk(1)$ the value of the skew fit, as defined by Formula 4.3, for multiplicity 1 and N_{tot} the total number of entries.

- The amount of data contained in the multiplicity 0 bin should not exceed 40% : $\frac{n_{m=0}}{N_{tot}} \leq 0.4$ where $n_{m=0}$ is the number of entries with multiplicity 0. This number has been determined to be the maximum to be able to separate the excess of data due to corruption from the hit multiplicity distribution.

Those 2 conditions need to be fulfilled to estimate the corruption of old data format files. If the fit was successful, the level of corruption is written in `Offline-Corrupted.csv` and the number of corrupted entries, refered as the integer `nEmptyEvent`, is subtracted from the total number of entries when the rate normalisation factor is computed as explicit in Source Code B.13. Note that for new data format files, the number of corrupted entries being set to 0, the definition of `rate_norm` stays valid.

```

2344
if(!isNewFormat){
    TF1* GaussFit = new TF1("gaussfit","[0]*exp(-0.5*((x-[1])/[2])**2)",0,Xmax);
    GaussFit->SetParameter(0,100);
    GaussFit->SetParameter(1,10);
    GaussFit->SetParameter(2,1);
    HitMultiplicity_H.rpc[T][S][p]->Fit(GaussFit,"LIQR","",0.5,Xmax);

    TF1* SkewFit = new TF1("skewfit","[0]*exp(-0.5*((x-[1])/[2])**2) / (1 +
→ exp(-[3]*(x-[4])))",0,Xmax);
    SkewFit->SetParameter(0,GaussFit->GetParameter(0));
    SkewFit->SetParameter(1,GaussFit->GetParameter(1));
    SkewFit->SetParameter(2,GaussFit->GetParameter(2));
    SkewFit->SetParameter(3,1);
    SkewFit->SetParameter(4,1);
    HitMultiplicity_H.rpc[T][S][p]->Fit(SkewFit,"LIQR","",0.5,Xmax);

    double fitValue = SkewFit->Eval(1,0,0,0);
    double dataValue = (double)HitMultiplicity_H.rpc[T][S][p]->GetBinContent(2);
    double difference = TMath::Abs(dataValue - fitValue);
    double fitTOdataVSentries_ratio = difference / (double)nEntries;
    bool isFitGOOD = fitTOdataVSentries_ratio < 0.01;

2345
    double nSinglehit = (double)HitMultiplicity_H.rpc[T][S][p]->GetBinContent(1);
    double lowMultRatio = nSinglehit / (double)nEntries;
    bool isMultLOW = lowMultRatio > 0.4;

    if(isFitGOOD && !isMultLOW){
        nEmptyEvent = HitMultiplicity_H.rpc[T][S][p]->GetBinContent(1);
        nPhysics = (int)SkewFit->Eval(0,0,0,0);
        if(nPhysics < nEmptyEvent)
            nEmptyEvent = nEmptyEvent-nPhysics;
    }
}

double corrupt_ratio = 100.*(double)nEmptyEvent / (double)nEntries;
outputCorrCSV << corrupt_ratio << '\t';

float rate_norm = 0.;
float stripArea = GIFIInfra->GetStripGeo(tr,sl,p);

if(IsEfficiencyRun(RunType)){
    float noiseWindow = BMTDCWINDOW - TIMEREJECT - 2*PeakWidth.rpc[T][S][p];
    rate_norm = (nEntries-nEmptyEvent)*noiseWindow*1e-9*stripArea;
} else
    rate_norm = (nEntries-nEmptyEvent)*RDMNOISEWDW*1e-9*stripArea;

```

Source Code B.13: Definition of the rate normalisation variable. It takes into account the number of non corrupted entries and the time window used for noise calculation, to estimate the total integrated time, and the strip active area to express the result as rate per unit area.

2347 B.6.4.2 Rate and activity

2348 At this point, the strip rate histograms, StripNoiseProfile_H.rpc[T][S][p], only contain an in-
2349 formation about the total number of noise or rate hits each channel received during the data taking.
2350 As described in Source Code B.14, a loop on the strip channels will be used to normalise the content
2351 of the rate distribution histogram for each detector partitions. The initial number of hits recorded for
2352 a given bin will be extracted and 2 values will be computed:

- 2353 ● the strip rate, defined as the number of hits recorded in the bin normalised like described in
 2354 the previous section, using the variable `rate_norm`, and

- 2355 ● the strip activity, defined as the number of hits recorded in the bin normalised to the average
 2356 number of hits per bin contained in the partition histogram, using the variable `averageNhit`.
 2357 This value provides an information on the homogeneity of the detector response to the gamma
 2358 background or of the detector noise. An activity of 1 corresponds to an average response.
 2359 Above 1, the channel is more active than the average and bellow 1, the channel is less active.

```

int nNoise = StripNoiseProfile_H.rpc[T][S][p]->GetEntries();
float averageNhit = (nNoise>0) ? (float)(nNoise/nStripsPart) : 1.;

for(Uint st = 1; st <= nStripsPart; st++) {
    float stripRate =
        StripNoiseProfile_H.rpc[T][S][p]->GetBinContent(st)/rate_norm;
    float stripAct =
        StripNoiseProfile_H.rpc[T][S][p]->GetBinContent(st)/averageNhit;

    StripNoiseProfile_H.rpc[T][S][p]->SetBinContent(st,stripRate);
    StripActivity_H.rpc[T][S][p]->SetBinContent(st,stripAct);
}

```

2361 *Source Code B.14: Description of the loop that allows to set the content of each strip rate and strip activity
 channel for each detector partition.*

2362 On each detector partitions, which are readout by a single FEE, all the channels are not processed
 2363 by the same chip. Each chip can give a different noise response and thus, histograms using a chip
 2364 binning are used to investigate chip related noise behaviours. The average values of the strip rate
 2365 or activity grouped into a given chip are extracted using the using the function `GetChipBin()` and
 2366 stored in dedicated histograms as described in Source Codes B.15 and B.16 respectively.

```

float GetChipBin(TH1* H, Uint chip){
    Uint start = 1 + chip*NSTRIPSCHIP;
    int nActive = NSTRIPSCHIP;
    float mean = 0.;

    for(Uint b = start; b <= (chip+1)*NSTRIPSCHIP; b++) {
        float value = H->GetBinContent(b);
        mean += value;
        if(value == 0.) nActive--;
    }

    if(nActive != 0) mean /= (float)nActive;
    else mean = 0.;

    return mean;
}

```

2369 *Source Code B.15: Function used to compute the content of a bin for an histogram using chip binning.*

```

2370   for(UInt ch = 0; ch < (nStripsPart/NSTRIPSCHIP); ch++) {
      ChipMeanNoiseProf_H.rpc[T][S][p]->
          SetBinContent(ch+1,GetChipBin(StripNoiseProfile_H.rpc[T][S][p],ch));
      ChipActivity_H.rpc[T][S][p]->
          SetBinContent(ch+1,GetChipBin(StripActivity_H.rpc[T][S][p],ch));
}

```

Source Code B.16: Description of the loop that allows to set the content of each chip rate and chip activity bins for each detector partition knowing the information contained in the corresponding strip distribution histograms.

The activity variable is used to evaluate the homogeneity of the detector response to background or of the detector noise. The homogeneity h_p of each detector partition can be evaluated using the formula $h_p = \exp(-\sigma_p^R / \langle R \rangle_p)$, where $\langle R \rangle_p$ is the partition mean rate and σ_p^R is the rate standard deviation calculated over the partition channels. The more homogeneously the rates are distributed and the smaller will σ_p^R be, and the closer to 1 will h_p get. On the contrary, if the standard deviation of the channel's rates is large, h_p will rapidly get to 0. This value is saved into histograms as shown in Source Code B.17 and could in the future be used to monitor through time, once extracted, the evolution of every partition homogeneity. This could be of great help to understand the apparition of eventual hot spots due to ageing of the chambers subjected to high radiation levels. The monitored homogeneity information could then be combined with a monitoring of the activity of each individual channel in order to have a finer information. Monitoring tools have been suggested and need to be developed for this purpose.

```

2384   float MeanPartSDev = GetTH1StdDev(StripNoiseProfile_H.rpc[T][S][p]);
   float strip_homog = (MeanPartRate==0)
     ? 0.
     : exp(-MeanPartSDev/MeanPartRate);
   StripHomogeneity_H.rpc[T][S][p]->Fill("exp -#left(#frac{\#sigma_{Strip}
     \rightarrow Rate}{\#mu_{Strip Rate}}\#right)",strip_homog);
   StripHomogeneity_H.rpc[T][S][p]->GetYaxis()->SetRangeUser(0.,1.);

2385   float ChipStDevMean = GetTH1StdDev(ChipMeanNoiseProf_H.rpc[T][S][p]);
   float chip_homog = (MeanPartRate==0)
     ? 0.
     : exp(-ChipStDevMean/MeanPartRate);
   ChipHomogeneity_H.rpc[T][S][p]->Fill("exp -#left(#frac{\#sigma_{Chip}
     \rightarrow Rate}{\#mu_{Chip Rate}}\#right)",chip_homog);
   ChipHomogeneity_H.rpc[T][S][p]->GetYaxis()->SetRangeUser(0.,1.);

```

Source Code B.17: Storage of the homogeneity into dedicated histograms.

B.6.4.3 Strip masking tool

The offline tool is automatically called at the end of each data taking to analyse the data and offer the shifter DQM histograms to control the data quality. After the histograms have been published online in the DQM page, the shifter can decide to mask noisy or dead channels that will contribute to bias the final rate calculation by editing the mask column of `ChannelsMapping.csv` as can be seen in Figure B.3.

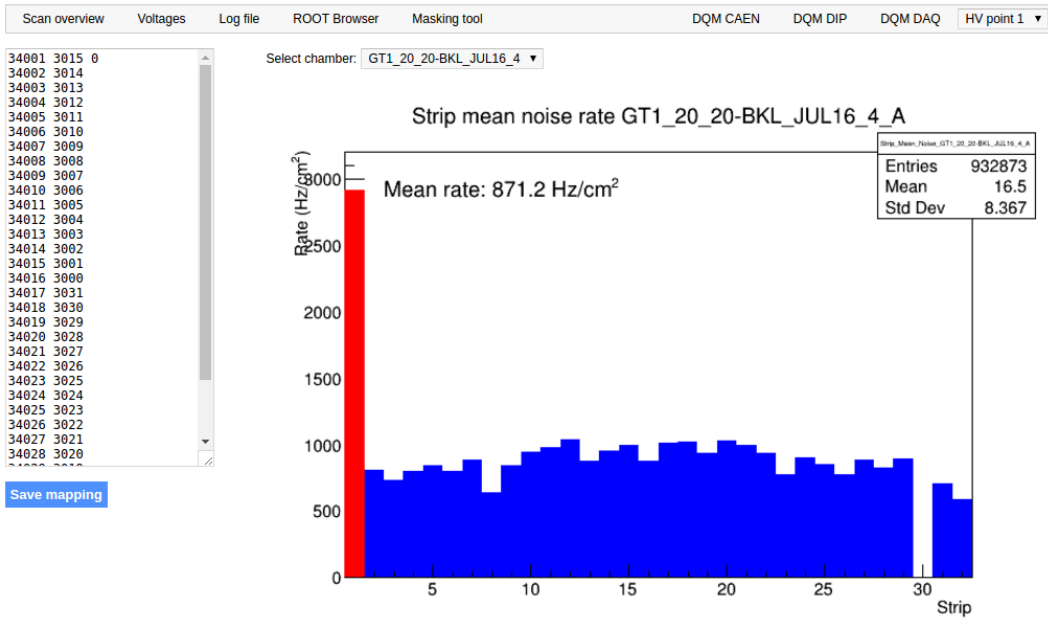


Figure B.3: Display of the masking tool page on the webDCS. The window on the left allows the shifter to edit ChannelsMapping.csv. To mask a channel, it only is needed to set the 3rd field corresponding to the strip to mask to 0. It is not necessary for older mapping file formats to add a 1 for each strip that is not masked as the code is versatile and the default behaviour is to consider missing mask fields as active strips. The effect of the mask is directly visible for noisy channels as the corresponding bin turns red. The global effect of masking strips will be an update of the rate value showed on the histogram that will take into consideration the rejected channels.

2393 From the code point of view, the function `GetTH1Mean()` is used to retrieve the mean rate par-
 2394 tition by partition after the rates have been calculated strip by strip and filled into the histograms
 2395 `StripNoiseProfile_H.rpc[T][S][p]`, as described through Source Code B.18.

2396 Once the mask for each rejected channel has been updated, the shifter can manually run the of-
 2397 fline tool again to update the DQM plots, now including the masked strips, as well the rate results
 2398 written in the output CSV file `Offline-Rate.csv`. If not done during the shifts, the strip masking
 2399 procedure needs to be carefully done by the person in charge of data analysis on the scans that were
 2400 selected to produce the final results.

```

2401   float GetTH1Mean(TH1* H) {
2402     int nBins = H->GetNbinsX();
2403     int nActive = nBins;
2404     float mean = 0.;
2405
2406     for(int b = 1; b <= nBins; b++) {
2407       float value = H->GetBinContent(b);
2408       mean += value;
2409       if(value == 0.) nActive--;
2410     }
2411
2412     if(nActive != 0) mean /= (float)nActive;
2413     else mean = 0.;
2414
2415     return mean;
2416   }

```

Source Code B.18: The function `GetTH1Mean()` is used to return the mean along the y-axis of `TH1` histograms containing rate information. In order to take into account masked strips whose rate is set to 0, the function looks for masked channels and decrement the number of active channels for each null value found.

2404 B.6.4.4 Output CSV files filling

2405 All the histograms have been filled. Parameters will then be extracted from them to compute the
 2406 final results that will later be used to produce plots. Once the results have been computed, the very
 2407 last step of the offline macro is to write these values into the corresponding CSV outputs. Aside of
 2408 the file `Offline-Corrupted.csv`, 2 CSV files are being written by the macro `offlineAnalysis()`,
 2409 `Offline-Rates.csv` and `Offline-L0-EffCl.csv` that respectively contain information about noise
 2410 or gamma rates, cluster size and multiplicity, and about level 0 reconstruction of the detector effi-
 2411 ciency, muon cluster size and multiplicity. Details on the computation and file writing are respec-
 2412 tively given in Sources Codes B.19 and B.20.

2413 **Noise/gamma background variables** are computed and written in the output file for each detector
 2414 partitions. A detector average of the hit and cluster rate is also provided, as shown through Sources
 2415 Code B.19. The variables that are written for each partition are:

- 2416 • The mean partition hit rate per unit area, `MeanPartRate`, that is extracted from the histogram
 2417 `StripNoiseProfile_H` as the mean value along the y-axis, as described in section B.6.4.3. No
 2418 error is recorded for the hit rate as this is considered a single measurement. No statistical error
 2419 can be associated to it and the systematics are unknown.
- 2420 • The mean cluster size, `cSizePart`, is extracted from the histogram `NoiseCSize_H` and it's
 2421 statistical error, `cSizePartErr`, is taken to be 2σ of the total distribution.
- 2422 • The mean cluster multiplicity per trigger, `cMultPart`, is extracted from the histogram `NoiseCMult_H`
 2423 and it's statistical error, `cMultPartErr`, is taken to be 2σ of the total distribution. It is impor-
 2424 tant to point to the fact that this variable gives an information that is dependent on the buffer
 2425 window width used for each trigger for the calculation.
- 2426 • The mean cluster rate per unit area, `ClustPartRate`, is defined as the mean hit rate normalised

2427 to the mean cluster size and it's statistical error, `ClustPartRateErr`, is then obtained using the
 2428 relative statistical error on the mean cluster size.

```

for (UInt tr = 0; tr < GIFInfra->GetNTrolleys(); tr++) {
    UInt T = GIFInfra->GetTrolleyID(tr);

    for (UInt sl = 0; sl < GIFInfra->GetNSlots(tr); sl++) {
        UInt S = GIFInfra->GetSlotID(tr,sl) - 1;

        float MeanNoiseRate = 0.;
        float ClusterRate = 0.;
        float ClusterSDev = 0.;

        for (UInt p = 0; p < GIFInfra->GetNPartitions(tr,sl); p++) {
            float MeanPartRate = GetTH1Mean(StripNoiseProfile_H.rpc[T][S][p]);
            float cSizePart = NoiseCSIZE_H.rpc[T][S][p]->GetMean();
            float cSizePartErr = (NoiseCSIZE_H.rpc[T][S][p]->GetEntries()==0)
                ? 0.
                : 2*NoiseCSIZE_H.rpc[T][S][p]->GetStdDev() /
                    sqrt(NoiseCSIZE_H.rpc[T][S][p]->GetEntries());
            float cMultPart = NoiseCMult_H.rpc[T][S][p]->GetMean();
            float cMultPartErr = (NoiseCMult_H.rpc[T][S][p]->GetEntries()==0)
                ? 0.
                : 2*NoiseCMult_H.rpc[T][S][p]->GetStdDev() /
                    sqrt(NoiseCMult_H.rpc[T][S][p]->GetEntries());
            float ClustPartRate = (cSizePart==0) ? 0.
                : MeanPartRate/cSizePart;
            float ClustPartRateErr = (cSizePart==0) ? 0.
                : ClustPartRate * cSizePartErr/cSizePart;

            outputRateCSV << MeanPartRate << '\t'
                << cSizePart << '\t' << cSizePartErr << '\t'
                << cMultPart << '\t' << cMultPartErr << '\t'
                << ClustPartRate << '\t' << ClustPartRateErr << '\t';

            RPCarea += stripArea * nStripsPart;
            MeanNoiseRate += MeanPartRate * stripArea * nStripsPart;
            ClusterRate += ClustPartRate * stripArea * nStripsPart;
            ClusterSDev += (cSizePart==0)
                ? 0.
                : ClusterRate*cSizePartErr/cSizePart;
        }

        MeanNoiseRate /= RPCarea;
        ClusterRate /= RPCarea;
        ClusterSDev /= RPCarea;

        outputRateCSV << MeanNoiseRate << '\t'
            << ClusterRate << '\t' << ClusterSDev << '\t';
    }
}

```

2430 *Source Code B.19: Description of rate result calculation and writing into the CSV output Offline-Rate.csv.
 Are saved into the file for each detector, the mean partition rate, cluster size and cluster mutiplicity, along with
 their errors, for each partition and as well as a detector average.*

2431 **Muon performance variables** are computed and written in the output file for each detector parti-
 2432 tions as shown through Sources Code B.20. The variables that are written for each partition are:

- 2433 ● The muon efficiency, `eff`, extracted from the histogram `Efficiency0_H`. It is reminded that
2434 this offline tool doesn't include any tracking algorithm to identify muons from the beam and
2435 only relies on the hits arriving in the time window corresponding to the beam time. The con-
2436 tent of the efficiency histogram is thus biased by the noise/gamma background contribution
2437 into this window and is thus corrected by estimating the muon data content in the peak re-
2438 gion knowing the noise/gamma content in the rate calculation region. Both time windows
2439 being different, the choice was made to normalise the noise/gamma background calculation
2440 window to it's equivalent beam window in order to have comparable values using the variable
2441 `windowRatio`. Finally, to estimate the data ratio in the peak region, the variable `DataRatio`
2442 is defined as the ratio in between the estimated mean cluster multiplicity of the muons in the
2443 peak region, `MuonCM`, and of the total mean cluster multiplicity in the peak region, `PeakCM`.
2444 `MuonCM` is itself defined as the difference in between the total mean cluster multiplicity in the
2445 peak region and the normalised mean noise/gamma cluster multiplicity calculated outside of
2446 the peak region. The statistical error related to the efficiency, `eff_err`, is computed using a
2447 binomial distribution, as the efficiency measure the probability of "success" and "failure" to
2448 detect muons.
- 2449 ● The mean muon cluster size, `MuonCS`, is calculated using the total mean cluster size and multi-
2450 plicity in the peak region, respectively extracted from histograms `MuonCSize_H` and `MuonCMult_H`,
2451 the noise/gamma background mean cluster size and normalised multiplicity, extracted from
2452 `NoiseCSize_H` and `NoiseCMult_H`, and of the estimated muon cluster multiplicity `MuonCM` pre-
2453 viously explicated. The associated statistical error, `MuonCM_err`, is calculated using the propa-
2454 gation of errors of the mentioned variables.
- 2455 ● The mean muon cluster multiplicity in the peak region, `MuonCM`, explicated above whose sta-
2456 tistical error, `MuonCM_err`, is the sum of statistical error associated to the total mean clus-
2457 ter multiplicity in the peak reagion, `PeakCM_err`, and of the mean noise/gamma cluster size,
2458 `NoiseCM_err`.

2459 In addition to these 2 CSV files, the histograms are saved in ROOT file `Scan00XXXX_HVY_Offline.root`
2460 as explained in section B.2.1.1.

2461

```

for (UInt tr = 0; tr < GIFInfra->GetNTrolleys(); tr++) {
    UInt T = GIFInfra->GetTrolleyID(tr);
    for (UInt sl = 0; sl < GIFInfra->GetNSlots(tr); sl++) {
        UInt S = GIFInfra->GetSlotID(tr,sl) - 1;
        for (UInt p = 0; p < GIFInfra->GetNPartitions(tr,sl); p++) {
            float noiseWindow =
                BMTDCWINDOW - TIMEREJECT - 2*PeakWidth.rpc[T][S][p];
            float peakWindow = 2*PeakWidth.rpc[T][S][p];
            float windowRatio = peakWindow/noiseWindow;

            float PeakCM = MuonCMult_H.rpc[T][S][p]->GetMean();
            float PeakCS = MuonCSize_H.rpc[T][S][p]->GetMean();
            float NoiseCM = NoiseCMult_H.rpc[T][S][p]->GetMean() *windowRatio;
            float NoiseCS = NoiseCSize_H.rpc[T][S][p]->GetMean();
            float MuonCM = (PeakCM<NoiseCM) ? 0. : PeakCM-NoiseCM;
            float MuonCS = (MuonCM==0 || PeakCM*PeakCS<NoiseCM*NoiseCS)
                ? 0.
                : (PeakCM*PeakCS-NoiseCM*NoiseCS) / MuonCM;
            float PeakCM_err = (MuonCMult_H.rpc[T][S][p]->GetEntries()==0.)
                ? 0.
                : 2*MuonCMult_H.rpc[T][S][p]->GetStdDev() /
                    sqrt(MuonCMult_H.rpc[T][S][p]->GetEntries());
            float PeakCS_err = (MuonCSize_H.rpc[T][S][p]->GetEntries()==0.)
                ? 0.
                : 2*MuonCSize_H.rpc[T][S][p]->GetStdDev() /
                    sqrt(MuonCSize_H.rpc[T][S][p]->GetEntries());
            float NoiseCM_err = (NoiseCMult_H.rpc[T][S][p]->GetEntries()==0.)
                ? 0.
                : windowRatio*2*NoiseCMult_H.rpc[T][S][p]->GetStdDev() /
                    sqrt(NoiseCMult_H.rpc[T][S][p]->GetEntries());
            float NoiseCS_err = (NoiseCSize_H.rpc[T][S][p]->GetEntries()==0.)
                ? 0.
                : 2*NoiseCSize_H.rpc[T][S][p]->GetStdDev() /
                    sqrt(NoiseCSize_H.rpc[T][S][p]->GetEntries());
            float MuonCM_err = (MuonCM==0) ? 0. : PeakCM_err+NoiseCM_err;
            float MuonCS_err = (MuonCS==0 || MuonCM==0) ? 0.
                : (PeakCS*PeakCM_err + PeakCM*PeakCS_err +
                    NoiseCS*NoiseCM_err + NoiseCM*NoiseCS_err +
                    MuonCS*MuonCM_err) / MuonCM;

            float DataRatio = MuonCM/PeakCM;
            float DataRatio_err = (MuonCM==0) ? 0.
                : DataRatio*(MuonCM_err/MuonCM + PeakCM_err/PeakCM);
            float eff = DataRatio*Efficiency0_H.rpc[T][S][p]->GetMean();
            float eff_err = DataRatio*2*Efficiency0_H.rpc[T][S][p]->GetStdDev() /
                sqrt(Efficiency0_H.rpc[T][S][p]->GetEntries()) +
                Efficiency0_H.rpc[T][S][p]->GetMean()*DataRatio_err;

            outputEffCSV << eff << '\t' << eff_err << '\t'
                << MuonCS << '\t' << MuonCS_err << '\t'
                << MuonCM << '\t' << MuonCM_err << '\t';
        }
    }
}

```

2462

2463

Source Code B.20: Description of efficiency result calculation and writing into the CSV output Offline-L0-EffCl.csv. Are saved into the file for each detector, the efficiency, corrected taking into account the background in the peak window of the time profile, muon cluster size and muon cluster multiplicity, along with their errors, for each partition and as well as a detector average.

B.7 Current data Analysis

Detectors under test at GIF++ are connected both to a CAEN HV power supply and to a CAEN ADC that reads the currents inside of the RPC gaps bypassing the supply cable. During data taking, the webDCS records into a ROOT file called `Scan00XXXX_HVY_CAEN.root` histograms with the monitored parameters of both CAEN devices. Are recorded for each RPC channels (in most cases, a channel corresponds to an RPC gap):

- the effective voltage, HV_{eff} , set by the webDCS using the PT correction on the CAEN power supply,
- the applied voltage, HV_{app} , monitored by the CAEN power supply, and the statistical error related to the variations of this value through time to follow the variation of the environmental parameters defined as the RMS of the histogram divided by the square root of the number of recorded points,
- the monitored current, I_{mon} , monitored by the CAEN power supply, and the statistical error related to the variations of this value through time to follow the variation of the environmental parameters defined as the RMS of the histogram divided by the square root of the number of recorded points,
- the corresponding current density, J_{mon} , defined as the monitored current per unit area, $J_{mon} = I_{mon}/A$, where A is the active area of the corresponding gap,
- the ADC current, I_{ADC} , recorded through the CAEN ADC module that monitors the dark current in the gap itself. First of all, the resolution of such a module is better than that of CAEN power supplies and moreover, the current is not read-out through the HV supply line but directly at the chamber level giving the real current inside of the detector. The statistical error is defined as the RMS of the histogram distribution divided by the square root of the number of recorded points.

Once extracted through a loop over the element of GIF++ infrastructure via the C++ macro `GetCurrent()`, these parameters, organised in 9 columns per detector HV supply line, are written in the output CSV file `Offline-Current.csv`. The macro can be found in the file `Current.cc`.

References

2491

- 2492 [1] T. Massam et al. “Experimental observation of antideuteron production”. In: *Il Nuovo Cimento A* 63 (1965), pp. 10–14.
- 2493
- 2494 [2] UA1 Collaboration. “Experimental observation of isolated large transverse energy electrons with associated missing energy at $s = 540 \text{ GeV}$ ”. In: *Physics Letters B* 122 (1983), pp. 103–116.
- 2495
- 2496
- 2497 [3] UA2 Collaboration. “Observation of single isolated electrons of high transverse momentum in events with missing transverse energy at the CERN pp collider”. In: *Physics Letters B* 122 (1983), pp. 476–485.
- 2498
- 2499
- 2500 [4] UA1 Collaboration. “Experimental observation of lepton pairs of invariant mass around $95 \text{ GeV}/c^2$ at the CERN SPS collider”. In: *Physics Letters B* 126 (1983), pp. 398–410.
- 2501
- 2502 [5] UA2 Collaboration. “Evidence for $Z_0 \rightarrow e^+e^-$ at the CERN pp collider”. In: *Physics Letters B* 129 (1983), pp. 130–140.
- 2503
- 2504 [6] ALEPH Collaboration. “Determination of the number of light neutrino species”. In: *Physics Letters B* 231 (1989), pp. 519–529.
- 2505
- 2506 [7] CERN, ed. (1985).
- 2507 [8] CERN, ed. (1986).
- 2508 [9] CERN, ed. (1994).
- 2509 [10] CERN, ed. (1998).
- 2510 [11] CERN, ed. (1999).
- 2511 [12] CERN. Geneva. LHC Experiments Committee. *Letter of Intent for A Large Ion Collider Experiment [ALICE]*, note = CERN-LHCC-93-016. Tech. rep. ALICE Collaboration, 1993.
- 2512
- 2513 [13] CERN. Geneva. LHC Experiments Committee. *ATLAS : technical proposal for a general-purpose pp experiment at the Large Hadron Collider at CERN*, note = CERN-LHCC-94-43. Tech. rep. ATLAS Collaboration, 1994.
- 2514
- 2515
- 2516 [14] CERN. Geneva. LHC Experiments Committee. *CMS : letter of intent by the CMS Collaboration for a general purpose detector at LHC*, note = CERN-LHCC-92-003. Tech. rep. CMS Collaboration, 1992.
- 2517
- 2518
- 2519 [15] CERN. Geneva. LHC Experiments Committee. *LHCb : letter of intent*. Tech. rep. CERN-LHCC-95-5. LHCb Collaboration, 1995.
- 2520
- 2521 [16] L. Evans and P. Bryant. “LHC Machine”. In: *JINST* 3 (2008). S08001.
- 2522
- 2523 [17] CMS Collaboration ATLAS Collaboration. “Combined Measurement of the Higgs Boson Mass in pp Collisions at $\sqrt{s} = 7$ and 8 TeV with the ATLAS and CMS Experiments”. In: *Physical Review Letters* 114 (2015). 191803.
- 2524
- 2525 [18] LHCb Collaboration. “Observation of $J/\psi p$ Resonances Consistent with Pentaquark States in $\Lambda_b^0 \rightarrow J/\psi K^- p$ Decays”. In: *Physical Review Letters* 115 (2015). 072001.
- 2526

- 2527 [19] LHCb Collaboration. “Observation of $J/\psi\phi$ Structures Consistent with Exotic States from
2528 Amplitude Analysis of $B^+ \rightarrow J/\psi\phi K^+$ Decays”. In: *Physical Review Letters* 118 (2017).
2529 022003.
- 2530 [20] CERN. Geneva. *High-Luminosity Large Hadron Collider (HL-LHC) Technical Design Re-*
2531 *port V. 0.1*. Tech. rep. CERN-2017-007-M. 2017.
- 2532 [21] CERN. Geneva. LHC Experiments Committee. *The CMS muon project : Technical Design*
2533 *Report*. Tech. rep. CERN-LHCC-97-032. CMS Collaboration, 1997.
- 2534 [22] CERN. Geneva. LHC Experiments Committee. *Technical Proposal for the Phase-II Upgrade*
2535 *of the CMS Detector*. Tech. rep. CERN-LHCC-2015-010. CMS Collaboration, 2015.
- 2536 [23] CERN. Geneva. LHC Experiments Committee. *CMS, the Compact Muon Solenoid : technical*
2537 *proposal*. Tech. rep. CERN-LHCC-94-38. CMS Collaboration, 1994.
- 2538 [24] R. Santonico and R. Cardarelli. “Development of resistive plate counters”. In: *Nucl. Instr.*
2539 *Meth. Phys. Res.* 187 (1981), pp. 377–380.
- 2540 [25] Yu.N. Pestov and G.V. Fedotovich. *A picosecond time-of-flight spectrometer for the VEPP-2M*
2541 *based on local-discharge spark counter*. Tech. rep. SLAC-TRANS-0184. SLAC, 1978.
- 2542 [26] W.W. Ash, ed. *Spark Counter With A Localized Discharge*. Vol. SLAC-R-250. 1982, pp. 127–
2543 131.
- 2544 [27] I. Crotty et al. “The non-spark mode and high rate operation of resistive parallel plate cham-
2545 bers”. In: *NIMA* 337 (1993), pp. 370–381.
- 2546 [28] I. Crotty et al. “Further studies of avalanche mode operation of resistive parallel plate cham-
2547 bers”. In: *NIMA* 346 (1994), pp. 107–113.
- 2548 [29] R. Cardarelli et al. “Avalanche and streamer mode operation of resistive plate chambers”. In:
2549 *NIMA* 382 (1996), pp. 470–474.
- 2550 [30] E. Cerron Zeballos et al. “A new type of resistive plate chamber: The multigap RPC”. In:
2551 *NIMA* 374 (1996), pp. 132–135.
- 2552 [31] M.C.S. Williams. “The development of the multigap resistive plate chamber”. In: *Nucl. Phys.*
2553 *B* 61 (1998), pp. 250–257.
- 2554 [32] H. Czyrkowski et al. “New developments on resistive plate chambers for high rate operation”.
2555 In: *NIMA* 419 (1998), pp. 490–496.
- 2556 [33] P. Camarri et al. “Streamer suppression with SF6 in RPCs operated in avalanche mode”. In:
2557 *NIMA* 414 (1998), pp. 317–324.
- 2558 [34] E. Cerron Zeballos et al. “Effect of adding SF6 to the gas mixture in a multigap resistive plate
2559 chamber”. In: *NIMA* 419 (1998), pp. 475–478.
- 2560 [35] CERN. Geneva. LHC Experiments Committee. *ATLAS muon spectrometer: Technical design*
2561 *report*. Tech. rep. CERN-LHCC-97-22. ATLAS Collaboration, 1997.
- 2562 [36] CERN. Geneva. LHC Experiments Committee. *ALICE Time-Of-Flight system (TOF) : Tech-*
2563 *nical Design Report*. Tech. rep. CERN-LHCC-2000-012. ALICE Collaboration, 2000.
- 2564 [37] The CALICE collaboration. “First results of the CALICE SDHCAL technological proto-
2565 type”. In: *JINST* 11 (2016).
- 2566 [38] PoS, ed. *Density Imaging of Volcanoes with Atmospheric Muons using GRPCs*. International
2567 Europhysics Conference on High Energy Physics - HEP 2011. 2011.
- 2568 [39] C. Lippmann. “Detector Physics of Resistive Plate Chambers”. PhD thesis. Johann Wolfgang
2569 Goethe-Universität, 2003.

BIBLIOGRAPHY

- [40] M. Abbrescia et al. “Properties of C₂H₂F₄-based gas mixture for avalanche mode operation of resistive plate chambers”. In: *NIMA* 398 (1997), pp. 173–179.
- [41] G. Battistoni et al. “Sensitivity of streamer mode to single ionization electrons”. In: *NIMA* 235 (1985), pp. 91–97.
- [42] W. Riegler. “Induced signals in resistive plate chambers”. In: *NIMA* 491 (2002), pp. 258–271.
- [43] E. Cerron Zeballos et al. “A comparison of the wide gap and narrow gap resistive plate chamber”. In: *NIMA* 373 (1996), pp. 35–42.
- [44] M. Abbrescia et al. “Cosmic ray tests of double-gap resistive plate chambers for the CMS experiment”. In: *NIMA* 550 (2005), pp. 116–126.
- [45] ALICE Collaboration. “A study of the multigap RPC at the gamma irradiation facility at CERN”. In: *NIMA* 490 (2002), pp. 58–70.
- [46] B. Bonner et al. “A multigap resistive plate chamber prototype for time-of-flight for the STAR experiment at RHIC”. In: *NIMA* 478 (2002), pp. 176–179.
- [47] S. Yang et al. “Test of high time resolution MRPC with different readout modes for the BESIII upgrade”. In: *NIMA* 763 (2014), pp. 190–196.
- [48] A. Akindinov et al. “RPC with low-resistive phosphate glass electrodes as a candidate for the CBM TOF”. In: *NIMA* 572 (2007), pp. 676–681.
- [49] JINST, ed. *Development of the MRPC for the TOF system of the MultiPurpose Detector*. RPC2016: XII Workshop on Resistive Plate Chambers and Related Detectors. 2016.
- [50] M.C.S. Williams. “Particle identification using time of flight”. In: *Journal of Physics G* 39 (2012).
- [51] A. Alici et al. “Aging and rate effects of the Multigap RPC studied at the Gamma Irradiation Facility at CERN”. In: *NIMA* 579 (2007), pp. 979–988.
- [52] M. Abbrescia et al. “The simulation of resistive plate chambers in avalanche mode: charge spectra and efficiency”. In: *NIMA* 431 (1999), pp. 413–427.
- [53] M. Abbrescia et al. “Study of long-term performance of CMS RPC under irradiation at the CERN GIF”. In: *NIMA* 533 (2004), pp. 102–106.
- [54] H.C. Kim et al. “Quantitative aging study with intense irradiation tests for the CMS forward RPCs”. In: *NIMA* 602 (2009), pp. 771–774.
- [55] S. Agosteo et al. “A facility for the test of large-area muon chambers at high rates”. In: *NIMA* 452 (2000), pp. 94–104.
- [56] PoS, ed. *CERN GIF ++ : A new irradiation facility to test large-area particle detectors for the high-luminosity LHC program*. Vol. TIPP2014. 2014, pp. 102–109.
- [57] A. Fagot. *GIF++ DAQ v4.0*. 2017. URL: https://github.com/afagot/GIF_DAQ.
- [58] CAEN. *Mod. V1190-VX1190 A/B, 128/64 Ch Multihit TDC*. 14th ed. 2016.
- [59] CAEN. *Mod. V1718 VME USB Bridge*. 9th ed. 2009.
- [60] W-Ie-Ne-R. *VME 6021-23 VXI*. 5th ed. 2016.
- [61] Wikipedia. *INI file*. 2017. URL: https://en.wikipedia.org/wiki/INI_file.
- [62] S. Carrillo A. Fagot. *GIF++ Offline Analysis v6*. 2017. URL: https://github.com/afagot/GIF_OfflineAnalysis.